University of Exeter
Department of Computer Science

Surface analysis and fingerprint recognition from multi-light imaging collections

Matthew McGuigan

March 30, 2023

Supervised by Dr Jacqueline Christmas

Submitted by Matthew McGuigan, to the University of Exeter as a thesis for the degree of Doctor of Philosophy in Computer Science, March 30, 2023.

I certify that all material in this thesis which is not my own work has been identified and that no material has previously been submitted and approved for the award of a degree by this or any other University.

M. McGuigan

(signature)..

Abstract

Multi-light imaging captures a scene from a fixed viewpoint through multiple photographs, each of which are illuminated from a different direction. Every image reveals information about the surface, with the intensity reflected from each point being measured for all lighting directions. The images captured are known as multi-light image collections (MLICs), for which a variety of techniques have been developed over recent decades to acquire information from the images. These techniques include *shape from shading*, *photometric stereo* and *reflectance transformation imaging* (RTI). Pixel coordinates from one image in a MLIC will correspond to exactly the same position on the surface across all images in the MLIC since the camera does not move.

We assess the relevant literature to the methods presented in this thesis in chapter 1 and describe different types of reflections and surface types, as well as explaining the multi-light imaging process. In chapter 2 we present a novel automated RTI method which requires no calibration equipment (i.e. shiny reference spheres or 3D printed structures as other methods require) and automatically computes the lighting direction and compensates for non-uniform illumination.

Then in chapter 3 we describe our novel MLIC method termed Remote Extraction of Latent Fingerprints (RELF) which segments each multi-light imaging photograph into superpixels (small groups of pixels) and uses a neural network classifier to determine whether or not the superpixel contains fingerprint. The RELF algorithm then mosaics these superpixels which are classified as fingerprint together in order to obtain a complete latent print image, entirely contactlessly.

In chapter 4 we detail our work with the Metropolitan Police Service (MPS) UK, who described to us with their needs and requirements which helped us to create a prototype RELF imaging device which is now being tested by MPS officers who are validating the quality of the latent prints extracted using our technique.

In chapter 5 we then further developed our multi-light imaging latent fingerprint technique to extract latent prints from curved surfaces and automatically correct for surface curvature distortions. We have a patent pending for this method.

Acknowledgements

I would very much like to thank my family and friends, who have been a constant source of support and encouragement throughout my PhD. I would also like to thank my supervisor Jacqueline Christmas for her invaluable guidance, direction and supportive words throughout my PhD (as well as the countless coffees she got me!).

I would like to dedicate this thesis to my nephew Leo and my cat ('the cat') who are pictured above.

Contents

List of Figures

Publications

Journal papers

McGuigan, M., and Christmas, J. (2022). Contactless automated lifting of latent fingerprints from difficult curved surfaces. In Signal Processing: Image Communication (Vol. 109, p. 116858). Elsevier BV.
https://doi.org/10.1016/j.image.2022.116858

McGuigan, M., and Christmas, J. (2020). Automating RTI: Automatic light direction detection and correcting non-uniform lighting for more accurate surface normals. In Computer Vision and Image Understanding (Vol. 192, p. 102880). Elsevier BV.
https://doi.org/10.1016/j.cviu.2019.102880

Conference paper

McGuigan, M., and Christmas, J. (2020). Remote Extraction of Latent Fingerprints (RELF). In 2020 International Joint Conference on Neural Networks (IJCNN). 2020 International Joint Conference on Neural Networks (IJCNN). IEEE.
https://doi.org/10.1109/ijcnn48605.2020.9207376

Patent

Some of the material in chapter 5 has led to growing interest from law enforcement agencies (LEAs) and the University of Exeter has filed a priority UK patent.

M. McGuigan and J. Christmas, "Latent Print Extraction Apparatus and Method", priority UK patent filed (application number *GB2110863.4*)

Talks

“Remote Extraction of Latent Fingerprints (RELF)”, Home Office Security and Policing 2021 - The Official UK Government Global Security Event, (9-11 March 2021), UK. (*Selected as only one of ten short talks from across the UK*).

“RTI – using mathematics and off the shelf camera optics to obtain high resolution surface topography”, IONS Exeter Conference (9-12) July 2019. University of Exeter, UK

“Non invasive fingerprint extraction from specular surfaces using computational imaging”, The Smart Industry Workshop; ’Recent Advances in Industrial Digitalisation, Robotics and Automation’, (9-11 January 2019), Nottingham Trent University, UK.

“Accurate Surface Normals From Photographs Using Computational Imaging”, 2018 Society for Industrial and Applied Mathematics (SIAM) Annual Meeting (AN18), (9-13 July 2018), Oregon Convention Center (OCC), Portland, Oregon, USA.

Introduction

Multi-light imaging collections (MLICs) capture a scene from a fixed viewpoint through multiple photographs, each of which are illuminated from a different direction. A variety of techniques have been developed over recent decades to acquire information from the images. These techniques include *shape from shading*, *photometric stereo* and *reflectance transformation imaging* (RTI).

Multi-light imaging collections are processed using RTI to estimate surface reflectance towards the camera from *any* lighting direction, including 'unseen' lighting directions not captured during imaging. This reflectance estimation in RTI also allows for a simulated relighting of the scene with a virtual torch. RTI has many applications [56] particularly in the cultural heritage community [16]. The technique is an inexpensive tool for conservation imaging, allowing for the fine details of cultural artefacts to be captured and enhanced using surface normals and virtual relighting to reveal nearly invisible features.

Surface normal vectors may be estimated at each pixel location using RTI, however due to the false assumption of a uniform light source these surface normals are often inaccurate since in reality it is not possible to generate perfectly uniform illumination. RTI falsely assumes that all surfaces in a scene are Lambertian, and also requires the use of calibration equipment (i.e. shiny reference spheres or 3D printed structures).

To address this we present a novel automated RTI method in chapter 2 that removes the need for calibration equipment and structures that other methods require, and we automatically compute the lighting direction and compensate for non-uniform illumination.

We also harness the non-contact nature of multi-light imaging to provide a rapid method for automated remote latent fingerprint extraction (RELF). Current fingerprint extraction techniques are invasive and use chemicals to enhance the fingerprint visibility whilst simultaneously rendering the fingerprint unusable for further forensic testing such as DNA analysis, and involve various time consuming manual tasks.

During our work on our remote fingerprint extraction technique we collaborated with the Metropolitan Police Service (MPS) UK, as they described to us their needs and requirements which helped us to create a prototype contactless fingerprint imaging device which is now being tested by MPS officers who are validating the quality of the latent prints extracted using our technique.

We then further developed our multi-light imaging latent fingerprint technique to extract latent prints from curved surfaces and automatically correct for surface curvature distortions in chapter 5.

In summary, the novel contributions of this thesis (also shown in Figure 1) are as follows:

• A fully automated RTI technique for correcting common lighting errors and markedly improving the accuracy of surface normal estimation, as well as increasing the legibility of low relief surface variations whilst requiring no calibration equipment.

• Remote Extraction of Latent Fingerprints (RELF) - a rapid, automatic, zero-contact and chemical-free method which is able to obtain high quality fingerprint images. RELF produces results comparable to existing invasive methods and leaves the fingerprint sample unaffected for further forensic analysis, using machine learning to identify partial fingerprints between successive images and mosaics them.

• An automated surface curvature distortion correction technique which improves fingerprint matching scores for fingerprints extracted using RELF, often significantly. This technique corrects for curvature distortion from a range of objects commonly found at a crime scene that are (forensically) difficult due to their curvature, shininess and/or transparent (such as glass lightbulbs and chrome water taps).

• The development of a handheld prototype capable of capturing multi-light imaging collections of surfaces containing fingerprints to then be processed using the RELF algorithm. The device was developed in collaboration with the UK Metropolitan Police Service then tested to find fingerprints on a variety of surfaces, including difficult curved and specular surfaces such as lightbulbs as well as vehicle bodywork.

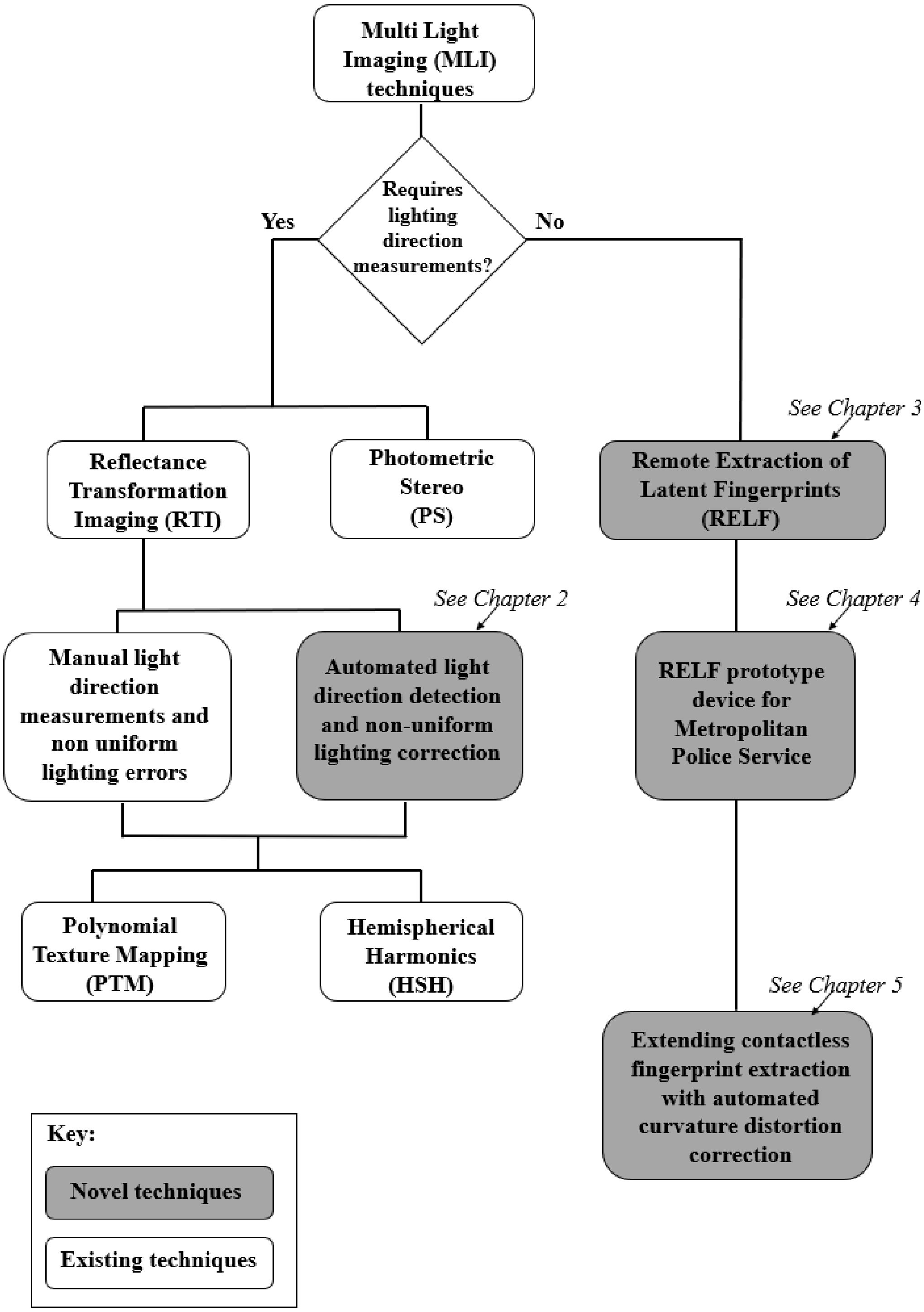

Figure 1: The hierarchy of techniques and their nomenclature is shown here, with the novel contributions detailed in this thesis shown with their corresponding chapter numbers.

1 Literature review and background

This chapter assesses the literature relevant to the methods presented in this thesis. We describe different types of reflections and surface types, as well as explaining the multi-light imaging process. We also describe techniques that analyse MLICs such as RTI, and explain known issues with the method which we later address in chapter 2. We then describe the outstanding issues facing latent fingerprint extraction and describe how multi-light imaging could be used to resolve some of these problems, before introducing our Remote Extraction of Latent Fingerprint (RELF) technique in chapter 3.

1.1 Reflectance and surface types

A surface's appearance in an image is determined by its material, surface shape and the incident illumination's direction and intensity. In multi-light imaging the lighting direction is changed between images, so it is necessary to understand the interaction between a given surface type and the illumination. A method known as the Bidirectional Reflectance Distribution Function (BRDF) was developed for modelling the light intensity reflected from a surface under different lighting directions [21]. We describe the BRDF in section 1.1.1, then in 1.1.3 we describe diffuse reflections, and in 1.1.4 we describe specular reflections and in 1.1.5 we describe real world surfaces.

1.1.1 Bidirectional reflectance distribution function (BRDF)

The BRDF is key to understanding the response of a given surface to incident illumination. The function describes the reflectance of a surface as a function of lighting direction and viewing position [21].

The characteristics of how a surface reflects light may be defined by its 4D BRDF, which captures the intensity of light observed at all viewing directions. The four dimensions of the BRDF are made up of the 2 dimensions of the incident direction which are described by both its azimuth and zenith angles, (θ_i, ϕ_i), and the 2 dimensions of the outgoing direction which is also described by both azimuth and zenith angles, (θ_r, ϕ_r). Different materials will reflect light differently. Glossy surfaces exhibit specular reflections and matte surfaces exhibit diffuse reflections, resulting in the BRDF of these materials being very different.

The BRDF is also dependent on wavelength (and therefore colour), so often in computer vision an independent BRDF is computed per colour channel (red, green and blue in conventional digital cameras). In order to fully measure the BRDF, both incident illumination and viewing angles must be sampled throughout the four-dimensional space which they are described by (across an effective viewing hemisphere).

This would require capturing a very large number of images from many locations under varying lighting directions. This would require the long process of moving the camera around or using many cameras to capture the surface whilst ensuring the precise alignment of the light source and camera for each photo [88].

We see in equation (1.1) the BRDF is defined as the ratio of outgoing radiance, $L(\theta_r, \phi_r)$, in the reflected direction (θ_r, ϕ_r) to the incoming irradiance, $E(\theta_i, \phi_i)$, from the incident direction (θ_i, ϕ_i) [8].

$$BRDF(\theta_i, \phi_i, \theta_r, \phi_r) = \frac{L(\theta_r, \phi_r)}{E(\theta_i, \phi_i)} \tag{1.1}$$

In order to avoid the computation of stereo correspondences for all camera positions a 2D 'slice' of the BRDF can be obtained through holding the camera position constant with respect to the surface and varying only the light direction. The BRDF obeys Helmholtz reciprocity [22], meaning that there is symmetry between incident and reflected directions with respect to the surface normal. The BRDF incorporates energy conservation, meaning that the total power reflected for a given incident radiation direction is less than or equal to the the incident light energy [21].

BRDF measurements are of interest to researchers in many fields such as remote-sensing [77], optical engineering [90], computer vision [19], and computer graphics [57]. In computer vision, researchers are interested in measuring reflectance from a surface to estimate 3-D shape using methods such as shape from shading [39], photometric stereo [93] and reflectance transformation imaging [56]. These techniques will be discussed in more detail in section 1.3. For such methods to function properly, the BRDF must be modelled accurately which may be verified via measurement. The BRDF has a clear application in computer graphics for realistic surface rendering [49].

1.1.2 Bidirectional Texture Function (BTF)

The Bidirectional Texture Function (BTF) was defined by [18] as a texture representation technique which captures variation in texture under varying illumination and viewing directions. In additions to the four-dimensional BRDF, the BTF is also dependent on the local surface coordinates parametrised by u, v.

$$BTF(\theta_i, \phi_i, \theta_r, \phi_r, u, v) \tag{1.2}$$

Unlike the BRDF, the BTF is not equivalent to the ratio of outgoing radiance in the reflected direction to the incoming irradiance. For each photograph of a textured surface the BTF spans the local surface coordinate space u, v, but one photograph merely point-samples the remaining four dimensions. Similar to the BRDF, the BTF requires a vast

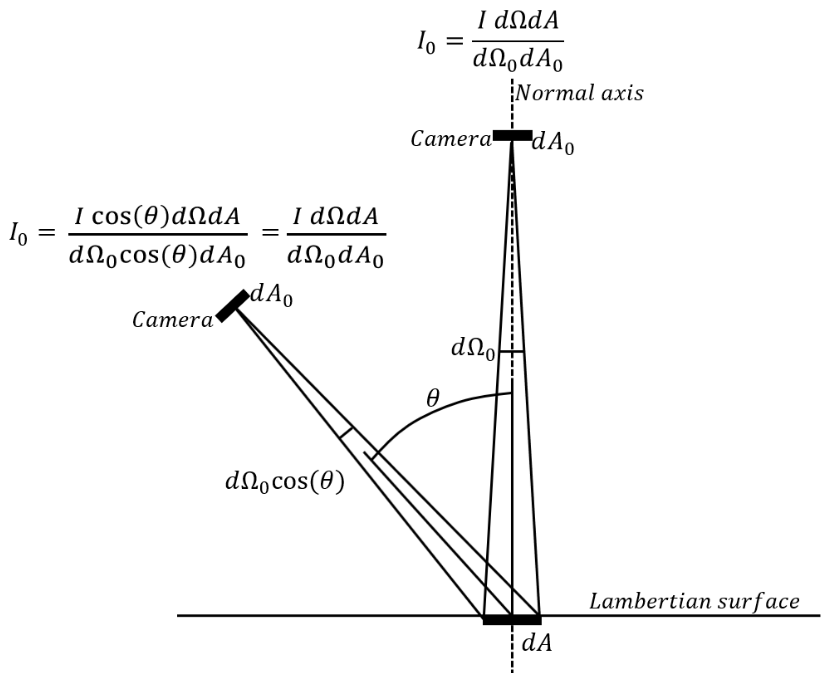

Figure 1.1: Lambert's cosine law for a diffuse surface: the amount of light emitted at angle θ is, I, which is equal to $I_0 cos\theta d\Omega dA$, so the radiance at angle θ is $I_0 cos\theta$, as expressed in equation (1.3).

quantity of images to be taken under different camera and light positions to sufficiently sample this space.

In section 1.3 multi-light imaging is described in detail, where the complication of undersampling high dimensional spaces are avoided by keeping the camera stationary and consequently holding two of these dimensions constant with the fixed reflected light direction, (θ_r, ϕ_r).

1.1.3 Diffuse reflectance

Lambertian reflectors are perfectly matte and reflect diffusely. These materials obey Lambert's Cosine Law (visualised in Figure 1.1), named after Johann Lambert who defined a perfectly diffuse reflector in 1760 [50].

Lambert's cosine law states that the maximum rate of photons emitted per solid angle unit is along the normal axis, and reduces to zero for $\theta = 90°$ as described by equation (1.3). If a camera imaging the scene placed along the normal axis has aperture area dA_0, it will image the diffuse surface element dA which will subtend a solid angle $d\Omega_0$ (where the d prefix represents an infinitesimally small area and solid angle respectively). The number of photons received per second by this camera's aperture along the normal is $Id\Omega dA$.

$$I_0 = \frac{Id\Omega dA}{d\Omega_0 dA_0} \tag{1.3}$$

A camera at angle θ to the normal with the same aperture area dA_0, will see the diffuse surface area element dA from an oblique viewpoint, so the area element dA appears re-

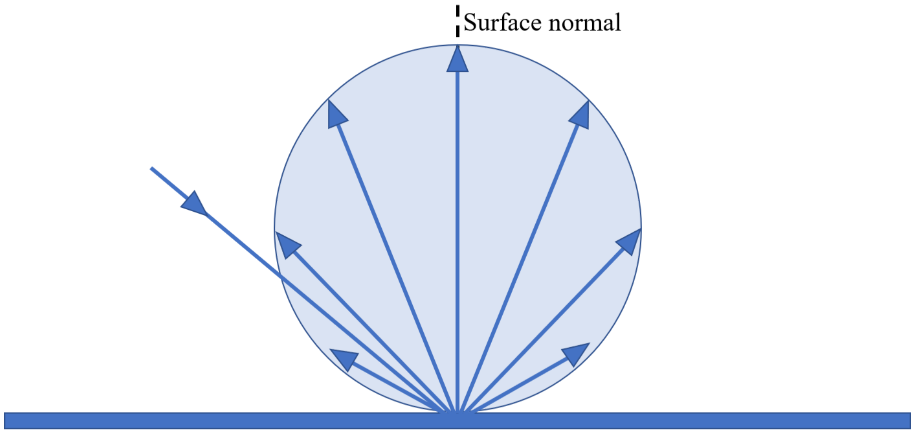

Figure 1.2: Diffuse reflection on a matte surface.

duced and will subtend a smaller solid angle of $d\Omega_0 cos(\theta)$. This camera will be observing $Icos(\theta)d\Omega dA$ photons per second, and so will be measuring a radiance of I_0 as shown by equation (1.4), which is the same as the camera at the normal described by equation (1.3).

$$I_0 = \frac{I\cos\theta d\Omega dA}{d\Omega_0 \cos\theta dA_0} \tag{1.4}$$

Therefore ideal Lambertian surfaces have a uniform BRDF and are equally bright from any possible illumination direction, meaning they will appear equally bright from any viewing direction, since its BRDF is independent of outgoing directions. A uniform BRDF is an assumption made by many computer vision techniques which process multi-light imaging collections [26]. A schematic diagram showing diffuse reflection on a matte surface is visualised in Figure 1.2 and a sampled BRDF measured from a matte (diffuse) surface using multi-light imaging is shown in Figure 1.4a.

1.1.4 Specular reflectance

A challenge for some multi-light imaging techniques in which surface normals are computed such as photometric stereo and RTI (as described in sections 1.3.3 and 1.3.2 respectively) is specular surfaces. This is because unless the camera is exactly positioned at the angle of reflection of the light source then there is no light returned and if no MLIC image is captured at this exact position then the pixel is always black, and so is the measured BRDF. Specular reflections are often too complex for the relatively simple functions chosen to fit to the measured reflectance distributions and these functions can have the effect of muting sharp specularities [67].

Consequently, many computer vision algorithms make the assumption that specular reflections are not present in images, and they generate erroneous results in areas where specular objects exist [53].

The BRDF of a specular surface is not uniform and will appear much brighter from one viewing angle. A sampled BRDF of a specular surface using multi-light imaging is shown

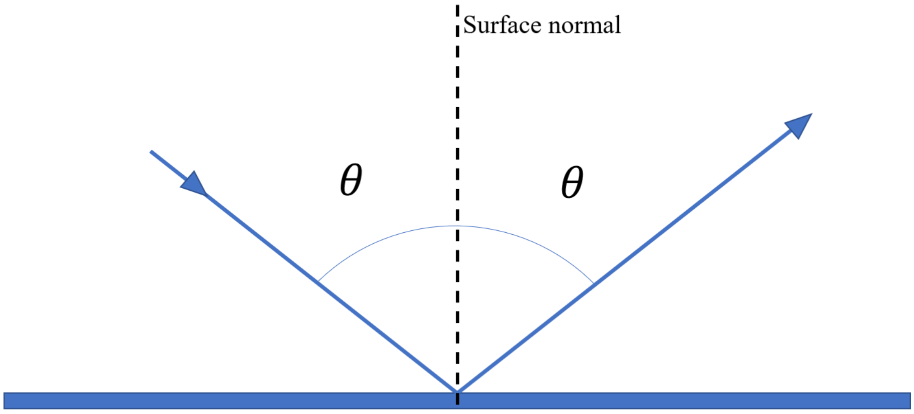

(a) Perfectly specular reflection on a perfectly shiny surface.

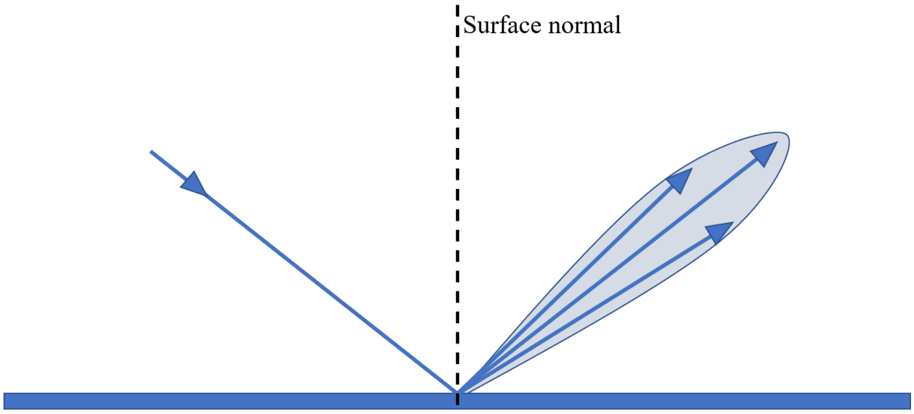

(b) Specular reflection with spread observed when viewing real world shiny surfaces.

Figure 1.3: (a) shows the a perfect specular reflection. (b) an approximately specular reflection as exhibited by real world surfaces.

in Figure 1.4c. As shown in Figure 1.3, specular reflectors obey the law of reflection so that when a ray of light is reflected from a flat specular surface, the angle of incidence is equal to the angle of reflection with respect to the surface normal as contrasted with the diffuse reflection shown in Figure 1.2.

1.1.5 Real world surfaces

In real world scenarios surfaces are often neither entirely specular (no mirror is perfect) or entirely Lambertian, in fact most materials exhibit partly specular and partly diffuse reflectance [17]. So the function chosen to model reflectance can vary depending on the application of multi-light imaging . If most of the regions of interest in the image are diffuse (i.e. a gravestone inscription) then a simpler function may be chosen to model the reflectance (such as a bi-quadratic polynomial). Conversely, if the region of an image is more specular (i.e. a shiny coin) then a more complex function may be selected (such as hemispherical harmonics) [11]. Functions such as bi-quadratic polynomials and hemispherical harmonics are described in section 1.3.4 and section 1.3.5 respectively.

1.2 Multi-light imaging collections (MLICs)

In order to obtain a multi-light imaging collection (MLIC), a camera is fixed in position (the scene must also be static) and each image is lit from a different direction, meaning that each digital image contains the reflectance response of the scene from that particular lighting direction. This collection of images then serves as a 'slice' of the BRDF as described in section 1.1.1.

Other similar photographic techniques such as photogrammetry involve moving the camera whilst acquiring images and also requires processing large amounts of data high-resolution images and computing point clouds [7]. This is both time consuming in the image acquisition and image processing stages. For RTI/MLIC the camera must remain stationary or the process will not work.

In this section we will describe multi-light imaging using a fixed lighting dome as well as freehand multi-light imaging .

1.2.1 Dome based MLIC acquisition

As noted by [56], data acquisition time is short when lighting for each photograph can be performed using a rigid hemispherical structure that contain tens of lights (typically between 20 and 100 lights) which fire automatically and trigger the camera. The number of lights required for capturing an MLIC can vary depending on the complexity of the surface, and more lights can be used to capture additional details and increase the accuracy of the reconstruction. We opt to use 92 lights for our prototype device described in chapter 4 and found that these cost effective LEDs illuminated the fingerprint adequately enough to allow for the extraction of high resolution surface information. In a dome based set-up the camera is rigidly fixed at the dome apex to capture images synchronously with the lights. The illumination directions for the multi-light imaging can be predetermined before imaging since the dome is of known lighting geometry, saving the need for computing the light direction in the processing stage. These devices are known as multi-light imaging domes and can provide a data acquisition time of the order of a few seconds, however this equipment can be expensive and fragile, making it difficult to store and transport.

From the image stack two crucial things are obtained: the direction from which each image was lit, (l_u, l_v), [56] and the associated light intensity emitted at each pixel, L. Note the subscripts u and v here because the light vector is normalised and projected onto the local texture coordinate system (u, v). The reflectance distribution measured for both diffuse and specular surfaces are shown in Figure 1.4a and Figure 1.4c respectively. In these measurement distributions the L value for a given pixel on the imaging sensor is taken from the images and is used to scale the direction vector from which the image was lit.

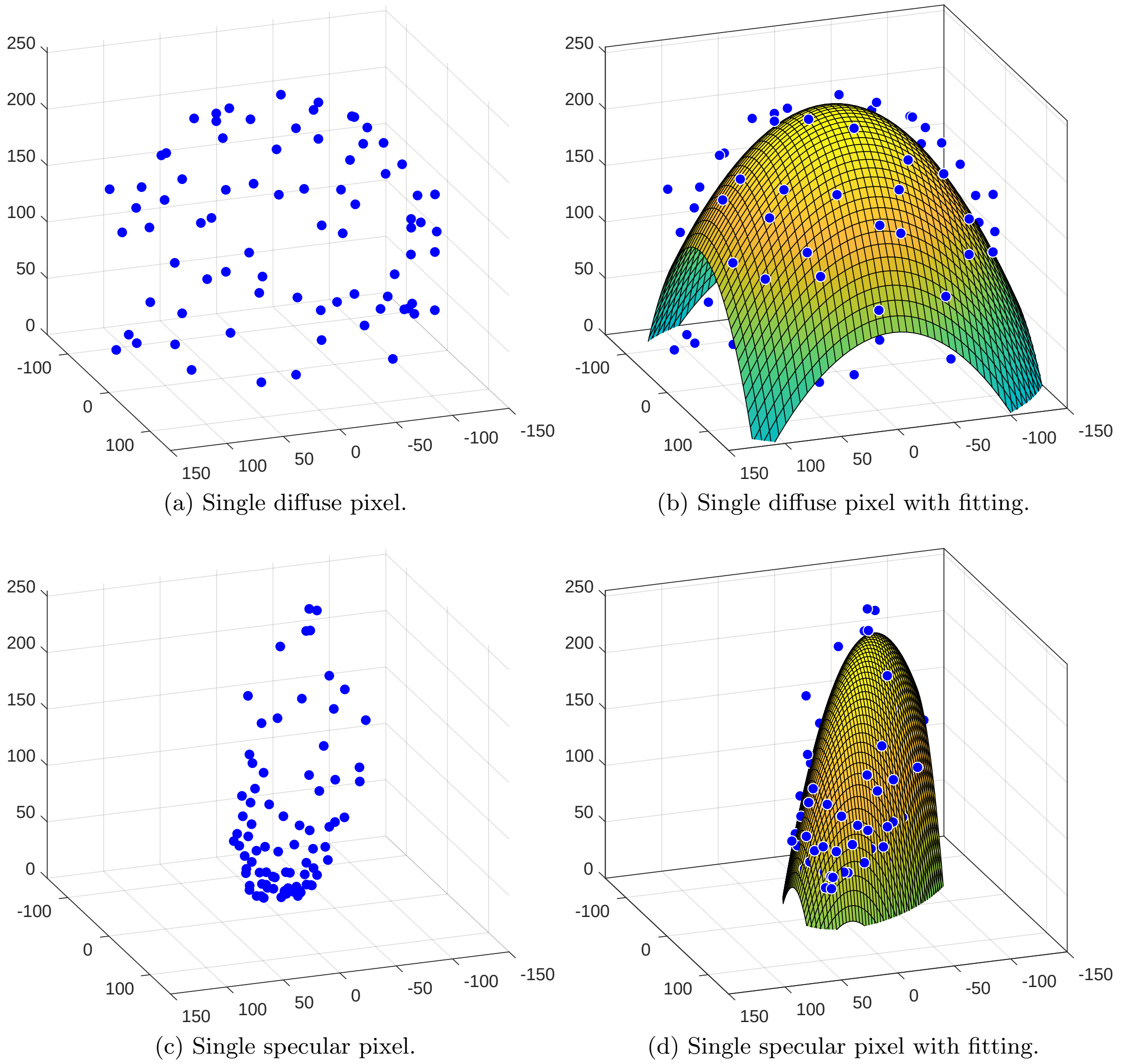

(a) Single diffuse pixel.

(b) Single diffuse pixel with fitting.

(c) Single specular pixel.

(d) Single specular pixel with fitting.

Figure 1.4: In RTI, a bidirectional reflectance function is fitted to the lighting intensity measurements independently for each pixel. In each of the four plots, the points represent the measurements, with the distance from the origin representing the intensity measured when the pixel is lit from that direction. (a) and (b) show results for a diffuse (matte) material as is shown schematically in Figure 1.2; the intensity distribution is approximately uniform over the hemisphere. (c) and (d) show results obtained from a more specular material as is shown schematically in Figure 1.3b; the intensity distribution is clearly biased towards a particular direction.

1.3 Multi-light imaging for surface analysis

Through measuring the change in reflectance of a scene under different lighting directions, multi-light imaging can be used to compute surface relief and orientation within a scene.

Since the camera is held stationary, a given pixel with coordinates (x_1, y_1) in the first image of a MLIC, $I1$, will correspond to the same region of space in the scene as the second image in an MLIC, $I2$, as well as all other images in the MLIC.

We describe the intensity of a given pixel in this first image with coordinates (x_1, y_1) as $I1_{(x_1,y_1)}$. This intensity is a measurement of the response of this small region in the scene to light from the direction the image is illuminated from, (u, v).

Direct measurement of the 4-dimensional BRDF and 6-dimensional BTF (as described in section 1.1.2 and section 1.1.1 respectively) requires a vast quantity of photographs to be taken under different camera and light positions for sufficient sampling. In multi-light imaging, these complications are avoided by keeping the camera stationary and consequently keeping two of these dimensions constant with a fixed reflected light direction, (θ_r, ϕ_r). This vastly reduces the amount of photographs and viewing directions required.

1.3.1 Shape from shading

The practice of estimating the shape of a surface using only the variation in intensity from one image is known as shape from shading. The technique was established in 1970, and it was shown that the surface gradient may be determined by solving non-linear first-order partial differential equations [39]. More recent advances in shape from shading show promising results with the use of machine learning to predict surface normals from single image [76], but the method is only shown to work on objects that are entirely white or gray in colour. The original technique makes several assumptions about the overall structure of the surface such as assuming there are no discontinuities in the surface, as well as assuming prior knowledge about the reflectance of the surface (most shape from shading methods assume the surface is Lambertian). The technique describes the image as an intensity function, $I(x_1, x_2)$, which is equal to the assumed reflection function $R(\mathbf{n}(x_1, x_2))$ [40] as shown in equation (1.5).

$$I(x_1, x_2) = R(\mathbf{n}(x_1, x_2)) \tag{1.5}$$

In equation (1.5) $I(x_1, x_2)$ refers to a pixel with coordinates (x_1, x_2) and intensity I in the image and R refers to the reflectance function and $\mathbf{n}$ is the normal vector to the surface. Infinitely many surface orientations may generate the intensity $I(x_1, x_2)$, so further information is needed before the surface orientation can be computed. A solution is found by taking a point within the image plane where the orientation of the surface is known [40]. Given that shape from shading assumes the surface is Lambertian, the reflectance function is then described by the following:

$$R = \cos\alpha = \frac{\mathbf{L}}{|\mathbf{L}|} \cdot \frac{\mathbf{n}}{|\mathbf{n}|} \tag{1.6}$$

where $\mathbf{L}$ is the normalised light direction vector and α is the angle between the surface normal and light direction, meaning the reflectance is highest if light direction is exactly along the surface normal since $\cos 0 = 1$. Known as the brightness equation, (1.6) yields the surface shape when solved [40]. For a given point, shape from shading is capable of computing a contour in gradient space, but cannot compute the local gradient.

Shape from shading is one of the oldest methods to address 3D reconstruction from photographs in computer vision, and the process shares many commonalities with more recent computer vision techniques such as RTI.

1.3.2 Photometric stereo

In 1980, a technique known as photometric stereo was developed for estimating surface normals without the need to solve partial differential equations (such as the brightness equation shown in equation (1.5)) [93]. Shape from shading is a unique case of this method where the data is a singular image. Photometric stereo determines surface normals at each image point in the scene captured using multi-light imaging [93]. The technique uses the fact that the intensity of reflected light from a surface is dependent on the surface orientation with respect to the light direction and the observer to generate surface normals. Photometric stereo makes the assumption that the surface is Lambertian (as described in section 1.1.3) and the light source illuminates the surface with uniform intensity. The Lambertian assumption is found to be untrue in the case of most real world surfaces where some portion of the object will contain a specular element (as described in section 1.1.5). The uniform light source assumption is also incorrect given that artificial light sources cannot generate uniform lighting. This has such an effect that the side of an object nearest the light source will appear brighter, and the farthest side of the object will appear dimmer. These issues are described in more detail in section 1.3.7.

Photometric stereo with one image (shape from shading) is capable of computing a contour in gradient space for a given point, but cannot compute the local gradient [39]. However, if three images are used instead, each lit from a different direction, then the three contours generated share a point of intersection corresponding to the gradient of the surface. For this reason photometric stereo requires 3 or more images to be used [74].

1.3.3 Reflectance Transformation Imaging

Reflectance transformation imaging (RTI) is another multi-light imaging technique [47] which computes surface shape [56]. Furthermore, the method enables virtual relighting of objects and provides tools such as specular enhancement which serves as a way of revealing low relief surface indentations which are otherwise imperceptible. RTI is an umbrella term for reflectance functions fitted on a per pixel basis to reflectance distributions measured dusing multi-light imaging . The most widely known reflectance functions used in RTI are polynomial texture maps (PTMs) [56] and hemispherical harmonics (HSH) [25].

RTI's traditional estimation of surface normals was originally a by-product of the virtual relighting, mainly being used as a method of contrast enhancement or to make sure that the image stack was correctly constructed by inspecting the normals generated to make sure they were broadly sensible. The method also allows for *specular enhancement*, which converts a Lambertian surface into a virtual specular surface using surface normals as we will discuss later in this section. RTI builds on the Bidirectional Reflectance Distribution Function (BRDF) defined by [21] and described in section 1.1.1, which estimates the intensity reflected from a material from a given viewing point and given lighting direction. In a similar manner, RTI approximates the intensity reflected from a material lit from any direction, but keeps the viewing point constant (i.e. the camera is kept stationary) which removes the need for an enormous volume of photographs to sample the viewing position space. RTI falsely assumes that the object is lit uniformly by the light source, a detrimental assumption photometric stereo also makes (these errors will be discussed in more detail in section 1.3.7).

1.3.4 Polynomial Texture Maps (PTMs)

In RTI, the object of interest is photographed under a wide range of lighting directions as possible. The technique assumes that the camera, viewpoint and object are in precisely the same position for each image in the stack, and that the only thing that changes in each image is the *direction* of the illumination [56]. The interactive relighting enabled by RTI makes it possible to view the imaged object under "virtual" illumination directions that were never actually captured in the original stack of photographs.

The light intensity, L, of a given pixel in these virtual images is constructed from a simple bi-quadratic function of the selected lighting direction (specified by the projection (l_u, l_v) of the normalised light vector onto the plane of the photograph), where the coefficients of the function $(a_0, \ldots, a_5)$ are learned from the image stack:

$$L = a_0 l_u^2 + a_1 l_v^2 + a_2 l_u l_v + a_3 l_u + a_4 l_v + a_5 \tag{1.7}$$

In the PTM equation shown in equation (1.7), each pixel's luminance function is learned independently. For a given pixel, maximising L with respect to l_u and l_v enables us to calculate the surface normal vector at that point, giving information about the shape of the surface of the object [56]. The coefficients $a_0, \ldots, a_5$ are computed using singular value decomposition [86] to solve the system of equations shown in (1.8).

$$\begin{bmatrix} l_{u0}^2 & l_{v0}^2 & l_{u0}l_{v0} & l_{u0} & l_{v0} & 1 \\ l_{u1}^2 & l_{v1}^2 & l_{u1}l_{v1} & l_{u1} & l_{v1} & 1 \\ \vdots & \vdots & \vdots & \vdots & \vdots & \vdots \\ l_{uN}^2 & l_{vN}^2 & l_{uN}l_{vN} & l_{uN} & l_{vN} & 1 \end{bmatrix} \begin{bmatrix} a_0 \\ a_1 \\ \vdots \\ a_5 \end{bmatrix} = \begin{bmatrix} L_0 \\ L_1 \\ \vdots \\ L_N \end{bmatrix} \tag{1.8}$$

Different sets of coefficients $(a_0, \ldots, a_5)$ are fitted to the multi-light imaging collection for each pixel and collected in a spatial map known as the Polynomial Texture Map (PTM). The spatial map has the same width and height as each of the original images in the MLIC. Surface normals may be computed at each pixel from the PTM by partially differentiating (1.7) with respect to the local surface coordinates u and v and setting them equal to zero to solve for the maximum:

$$\frac{\partial L}{\partial u} = \frac{\partial L}{\partial v} = 0 \tag{1.9}$$

Solving (1.9) to find the projected surface normal (l_{u0}, l_{v0}), we are left with (1.10) and (1.11).

$$l_{u0} = \frac{a_2 a_4 - 2a_1 a_3}{4a_0 a_1 - a_2^2} \tag{1.10}$$

$$l_{v0} = \frac{a_2 a_3 - 2a_0 a_4}{4a_0 a_1 - a_2^2} \tag{1.11}$$

The surface normal is then given by:

$$\hat{N} = (l_{u0}, l_{v0}, \sqrt{1 - l_{u0}^2 - l_{v0}^2}) \tag{1.12}$$

We will now introduce polynomial texture maps [56], but to avoid confusion RTI will be referred to as as the *process* from which PTMs are *output*. A PTM is a re-lightable texture map that can generate surface normal data using the coefficients from equation (1.7). RTI assumes that the surface material being imaged is diffuse and non-specular (non-shiny), we will explain what the main differences between these material types are.

The PTM aims to improve on the Lambertian model used in photometric stereo by utilising a low-order polynomial to approximate the BRDF [56]. The PTM better models real reflectance than photometric stereo and is capable of incorporating self-shadowing and inter-reflections for diffuse surfaces [56].

The PTM is fitted to the reflectance distribution independently for each spatial pixel in the image. In Fig. 1.4, we show the results of this fitting for two different materials: (a) shows the reflectance distribution measured for a diffuse material which appears spherical and homogeneous because by definition the material reflects roughly the same amount from all directions; (b) shows the same measurements superimposed on the fitted bi-quadratic surface; (c) and (d) show the same for a less diffuse (i.e. more specular or shiny) material where the distribution appears more elongated and drawn-out in one direction. Very specular surfaces reflect light only in one direction, making the distribution more like either a delta function (if that reflection direction is captured in the photographs) or a zero function (if it is not captured). Both of these cases lead to a very poor fit of the bi-quadratic approximation, which is the reason why RTI is not appropriate for very specular materials. Once the six coefficients (a_0 to a_5) for each pixel have been obtained the process can easily be reversed, and input any arbitrary light direction (l_u, l_v) to obtain the luminosity L for any point on the upper hemisphere of the unit sphere. We treat each (R, G, B) colour channel from a source image as three separate images, and compute a different value of L for each colour channel separately, then recombine them as (L_R, L_G, L_B) to create new $LRGB$ virtually relit images. From these coefficients, estimates of the orientation of each pixel within the image are made through computing surface normal data by differentiation in order to find the maximum as shown in (1.9).

Specular enhancement

Specular enhancement is a contrast enhancing method developed by [56] which implements the RTI generated surface normal vector into the Phong Lighting equation [71], shown in (1.13). For a given pixel illuminated from light direction L, the luminance, I, is given by:

$$I = I_a k_a + I_d k_d(\hat{N} \cdot L) + I_s k_s(\hat{N} \cdot H)^n \tag{1.13}$$

The ambient contribution of the Phong model is represented by the ambient light intensity, I_a, which is modulated by the ambient reflection constant k_a. The diffuse intensity, I_d, is modulated both by the diffuse reflection constant, k_d, and the product of the surface normal, $\hat{N}$, with the light direction, L.

The Phong model represents the specular contribution with the third term in (1.13), where I_s is the specular intensity, k_s is the specular reflection constant and H which is the vector halfway between the viewing direction and lighting direction and n defines the shininess. The specular enhancement method computes an artificial image where the specularity is synthetically enhanced. This is achieved by using the $\hat{N}$ computed from RTI using (1.12) for each pixel then proportionately increasing k_s.

An example of a specular enhancement image is shown in Figure 1.5c. This image was generated from a wax impression of the Great seal of Elizabeth I shown in Figure 1.5a we imaged in the Teign Heritage Centre (UK). The seal was used by the monarch during the latter half of her reign between 1596 until 1603, and served as proof that attached documents had been sanctioned or written by Elizabeth I herself. The wax impressions were produced from a bronze seal matrix, meaning they are malleable and hence it is possible that centuries old *plastic* fingerprints (impressions left by fingers pressed in malleable solids) may be present in the wax impression if a finger has come into contact with it. One such potential fingerprint is visible in a region of the wax seal impression shown in Figure 1.5. The extraction of a potentially centuries old plastic print poses an interesting challenge which may be solved using multi-light imaging. The non-contact nature of multi-light imaging is beneficial since the artefact is very delicate.

(a) Colour image.

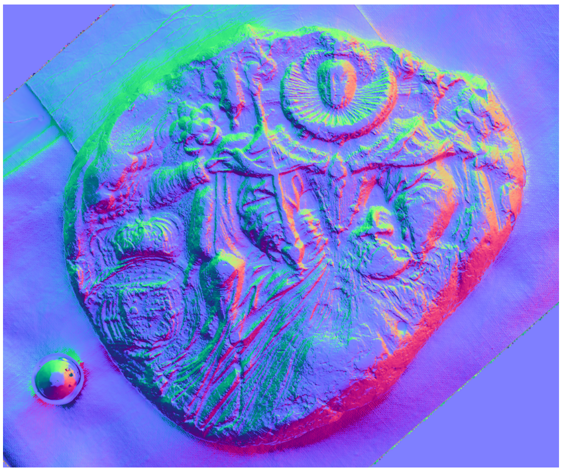

(b) Surface normal image.

(c) Specular enhancement image.

Figure 1.5: A wax impression of the Great seal of Elizabeth I at the Teign Heritage Centre in Teignmouth. (a) shows a colour image of the seal impression. (b) shows the surface normal image of the same seal impression, where the x, y, z components of the surface normal vector each represented by R, G, B respectively. It should be noted that x and y vary from -1 to $+1$, whereas z only varies from 0 to $+1$ which is facing towards the camera, since we cannot observe a surface from behind (facing away from the camera). Here the red edge is facing predominantly to the right, whereas the green edge it facing predominantly to the top. (c) shows the specular enhancement image of the same seal impression, converting a Lambertian surface into a virtual specular surface using surface normals as described in equation (1.13).

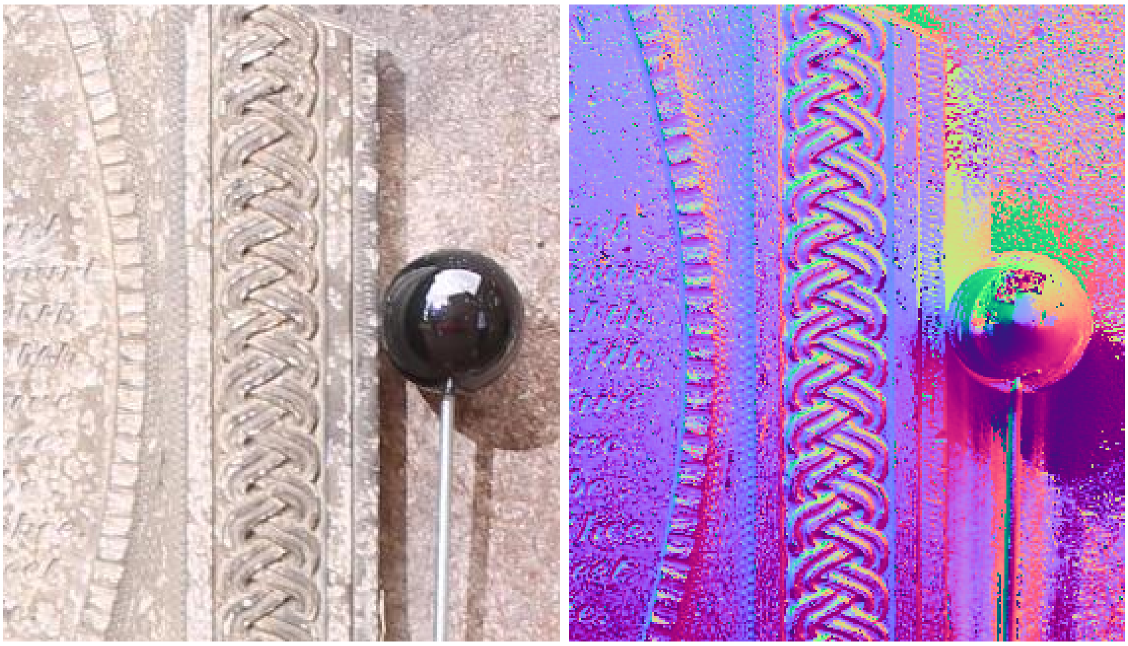

(a) Colour image. (b) Surface normal image.

Figure 1.6: H-RTI requires a shiny reference sphere to be inserted in the scene. (a) shows the colour image of an object of interest, with the reference sphere. (b) shows the erroneous effect that shadowing from this sphere has on the calculated surface normals in the inaccurate green haze (y facing normals) above the sphere.

1.3.5 PTM alternatives

As previously stated in section 1.3.3, RTI fits a function on a per-pixel basis to the measured reflectance distribution at each point, which varies for each pixel depending on the orientation and material at each individual pixel. The bi-quadratic is the original and primary function still used in RTI. There exist other mathematical functions which can be fitted to the reflectance distribution, each of which offer varying numbers of coefficients and fidelity. The most notable of these alternative functions are hemispherical harmonics (HSH) [25] and discrete modal decomposition [73]. These functions offer more degrees of freedom since they have more coefficients than the standard six coefficient bi-quadratic polynomial, meaning they could in theory better fit individual pixels which are more complex (such as specular pixels). However, these functions can suffer from over-fitting and the best results are found when the fitting method is selected on a case-by-case basis, so we opt to use the bi-quadratic polynomial in our method since we will address improvements to RTI in general and is not material specific. It should be noted that the selection of a function for the per-pixel fitting (e.g. PTM, HSH etc) is independent of any light direction estimation or intensity corrections, and that an improvement in light direction estimates would improve any per-pixel fitting.

Laser scanning is a comparable, yet considerably more expensive and complex, topographical imaging technique. It has already been shown that RTI can provide better results than laser scanning for surfaces with very low surface relief [32].

Figure 1.7: The shiny reference spheres used in H-RTI to determine the lighting direction. Each sphere shows a white specular reflection corresponding to the light direction. For example the first image has a specular reflection in its upper right indicating this is the light direction for the whole image, so when we compute the coordinates of this specularity with respect to the sphere centre we are able to calculate a normalised light vector direction.

1.3.6 Highlight RTI - freehand MLIC with calibration spheres

The issue of portability and expense is addressed by [65], who propose a technique whereby the camera is mounted on a tripod and the light source is moved around by hand. A shiny black reflective sphere is placed in the field of view (as shown in Figure 1.6) of the camera and the lighting direction is then determined in the processing stage by tracking the specular highlight caused by the light source on this sphere. Using the sphere, the lighting direction can thus be calculated intrinsically from the RTI image stack itself. This alternative method is known as Highlight RTI (H-RTI), and has aided in RTI's broad appeal to the cultural heritage community since it is inexpensive and requires less knowledge of lighting geometry.

1.3.7 False assumptions and known issues with RTI

The standard RTI method makes several false assumptions which cause inaccuracies in surface normals generated from the technique which we will now describe.

Obstructive calibration equipment

In standard H-RTI a shiny reference sphere (shown in Figure 1.7) is placed in the scene which (to avoid obstructing the object being imaged) is never placed in the centre of the image and often placed at the periphery. This leads to the light directions being heavily biased to wherever the reference sphere is arbitrarily placed. This problem is not addressed in standard H-RTI leading to the majority of RTI users unintentionally and unknowingly inducing errors in their light direction estimates. The sphere itself is obstructive and can cause errors in the fitting process when it casts shadows on the surface being imaged. This type of obstruction-induced error is show in the surface normal image in Fig. 1.6, where a sphere is placed next to the object for RTI and the shadows have clearly degraded the surface normal estimates.

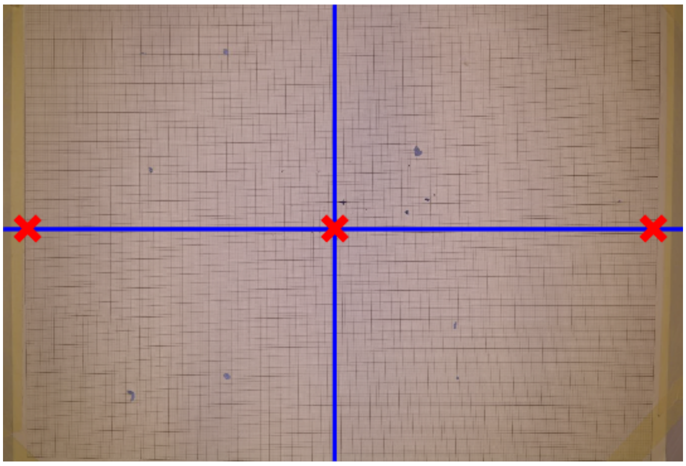

(a) Image of flat diffuse surface where the origin is at the centre.

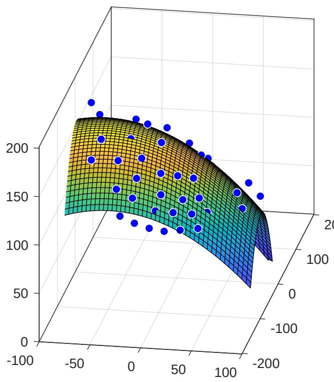

(b)

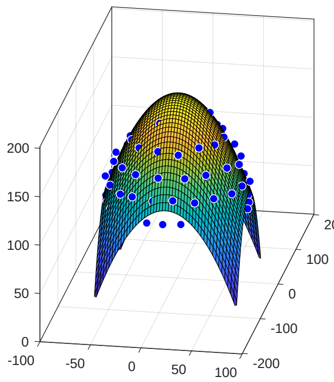

(c)

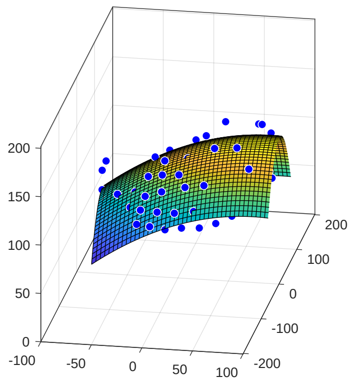

(d)

Figure 1.8: A demonstration of the lighting problem with RTI. (a) shows the colour image of a flat, diffuse surface (white graph paper) photographed using an RTI dome, overlaid with x and y axes. The camera is located above the origin (the centre cross); the three crosses mark the positions of three selected pixels. (c)–(d) show the reflectance distributions measured and fitted at the three selected pixel locations (left, centre and right respectively) marked by crosses in (a). For each pixel, the material and orientation are the same, but the distributions appear to be facing different directions due to different amounts of non parallel light received.

Falsely assumed collimated light rays

The inaccuracies in standard H-RTI become more noticeable for larger artefacts and image scenes, since light rays diverge more with respect to distance. Due to the very nature of light propagation, it is impossible to artificially produce exactly collimated light (light consisting of exactly parallel rays). Some light sources are considered to be approximately collimated, when the radius of curvature of the spherical wavefront is sufficiently large (i.e. the source is sufficiently far away) that when the wavefront is incident it can be considered flat and an approximate plane wave [91]. Laser light is more parallel than traditional light sources, but still suffers from beam divergence due to diffraction [4] and is also impractical for RTI since a laser beam width is so small.

The effect of this variation in intensity in RTI is demonstrated for a flat, Lambertian surface in Fig. 1.8 where fitted lighting distributions are shown measured at 3 different pixels which should be identical as they have identical orientation. Their RTI polynomial

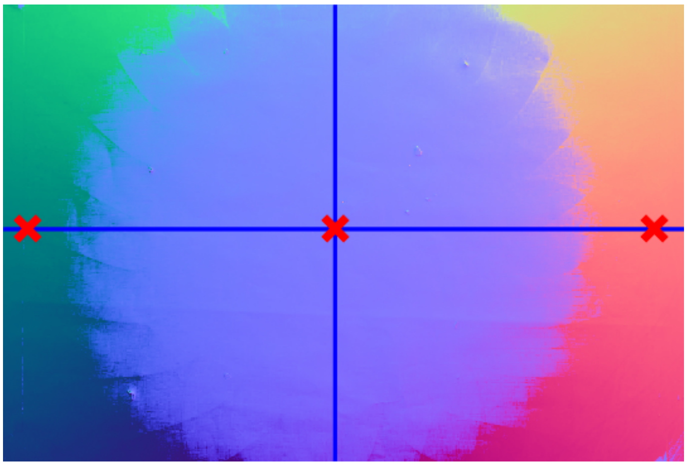

(a) The standard surface normal image generated from Fig. 1.8a.

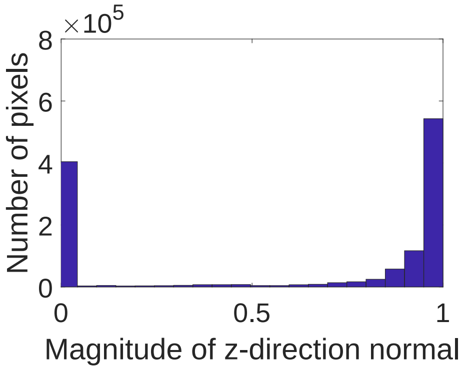

(b)

Figure 1.9: (a) shows the inaccurate surface normal data generated from the flat surface shown in Fig. 1.8a. One may be tempted to assume these errors are caused by vignetting, but we know this is not true because if we remove images lit from a low angle that the effect disappears. This means the effect is in fact caused by low elevation lights in RTI which are disproportionately illuminating the borders of the image. This image should be an even blue colour; the central ring effect is caused by errors from non-uniform lighting. A histogram of the z component of the surface normals across the whole image is shown in (b). This should only show a sharp peak where the z-direction normal equals 1 (surface normal facing the camera), but instead we also see a peak at 0 (surface normal perpendicular to the camera).

fittings have been plotted. These three pixels should have the same reflectance distribution (Fig. 1.8c is correct for a diffuse pixel facing the camera), but it can be seen that the left and right hand side pixels (Figs. 1.8b and 1.8d) show significantly different distributions. The differences visible in the plots in Figs. 1.8b, 1.8c and 1.8d are in fact due to the fact they are nearer in proximity to the light source when low elevation light images are taken and hence experience much stronger intensity. RTI somewhat naively fits a polynomial to the reflectance distribution which assumes that each pixel has been lit equally and uniformly. This is further demonstrated by the surface normal image generated in Figure 1.9a which shows the inaccurate surface normal data generated from the flat surface shown in Figure 1.8a. One may be tempted to assume these errors are caused by vignetting, but we know this is not true because if we remove images lit from a low angle that the effect disappears meaning the effect is in fact caused by low elevation lights in RTI which are disproportionately illuminating the borders of the image. Figure 1.9b shows a histogram of the z component of these surface normals across the whole image where

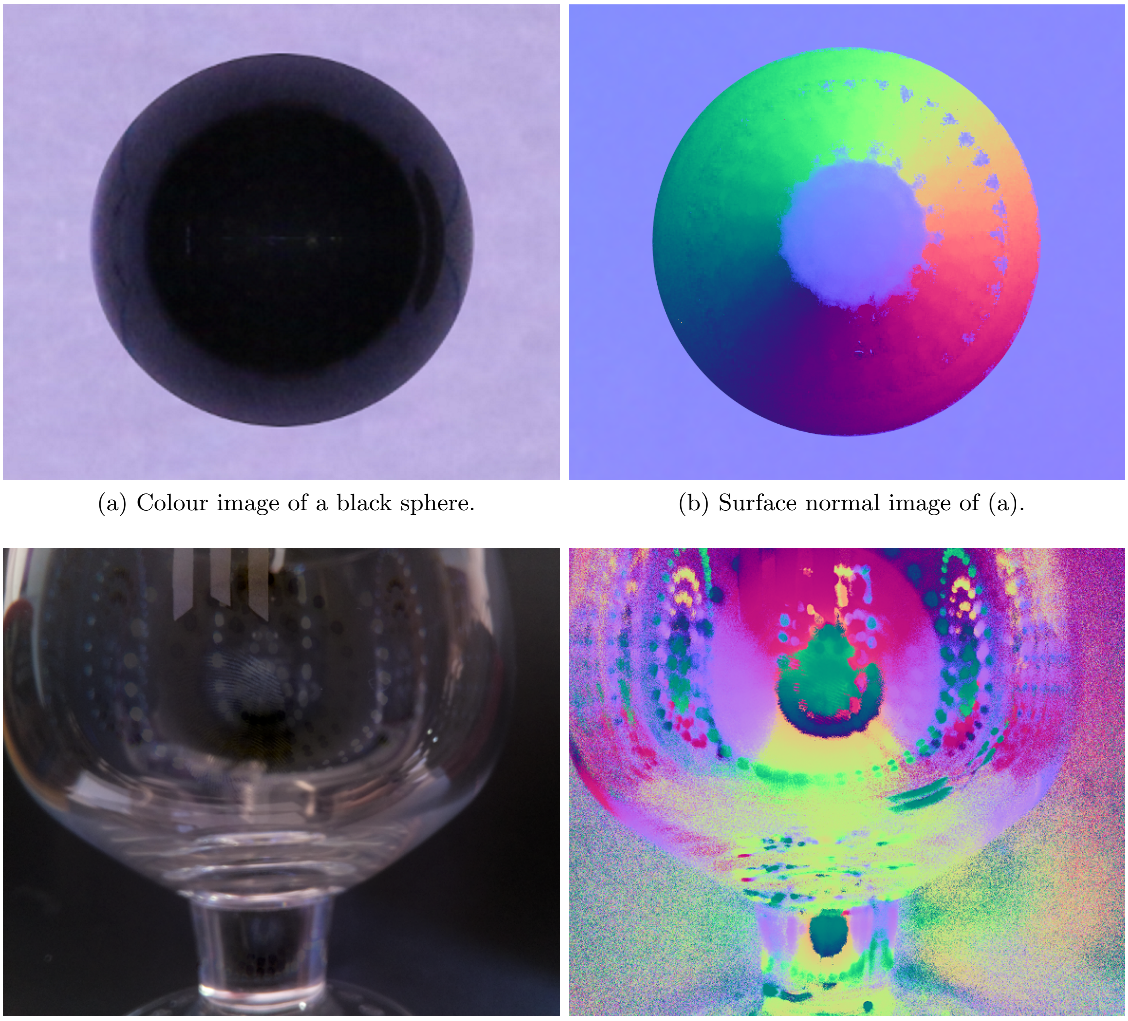

(a) Colour image of a black sphere.

(b) Surface normal image of (a).

(c) Colour image of a drinking glass.

(d) Surface normal image of (c).

Figure 1.10: Specular surfaces which RTI does not perform well on. (a) shows the colour image of an object of a specular sphere. (b) shows the surface normals from RTI of the specular sphere computed using (1.12). (c) shows the colour image of an object of a specular drinking glass. (d) shows the surface normals from RTI of the specular drinking glass computed using (1.12).

there should only show a sharp peak where the z-direction normal equals 1 (surface normal facing the camera), but instead we also see a peak at 0 (surface normal perpendicular to the camera).

This is the crux of the problem: regular light sources simply do not spread the light evenly enough. Standard H-RTI neglects both non-uniform intensity and non parallel rays, which can result in extreme errors in surface normal estimates as will be shown in chapter 2.

Poor performance on specular surfaces

Specular surfaces (described in section 1.1.4) are a problem for RTI since the camera must be exactly positioned at the angle of reflection of the light source in order to accurately measure the specular reflectance. This is a problem since unless an MLIC image is captured at this exact position then the measured BRDF will appear as zero. In an attempt to address this issue RTI simply makes the assumption that specular reflections are not present in the image, and assumes that the surface is approximately Lambertian (with a BRDF similar to Figure 1.4a). This generates erroneous results in areas where specular objects exist [53]. Specular surfaces have highly non-uniform BRDFs, an example of which is shown in Figure 1.4c.

The erroneous RTI surface normal images of specular objects generated using RTI's false assumption of Lambertian surfaces are shown in Figure 1.10. The specular sphere shown in Figure 1.10a produces surface normals which are similar to a cone shape with a flat top, and the drinking glass shown in Figure 1.10a produces patchy surface normals with many noisy image artefacts present. Clearly these surface normal images are inaccurate, since both objects have smooth and continuous surfaces and the incorrect surface normals appear to more similar to a discontinuous non-uniform surface.

1.4 Applications of multi-light imaging

Multi-light imaging methods have been used to provide solutions for a number of imaging problems in different fields. The significant reduction in price of digital cameras and remote lighting devices has meant the technique enjoys a growing number of applications in recent years.

RTI has been accessible to the cultural heritage and archaeological communities thanks to the availability of the *PTM Fitter* [37] together with a user interface, *RTI Builder* [16], which are used to preprocess the RTI image stack to calculate the lighting directions. The *RTI Builder* is also accompanied by *RTI Viewer* [16] which allows for virtual relighting (shown in Figure 1.11)and surface normal generation in an easy-to-use interface for end-users. The image in Figure 1.11a shows a coin virtually relit using RTI Viewer, from the default lighting position (as if the image were lit from the camera position). This lighting position is entirely virtual since it is impossible to light the object from the exact direction of the camera, so RTI make it possible to simulate 'unseen' lighting positions of the object. In Figure 1.11b we see the coin virtually relit under an arbitrary lighting position for comparison. The specular enhancement image is shown in Figure 1.11c where the image's specularity is superficially enhanced as described in section 1.3.4. In Figure 1.11d we see the surface normals of the coin from RTI computed using (1.12). These tools in RTI Viewer enable for detailed inspection of objects, with fine details and surface relief that is invisible to the naked eye being revealed. This allows for the virtual inspection of precious heritage artefacts to the cultural heritage community across the world simply by downloading the RTI file.

Multi-light imaging has been shown to produce promising results as a tool for failure analysis of structural components and materials in engineering [14]. The authors found that RTI surface normal images can be used to distinguish characteristics indicative of component failure such as surface fractures from the range of around 10 micrometers to 10 millimetres. Researchers have also shown RTI may be used for the study of archaeological bone specimens though revealing surface modifications on ancient bone using RTI virtual

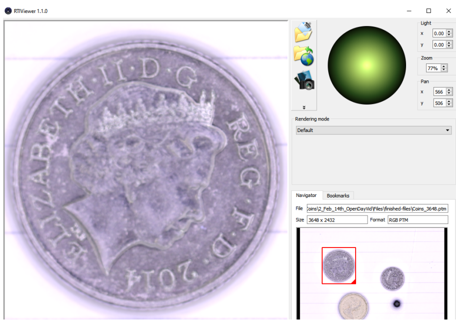

(a) Object virtually re-lit from position of camera (which is not possible to view in practice or light source would obstruct camera view).

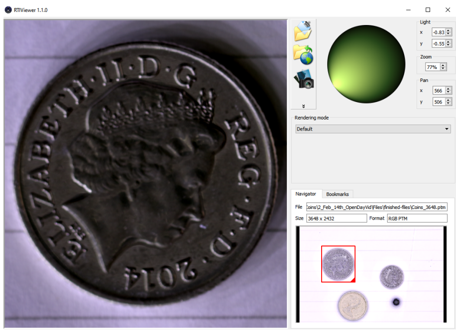

(b) Object virtually re-lit so virtual light source is placed at lower left of object.

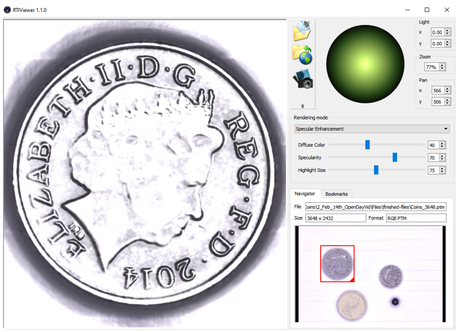

(c) Specular enhancement image.

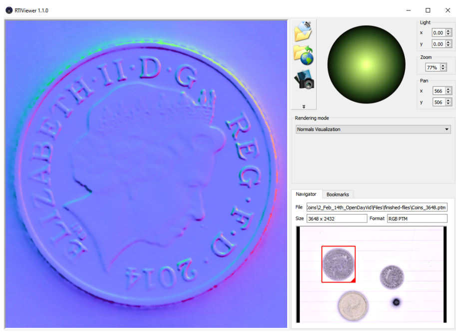

(d) Surface normal image.

Figure 1.11: The *RTI Viewer* [16] allows for virtual relighting and surface normal generation in an easy-to-use interface for end-users. (a) shows a coin virtually relit using RTI, from the default lighting position (as if the image were lit from the camera position). (b) shows the coin virtually relit under an arbitrary lighting position. (c) shows the coin in an image where its specularity is artificially enhanced. (d) shows the surface normals from RTI of the coin computed using (1.12).

re-lighting and inspecting surface normal images, offering evidence of ancient human behaviours and natural processes [68]. RTI has also been used to monitor minute surface relief and reflectivity changes at various stages of conservation treatment of ancient coins using specular enhancement and normal visualisation [61]. Researchers found this allowed detection of areas difficult to visualise through the human eye.

1.5 Multi-light imaging and contactless latent fingerprint extraction

Unpublished research indicates that around 10% [9] and 12% [52] of latent fingerprints are detected by visual inspection. It is also noted in [9] that all types of objects may be visually examined, including surfaces at crime scenes due to the non-destructive nature of visual inspection. The authors also note that visual examination should be performed first before any more invasive process and any prints found should be photographed before proceeding. Given that the detection rate of latent prints by visual examination is so low, there is motivation for a photographic technique that could automate this process and increase the detection rate.

As discussed in section 1.3, multi-light imaging can be used to reveal fine surface details by extracting surface normals on a per-pixel basis. Given the difficult nature of latent fingerprint imaging (they are nearly invisible), it is perhaps a natural application for a high resolution surface inspection technique such as multi-light imaging, as noted by [96]. However, as described in section 1.3.7, multi-light imaging methods such as photometric stereo and RTI make the assumption that surfaces are diffuse which poses a problem since latent prints are often found on real world surfaces which may be specular.

Our system incorporates all but one of the different lighting arrangements described in [9], and it is designed to capture latent prints in circumstances in which no latent prints at all are currently being collected.

In this section we will describe traditional methods for extracting latent fingerprints which require chemical processing to make them visible.

It has been standard practice to use fingerprints as evidence for decades in criminal convictions and information security [63]. There are three types of fingerprint used in biometrics: latent, patent and plastic [69]. Latent fingerprints are almost invisible, formed by a dielectric residue left behind from the fingerprint ridges containing water with various salts and organic compounds [66]. Extracting latent prints is further complicated since they may be found on complex curved surfaces. Patent fingerprints are easily visible to the naked eye and are formed when the finger is coated in ink or another similar substance then pressed onto a surface. Plastic prints are three dimensional impressions formed when the finger is pressed into a malleable surface such as wax (as shown in Figure 1.12), paint or soap.

In spite of latent fingerprint extraction being a long established process, invasive techniques are vulnerable to improper collection methods which may cause a loss of information [62]. Latent prints are often enhanced physically for photographs by adding a material which involves ‘dusting’ the scene in the expectation that the powder will become fixed to the residue left behind, and hence become much more visible in any further imaging. This type of chemical processing may degrade or contaminate the evidence, preventing additional forensic testing [54]. Fingerprints are comprised of ridges which may terminate or form bifurcations (diverge from one into two ridges) as well as a variety of other distinctive features formed in the foetus from the fifth month of pregnancy [97]. These features are known as minutiae and usually appear in the fingerprint in unique combinations resulting in one persons fingerprint being clearly discernible from another [42].

Latent fingerprint features are more difficult to match than patent fingerprint features and are more susceptible to scrutiny in courtroom arguments [97]. This is due to the non-ideal surfaces where latent prints are often found. In section 1.5.2 we will also discuss non-contact techniques which preserve the print, but require highly skilled users and expensive laboratory equipment.

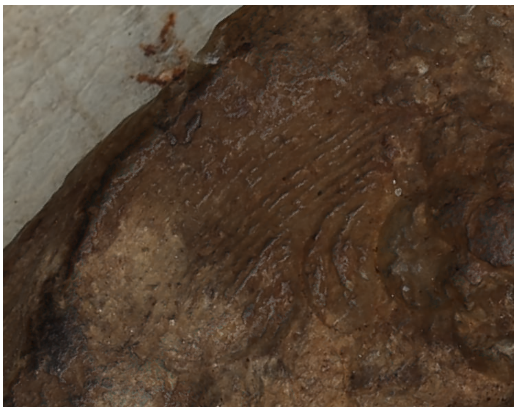

(a) Colour image.

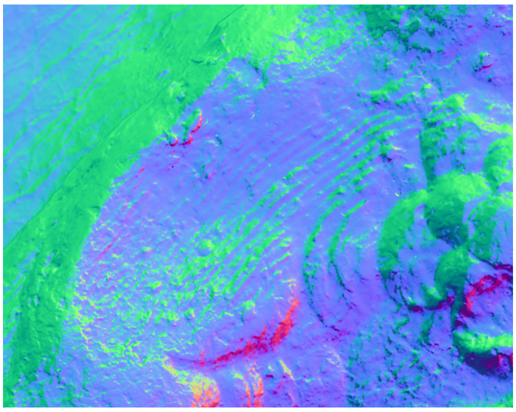

(b) Surface normal image.

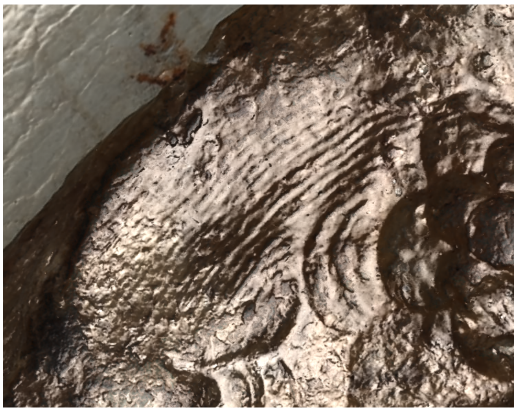

(c) Specular enhancement image.

Figure 1.12: A wax impression of the Great seal of Elizabeth I at the Teign Heritage Centre in Teignmouth (shown in its entirety in Figure 1.5). (a) shows a colour image of the potential plastic fingerprint in the seal impression. (b) shows the surface normal image of the same potential fingerprint in the seal impression. (c) shows the specular enhancement image of the same potential plastic fingerprint in the seal impression

Figure 1.13: Traditional 'dusting' for fingerprints using chemical powder which is designed to become affixed to the latent print residue and not the background surface. This powder enhances the contrast of the latent print with the background surface at the cost of contaminating the print rendering it compromised for DNA analysis.

1.5.1 Current invasive methods

Physical techniques which are contact based and require chemicals to process fingerprints can compromise further investigation from other forensic fields such as drug analysis and DNA testing [45]. Despite potentially hampering additional forensic testing, invasive latent print extraction methods are more traditional and are therefore often more researched with many established procedures and guides in existence [38]. As noted by the UK Government Home Office's Fingerprint Source Book [9], curved and shiny surfaces (both opaque and transparent) pose significant challenges for forensic investigators in extracting latent fingerprints.

The most common invasive latent print extraction method is known as dusting and develops the print using powder (as shown in Figure 1.13). This involves applying finely divided particles that become affixed to the aqueous and oily components in the latent print residue on surfaces [82]. Dusting is ubiquitous in crime scene investigations since it is one of the oldest methods of latent print detection, with one of the earliest references to the technique dating back to 1891 [24].

Many powders rely on two crucial factors to generate adhesion with the latent print residue so that the contrast is enhanced sufficiently and the material does not simply become bonded to the latent print as well as the background surface. The first of these factors is known as pigment and enables better visualization of the fingerprint through increasing contrast and clarity from the background surface. The second of these factors is known as the binder and ensures there is maximum and discriminatory adhesion to the residue of the latent print itself instead of the background surface [59]. Another issue (known as background painting) which may be encountered when using fingerprint powders is when a significant amount of powder adheres to the background surface, obstructing discovery [38].

Gelatin lifting is another physical processing method detailed in the UK Government Home Office's Fingerprint Source Book [9]. The mildly adhesive nature of the gelatin lift makes it suited for the lifting of latent prints from a range of surfaces, but is still highly invasive meaning the print could become altered.

Tape-lifting is another invasive fingerprint extraction method [51] that retrieves small particles from various surfaces. The method has been enhanced through its use in combination with spectroscopic techniques [75], but challenges still face the method such as the complexities behind separating the measured spectral bands which may highly be overlapping due to similar chemical structures [75].

1.5.2 Current reduced contact methods

There exist several methods using expensive optical equipment for non-destructive extraction of latent fingerprints from curved smooth surfaces that can yield impressive results.

Optical coherence tomography (OCT) has been used to extract latent fingerprints from complex surfaces [20]. The authors were able to extract fingerprints from even poorly reflecting samples where the latent print was unnoticeable under ordinary viewing conditions, and they achieved this without any physically invasive or chemically enhanced processing.

Another optical method utilises the fact that specularly reflected light from dielectrics is partially polarised at a specific range of observing angles [54]. Despite producing effective results, the techniques in [54], [20] and [12] are intended for extracting fingerprints from flat surfaces. However, another optical method has been developed specifically to image curved surfaces [48]. As the authors state, the ability to obtain a non-destructive reconstruction of a fingerprint (or portion of it) in situ from a cylindrical or curved surface is important for the purposes of identifying a person at a crime scene. This non invasive method uses a diffractive optical element based glossmeter (a device usually used to measure magazine print gloss quality). The method utilises a motor-driven rotary table to rotate the object being imaged. A laser beam is focused onto the position of the latent fingerprint and colour-coded gloss map of the scanned region is obtained, with colour being related to the strength of light reflection. The latent fingerprint is shown in contrast to the background surface due to a difference in reflectivity. The authors state their method may be encounter issues due to colour affecting the image contrast of the fingerprint [48]. It is worth noting that this technique requires lots of equipment and a highly skilled user.

Researchers have used hyperspectral imaging (which constructs a three dimensional data cube consisting of two dimensional images over numerous wavelengths) to obtain fingerprint images [29]. All channels are fused using histogram of oriented gradient information to weigh each of these channels [94]. These non invasive optical methods produce interesting results, but they are often experimental proof-of-concept setups and require a high level of knowledge and skill to operate the equipment. Other invasive and potentially deleterious methods besides dusting include using hardware such as deformable membranes on glass plates and heating glass plates to remove moisture [97]. Clearly, these methods are very invasive which is undesirable in any forensic investigation as they may risk destroying or contaminating the fingerprint sample.

As stated in the UK Government Home Office's Fingerprint Source Book [9], reduced contact methods used in the UK include multispectral imaging, monochromatic illumination and the use of colour filters show promise but require expensive expert equipment and are also used in tandem with chemical enhancements such as ninhydrin.

All of these described methods rely on complicated, laboratory based equipment that requires careful calibration. Therefore there is clearly a need for a straightforward, non-destructive approach which avoids having to compromise precious forensic evidence. Such a method could extract latent fingerprints without the use of chemicals to develop the prints, as is used in traditional methods. Our method proposed in chapter 3 requires only the operation of an off-the-shelf camera and a remote flash or lighting dome.

2 Automating RTI: Automatic light direction detection and correcting non-uniform lighting for more accurate surface normals

The following article has been published using material from this chapter:

McGuigan, M., and Christmas, J. (2020). Automating RTI: Automatic light direction detection and correcting non-uniform lighting for more accurate surface normals. In Computer Vision and Image Understanding (Vol. 192, p. 102880). Elsevier BV. https://doi.org/10.1016/j.cviu.2019.102880

In this chapter we propose a novel, fully automated technique for correcting common lighting errors in RTI and markedly improve the accuracy of surface normal estimation, leading to an increase in legibility of low relief surface variations. This moves RTI from the qualitative domain (e.g. enabling the reading of weathered inscriptions) into the quantitative domain of computer vision. RTI assumes only light direction, and not received intensity, changes as the object is imaged. Like other authors we show that this assumption is false and propose a novel method to correct for it. However, we estimate the lighting directions automatically, unlike other proposed correction techniques. Our method also requires no calibration equipment, meaning it can be easily retrofitted to any existing multi-light imaging collection. We increase the simplicity of the standard H-RTI method by automatically detecting lighting directions and maintain its appeal to non-imaging professionals.

2.1 Introducing an automated RTI technique

Reflectance Transformation Imaging (RTI) [56] is a photometric stereo technique that enables the interactive relighting of the object of interest from novel lighting directions, and an estimation of surface topography through the calculation of surface normal vectors. The method combines a multi-light imaging collection, of which each image is lit from a different direction, into a new representation (called a Polynomial Texture Map, or PTM, by [56]) that models how the reflectance of each pixel varies by lighting direction. RTI is widely used in the cultural heritage sector as it is relatively easy and inexpensive to perform [65], is supported by free software from Cultural Heritage Imaging[1], and, for

[1] http://culturalheritageimaging.org/What_We_Offer/Downloads/

example, enables the viewer to reveal markings that are not legible, or even visible, from a single photograph [10].

Key to the RTI method is knowing the lighting direction for a given photograph. If the illumination is provided by a fixed lighting dome (see Figure 2.1), then these directions are defined by the hardware. However, much RTI is performed without a dome and with a hand-held flash instead, known as highlight RTI (H-RTI) which was introduced by [65]. The light direction is calculated from the reflection of the flash on a shiny, black, spherical marker, or other calibration devices [27; 41], included in the photographs. The process for creating the PTM depends on accurate light direction estimation and on the assumption that the only difference in the level of illumination in each photograph is caused by the variation in light direction.

We introduce a fully automated RTI technique that improves the accuracy of the surface normal estimation, moving RTI from the qualitative domain towards the quantitative domain. The technique requires no calibration equipment and can be retrofitted to any existing multi-light imaging collection. The proposed method compensates for brighter and darker regions caused by relative distance to the light source, significantly reducing non-uniform lighting errors, automatically detects the light direction from each image photometrically, removing the errors introduced by the bias of the shiny spheres in H-RTI, as well as the obstructive shadows they cause, and removes the need for reflective spheres or other calibration devices through automation, thereby increasing simplicity of RTI and its appeal to non RTI specialists.

We have outlined the relevant background theory behind RTI in section 1.3.3, and in section 1.3.7 we described some of the known inaccuracies introduced by the RTI process. We present our new method for addressing these issues in section 2.2 and then compare the effectiveness of the new method with the standard H-RTI method [65] in section 2.3. RTI assumes a diffuse surface and is usually intended to work for surface relief rather than significantly varying surface heights, however we will also demonstrate in section 2.3 that our method produces improved results on a semi-cylindrical surface. Conclusions are drawn in section 2.4.

2.1.1 Related work

A homogeneous and diffuse surface such as flat white paper is ideal for RTI because white paper is (approximately) Lambertian. For the case when the image subject is not conveniently Lambertian, methods have been proposed by [27] in which 3D printed Lambertian surfaces are physically placed around the border of the scene in order to reveal the spread of illumination and then to measure this photometrically. This method successfully compensates for non-uniform illumination, but requires the insertion of extra physical apparatus and steps. Furthermore, this method may be undesirable because RTI is often performed on fragile artefacts where placing such a structure in the image frame may pose additional risk of damage to an artefact, as well as the fact that this would mean more equipment must be transported.

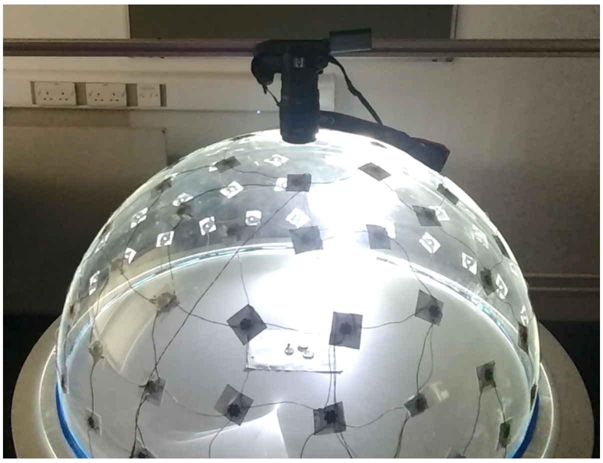

(a) RTI lighting dome of 1 metre diameter and an off-the-shelf Canon EOS 70D camera.

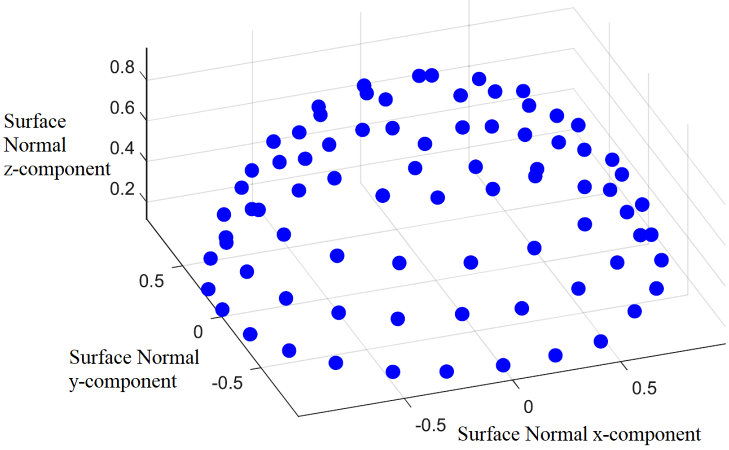

(b) Resulting normalised light directions of the dome.

Figure 2.1: One type of RTI lighting set-up is (a) a hemispherical lighting dome that provides fixed light directions, with the camera looking down vertically on the object. The plot in (b) shows the normalised light directions calculated for this dome.

[41] introduce a promising distance-compensated pixel intensity framework that aims to correct for non-uniform lighting and estimate light directions. However, their method requires a colour-checker calibration target to be placed in the scene, the estimation of 3D scene points, the requirement of initial values for combined albedo and vignetting, and initial surface normal estimates. This could be problematic for imperfect H-RTI multi-light imaging collections, since the method computes initial estimates of surface normals (already known to be potentially inaccurate), and obtains 3D scene point estimates by inputting them into a 3D surface reconstruction technique [3] which relies on sufficiently accurate surface normals to create a gradient map. This 3D surface reconstruction technique has shown very promising results with synthetic data but will only partially recover features in real images [3], missing more intricate details. The method would also likely suffer inaccuracies in arbitrary H-RTI conditions such as the non ideal multi-light imaging collections used in this thesis where initial surface normal estimates are found to be highly inaccurate (see Figure 2.14, left column). Much like [27], the technique proposed by [41] is very effective when multi-light imaging collections meet certain idealised criteria, but it would be impossible to retrofit the method to pre-existing multi-light imaging collections since these techniques require specific items to be placed in the scene. These extra

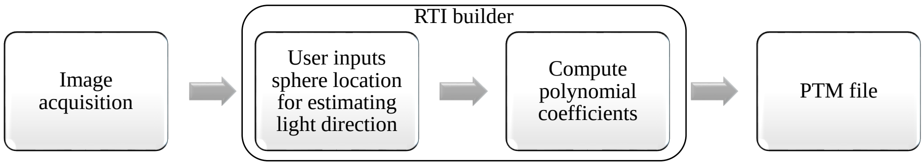

(a) Pipeline of standard H-RTI method.

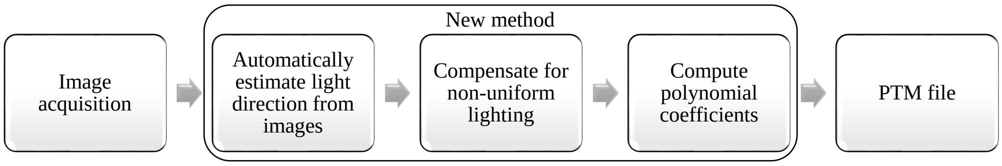

(b) Pipeline of the proposed method.

Figure 2.2: Process diagrams for the standard H-RTI method and the new proposed method.

steps pose potential complications and may be unattainable since the method requires the acquisition of a 3D printed structure. We propose a method that does not require such a structure, but it still relies on RTI illumination being adequately and consistently pointed by hand toward the object, as should be the case anyway.

A similar method to that introduced by [41] is proposed by [92] who use dimensionality reduction to produce estimates of the vectorised light directions. This method relies on the distance between consecutive lighting directions in the multi-light imaging collection being small and requires the use of a diffuse reflector in addition to the light source. Whilst producing approximate light directions in a fast acquisition time, the required manner of lighting may further obfuscate the RTI process to non imaging science users, if, for example the distance between consecutive lighting directions is not small enough. This constraint on RTI would also likely prevent retro-fitting the technique, since H-RTI multi-light imaging collections are often captured from arbitrarily consecutive lighting directions.

For these reasons it became clear that any potential solution must be as automated as possible, with emphasis on keeping the data acquisition process as simple as possible. Hence, a novel method is proposed which corrects for non-uniform illumination, automatically detects the lighting direction and does not require any further steps for the user. The technique in fact aims to minimise the equipment needed since the method proposes a way to automatically detect the lighting direction - removing the need for shiny reference spheres and allowing retro-fitting of our technique to existing highlight multi-light imaging collections.

2.2 Method

To enable us to compute more accurate surface normal vectors for RTI, the sources of error described in section 1.3.7 due to non-uniform illumination will be addressed before any estimates of the surface topography are computed. In order to algorithmically correct for non-uniformity in lighting for a given image, the incident illumination in the image scene

Algorithm 1 Correcting RTI for non-uniformly lit images and improving light direction estimation using the proposed method. The input dataset is a regular multi-light imaging collection and the result is a more accurate estimate of surface normal after corrections for non-uniformly lit images and automated light direction estimation.

for each image, I, in the multi-light imaging collection **do**
  - Generate mean-corrected version of the image, I_c.
  - Fit a bi-quadratic function to the lighting intensity across I_c.
  - Use the fitted function to compensate for over-lit and under-lit regions.
  -Automatically detect lighting direction from artificial mean-corrected image rather than using shiny reference sphere.
end for

must first be characterised. It has been discussed in section 1.3.7 how intensity variations in the light source can be measured photometrically if large enough portions of the image scene are Lambertian. However, this is more difficult since RTI is often performed in arbitrary conditions (often outdoors) when the image scene is very inhomogeneous. Often a given RTI image is comprised of many different objects, and hence surfaces, with different reflectance properties and often at varying distances from the focal plane.

The gravestone in Figure 2.3 was imaged in situ meaning it is impractical to use a lighting dome such as the one shown in Figure 2.1a, so a hand-held flash was used for H-RTI instead. Due to changeable weather conditions and human error aiming the hand-held flash, the images collected were not illuminated uniformly meaning this multi-light imaging collection is a good example for correcting with the proposed method. In order to characterise the non-uniform lighting and then compensate for this across the image the intensity profile being emitted from the light source must be isolated as much as possible from the various surfaces in the image. This is described in sections 2.2.1 and 2.2.2. Once this light profile has been isolated, a 3D function is fitted to the extracted intensity profile of the light source, and used to marginally brighten the under-lit regions, as described in section 2.2.3. Finally, the lighting directions are calculated from these fitted intensity profiles; this process is described in section 2.2.4. Process diagrams for the standard H-RTI method and the proposed method are shown in Figure 2.2 and the algorithm is outlined in algorithm 1.

2.2.1 Isolating intensity variations due to light source

The first step in this process is to isolate the light spread for each source photograph by subtracting the mean image. This is described by (2.1), where I_c is the mean-corrected version of a specific image and is constructed as follows

$$I_c = I - \sum_{n=1}^{N} \frac{I_n}{N} \tag{2.1}$$

where I is a given source image, I_n is the nth image in the multi-light imaging collection and N is the total number of images. This leaves us with an image in which the direction of the incoming light is more perceptible, as shown in Figure 2.3b. Subtracting the mean image removes most of the salient features of the object from the image so we are left with

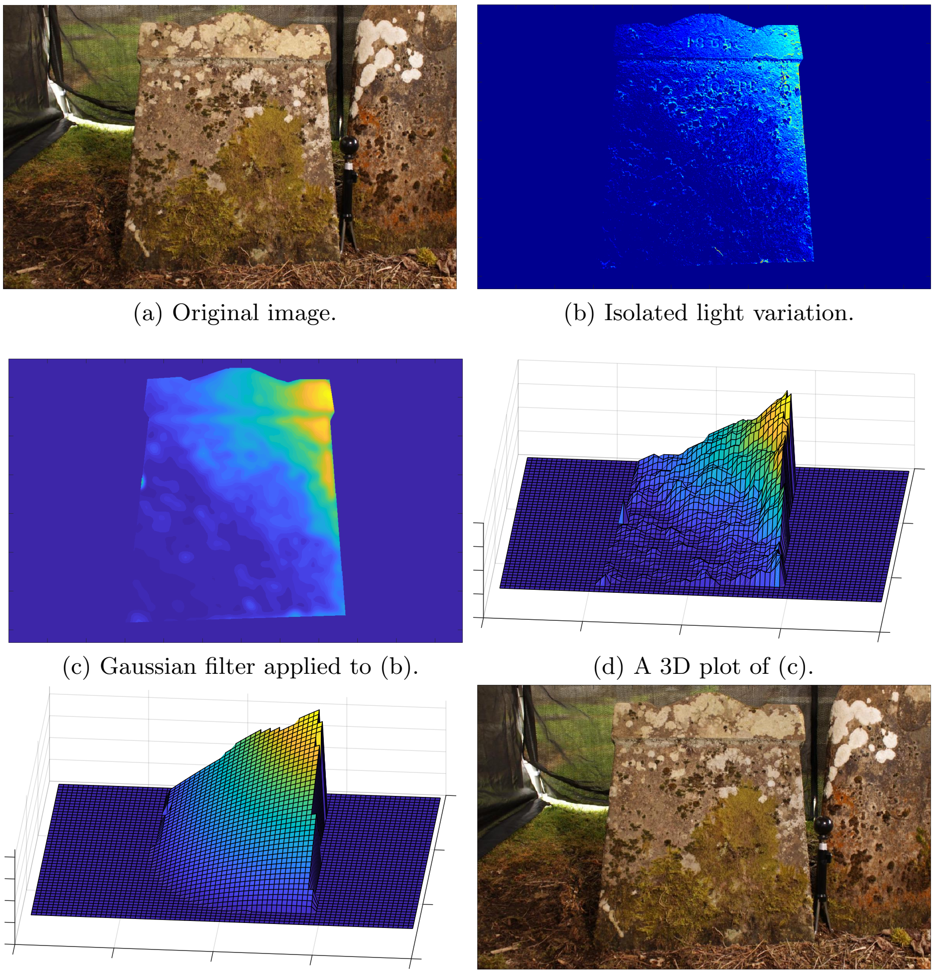

(a) Original image. (b) Isolated light variation.

(c) Gaussian filter applied to (b). (d) A 3D plot of (c).

(e) a bi-quadratic polynomial fitted to (d). (f) The corrected image.

Figure 2.3: An outline of the proposed method applied to a multi-light imaging collection that has been lit somewhat problematically, showing (a) the original non-uniformly lit image, (b) the light spread isolated as the image is mean-corrected and the object segmented from the background, (c) the light spread image after Gaussian filtering, (d) a 3D plot of the Gaussian filtered light spread, (e) a bi-quadratic polynomial function fitted to the light spread, and (f) the intensity-corrected image generated using the function. Note the intensity differences are very subtle and almost imperceptible so as to not overcompensate, but the differences are appropriate to counter the non-uniform intensity problem.

the incident light. A Gaussian filter is applied to this light intensity to smooth out small irregularities, as shown in Figure 2.3c.

2.2.2 Optional: segmentation of object from background

In rare circumstances such as the example in Figure 2.3, objects are imaged from farther back than would be desired and background objects are present whose reflectance is independent of, or only partially dependent on, the RTI light source (such as bright patches of sky). We provide an optional step here to accommodate for these circumstances, and would like to emphasise that there are a large number of image segmentation methods [95]. One such method is the mask R-CNN [36] which efficiently detects objects within images but requires the manual generation of training masks and can require significant computational expense to train. Fortunately, most objects are imaged in RTI so as to fill

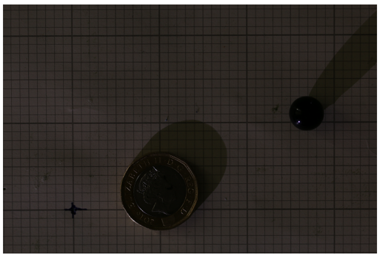

(a) Colour image.

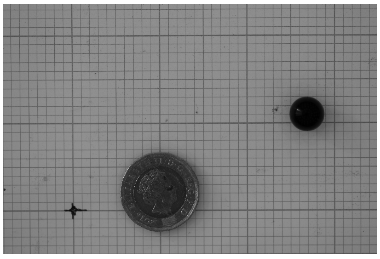

(b) First principle component.

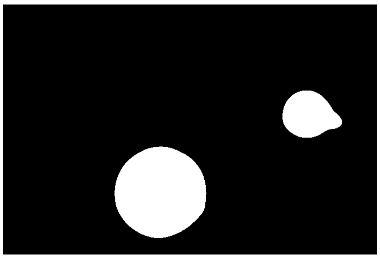

(c) Binary mask from (b).

Figure 2.4: The automated segmentation process proposed uses Principal Component Analysis (PCA) to separate the foreground and background. (a) shows a colour image from a multi-light imaging collection of a coin and black sphere. The first principal component extracted from the multi-light imaging collection is shown in (b) which enables the segmentation of these objects from the foreground through thresholding as shown in (c).

as much of the image frame as possible in order to view the object in higher resolution. The intensity corrections and light direction estimations from the proposed method work without segmentation (see Figure 2.10, Figure 2.11 and Figure 2.9), we simply include this optional step for these special cases.

The automated segmentation process proposed uses Principal Component Analysis (PCA) to separate the foreground and background [33] as shown in Figure 2.4. The first principal component extracted from a multi-light imaging collection of a coin and black sphere is shown in Figure 2.4b which enables the segmentation of these objects from the foreground through thresholding as shown in Figure 2.4c. We add the option for the user to manually segment the object by specifying a bounding polygon through a graphical user interface if they have imaged the object from particularly far away.

2.2.3 Fitting a function to non-uniform light

We choose to fit a bi-quadratic polynomial to each mean-subtracted input image, the same function fitted on the reflectance distributions in section 1.3.4 in the standard H-RTI method [56]. Note that standard H-RTI uses the bi-quadratic to estimate the orientation of a given pixel, but here we fit it collectively to all the pixels in a given image for intensity correction. We also opt to fit the bi-quadratic in this instance because it is fast, adequately flexible and does not require interpolation or physical reference spheres to be placed in the scene as per the method proposed by [27]. Fitting results for one image of a uniformly flat and diffuse surface are shown in Figure 2.5 where the mean-corrected version of the image was generated from the original image to isolate the light source. From here the polynomial function in Figure 2.5b was produced which is in turn used to correct the input image in Figure 2.5a generating the image shown in Figure 2.5c. The full fitting process is shown in Figure 2.3, where it can be seen that the intensity variations due to the light source are isolated from the original RGB image. The polynomial is then fitted as shown in Figure 2.3e, and this is used to marginally increase the intensity of the underlit region. The differences between the original input image and the corrected image are subtle; non-uniform lighting must not be *over* compensated for.We obtain a marginal brightening factor, F, by computing the interquartile range, IQR$(\cdot)$, of the mean-corrected image, I_c

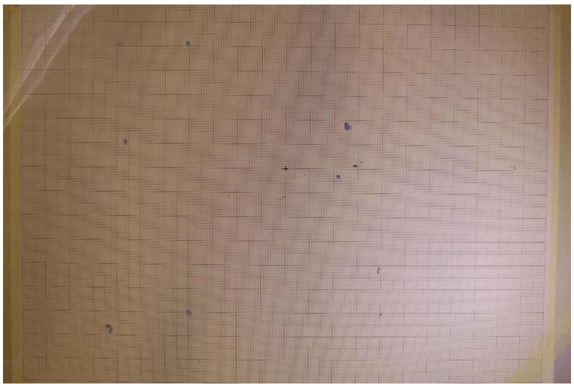

(a) Original image of a flat diffuse surface.

(b) Inverse of function fitted to light variation in (a).

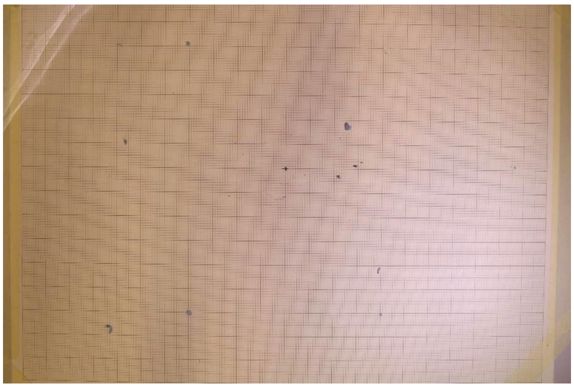

(c) The corrected image.

Figure 2.5: An example of a polynomial function fitted to the isolated light source to correct the light intensity. (a) The original non-uniformly lit image. (b) The inverse of the function fitted to the light variation which is then scaled to correct the image by the process described in section 2.2.3. (c) The intensity-corrected image generated using the inverse function. Note the darker regions in the original image appear marginally brighter in the corrected image.

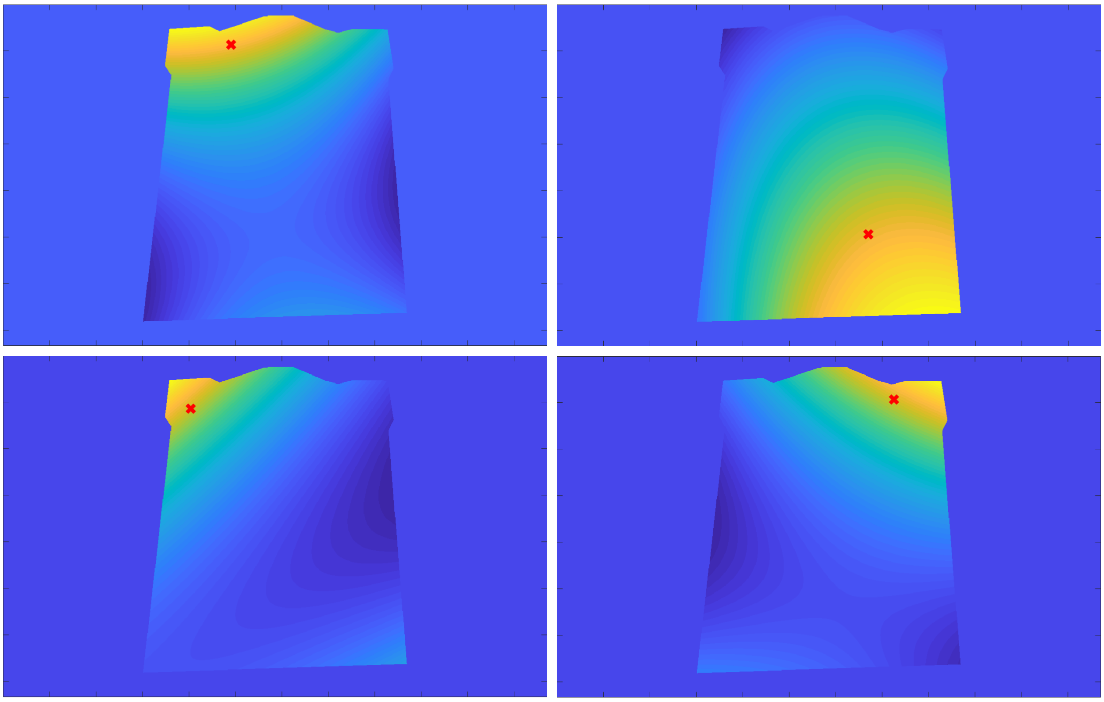

Figure 2.6: Here we see the automated light direction detection method for the gravestone in Figure 2.3. In each image the red cross shows the centroid of the higher value points of the polynomial fit. Here blue represents low intensity and yellow represents high intensity. This function tends to infinity, so we cannot compute it's maximum to yield the light direction. If we compute the maximum within the bounds of the image frame we end up at the image periphery. To address this, we compute the centroid of an upper intensity region within the bounds of the image. The limit of this upper intensity is determined by the process outlined in section 2.2.4.

as shown in (2.2).

$$F = \mathrm{IQR}(I_C) \tag{2.2}$$

$$P_{\text{corrected}} = (1 + F)\, P_{\text{original}} \tag{2.3}$$

Here $P_{\text{corrected}}$ is the corrected intensity value and P_{original} is the is the original intensity value. This measure of variability ensures that F is proportional to the variation (or lack thereof) of incoming light in the image. That is to say that less evenly lit images will have a higher interquartile range, and hence have a higher F. This correction is applied to all RGB colour channels. We assume that for the majority of images in the multi-light imaging collection all pixels receive light from the light source (albeit some regions more than others). A resulting image which has been corrected for non-uniform intensity is shown in Figure 2.3f. It can be seen by inspection that the fitting appears very good at approximating the distribution in light across the image. We will see in section 2.3 that these assumptions are true for a variety of multi-light imaging collections as these marginal corrections in intensity for RTI purposes prove to be effective in producing more accurate surface normal estimates.

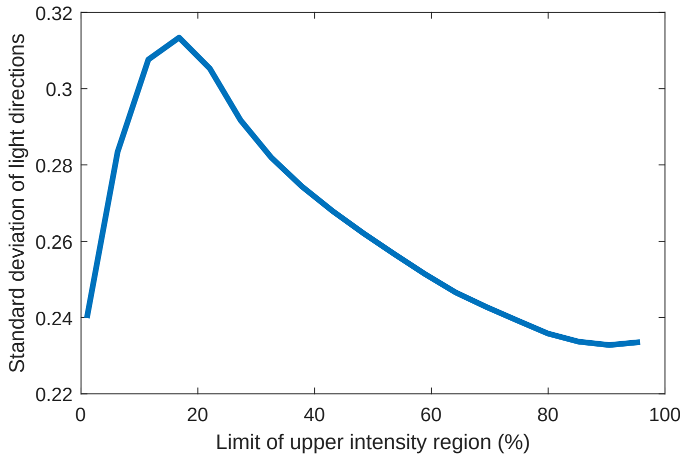

Figure 2.7: As described in 2.2.4, our method thresholds the function fitted to the light variation so we only see a certain portion of the function corresponding to the brightest region of the image, and compute the centroid coordinate of this remaining non-zero portion of the function after thresholding. We compute the centroid coordinate for various threshold percentage cut-off values and select the threshold value which yields the highest standard deviation in lighting directions. We do this because a high standard deviation means the estimated light directions are not clustered around the border of the image, and are more evenly distributed, as per the true directions of the light source. This figure shows this relationship, where it can be seen that the standard deviation increases towards 20% upper intensity, then decreases after this optimum percentage.

2.2.4 Automatic light direction estimation

The proposed approach automatically detects the light direction for all images in the multi-light imaging collection, removing the need to insert a reference sphere into the scene. When estimating the light direction in a given image, one may be tempted to compute the coordinates of the maximum point of the fitted function (introduced in section 2.2.3), extracting the highest value point as shown in Figure 2.6. This is because one may be tempted to assume the highest value point of a resulting fit for an image could be approximately equal to where the light source is located, and could yield the direction of the light for a given image. However, it is not possible compute the global maximum point if the function tends to infinity, as often occurs during fitting. Similarly problematic, if we apply mathematical boundaries to the function (the image borders) and locate the maximum point of the function, we obtain no meaningful information when the function tends towards infinity since the maximum point will always lie somewhere on the border of the image. We propose an efficient method for estimating light direction by computing the centroid (mean coordinates of a group of pixels) of the upper intensity group of points on the fit. This value is much more meaningful, having a more realistic correspondence to the source images than the global maximum. It was found that the optimum percentage of upper intensity for computing this centroid was different for different scenarios, so we produce a robust method which finds this optimum percentage automatically.

Our method thresholds the function fitted to the light variation so we only see a certain portion of the function corresponding to the brightest region of the image, and compute the centroid coordinate of this remaining non-zero portion of the function after thresholding. We compute the centroid coordinate for various threshold percentage cut-off values and

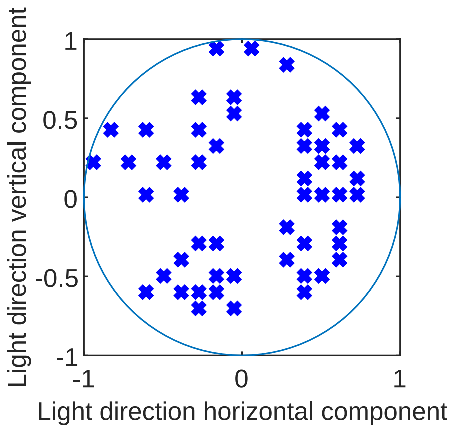

(a) Standard H-RTI method.

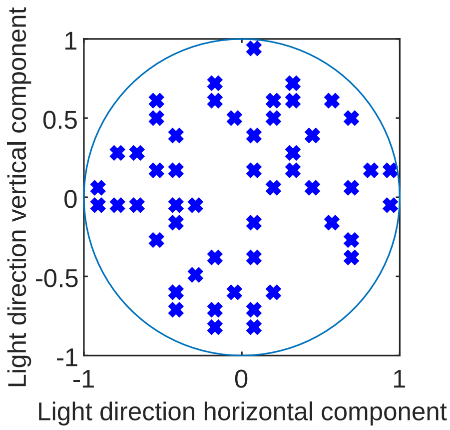

(b) Proposed method.

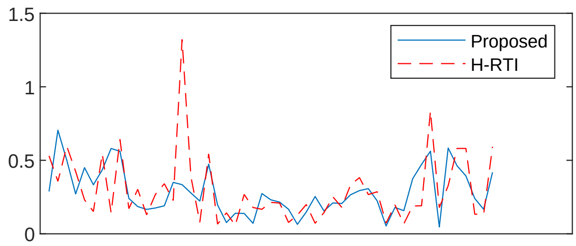

(c) Error in light directions.

Figure 2.8: The different light directions computed from the setup shown in Figure 2.9a, where the object was imaged in a lighting dome of known lighting directions. Here (a) shows the standard H-RTI method where light directions are more heavily biased to to the upper right quadrant due to the bias of the reflective sphere in H-RTI and (a) shows the proposed method where light directions are more uniformly spread using automatic light direction detection outlined in section 2.2.4. The errors for the H-RTI and proposed method light directions are shown in (c).

select the threshold value which yields the highest standard deviation in lighting directions. We do this because a high standard deviation means the estimated light directions are not clustered around the border of the image, and are more evenly distributed, as per the true directions of the light source. This relationship is shown in Figure 2.7, where it can be seen that the standard deviation increases towards 20% upper intensity, then decreases after this optimum percentage.

We then take the coordinates of the resulting optimum centroid and normalise with respect to the centre of the image to obtain a lighting direction. This estimation also does not suffer the bias present when using the reference sphere in standard H-RTI. The result of this process is shown in Figure 2.8, which compares the spread of light directions calculated by the standard H-RTI method with those calculated by our proposed method. It can be seen that the lighting directions generated from the two methods differ greatly, with the reference sphere method suffering from the position bias mentioned in section 1.3.7 causing the plot of lighting directions to be less evenly distributed, despite the fact that the light source was in fact moved in even coverage around the object. These light directions were computed from the setup shown in Figure 2.9a, where the object was imaged in a lighting dome of known lighting directions. The mean difference between the H-RTI method and the true light direction (shown as the dashed line in Figure 2.8c) was found to be 0.2959, and the mean difference between the proposed method and the true light direction (shown as the solid line in Figure 2.8c) was found to be 0.2841 meaning the proposed method is more accurate. The errors in light direction for the proposed method and for the H-RTI method are not markedly different, however there are a few sharp peaks observed in the H-RTI error. These sharp peaks are thought to be a result of the reference sphere being under the shadow of the object being imaged, as is often the case for select images in H-RTI, unbeknownst to the user. Despite the errors being similar, the proposed method is more accurate, automatic and does not require the use of physical calibration equipment. Using these automatically detected light direction vectors, it is also possible to compute new surface normal data for comparison with the standard H-RTI method.

2.3 Experimental Results

We have now fitted a function to the light which allows us to compensate for non-uniform intensity and to extract the light direction automatically. In order to evaluate the light directions estimated and the surface normals generated by the proposed method we image an object of known geometry under known lighting conditions. A 3D printed pyramid with a 30 degree slope was produced and imaged. Fig. 2.9a shows the 3D printed pyramid and the RTI reference sphere used to produce the standard H-RTI results for comparison. Fig. 2.9c shows the surface normals of the pyramid faces calculated using the standard H-RTI method, while Fig. 2.9d shows the same for the proposed method. Polar histograms of the elevation angle measured on all four visible faces of the pyramid (ground truth of 30 degrees) for the standard H-RTI method and the proposed method are shown respectively in Fig. 2.9e and 2.9f. It is clear from inspection that the proposed RTI method produces results much closer to the true elevation angle (of 30 degrees) of the pyramid faces, yielding a mean of 25.19 degrees with a standard deviation of 6.20 degrees, whereas the standard H-RTI method yields a mean of 51.1 degrees with a standard deviation of 20.21 degrees. There are a few peaks present in Fig. 2.9e which are caused by lighting direction errors from the reference sphere shown in Fig. 2.9a, which suffers position bias from not being placed at the centre of the image, as well as the non-uniform intensity not being compensated for. These errors then contribute to the polynomial defined in (1.7) being poorly fitted and causes the resulting surface normals to be inaccurate.

Figure 2.10 compares the standard H-RTI method with the proposed method on a flat, Lambertian surface. Here it can be seen in Figure 2.10b that the standard H-RTI method results in the ring like error effect appearing at the edges due to the periphery of the image receiving disproportionately more light. It can be seen from Figure 2.10a that this error has been corrected almost entirely by using the novel method proposed in this chapter. Figure 2.10a shows this quantitatively, where it can be seen that as we move from the centre of the image out to the right (along the x axis of this plot) that the z component of the surface normal drops off from 1 (surface normal facing the camera) to zero (surface normal perpendicular to the camera) using the standard H-RTI method, but is significantly improved using the proposed method where it only drops down to around 0.8. The true value should be close to 1 across the whole range. Despite this marked

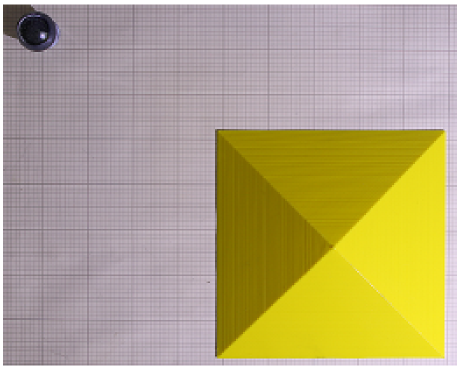

(a) 3D printed pyramid and RTI reference sphere.

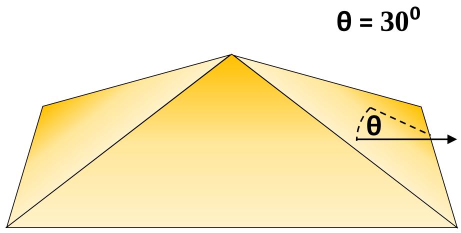

(b) 3D printed pyramid with 30 degree slope.

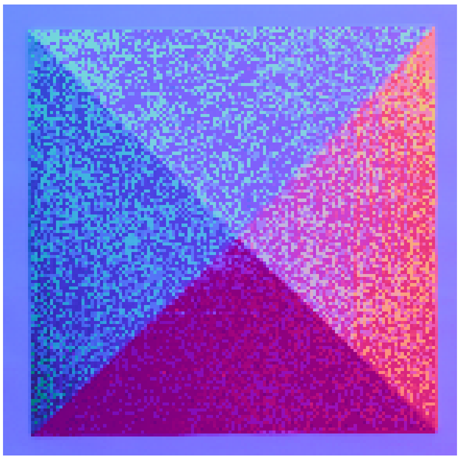

(c) Standard H-RTI surface normal image.

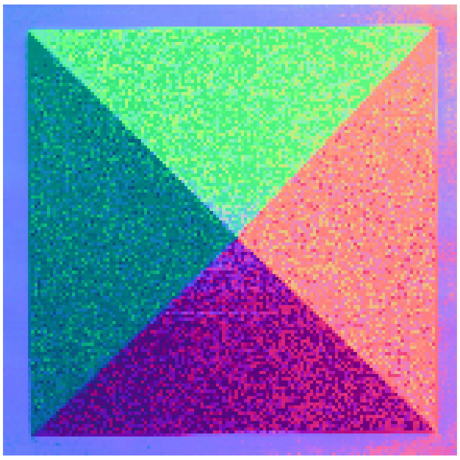

(d) Proposed method surface normal image.

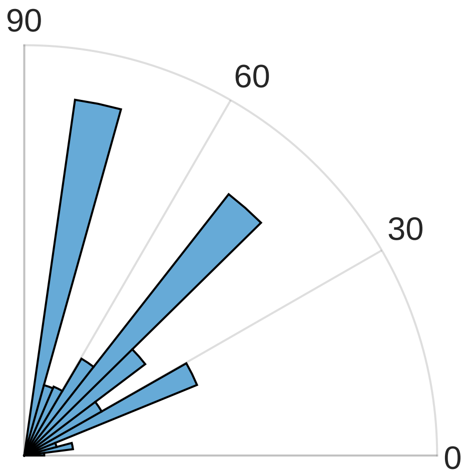

(e) Standard H-RTI elevation.

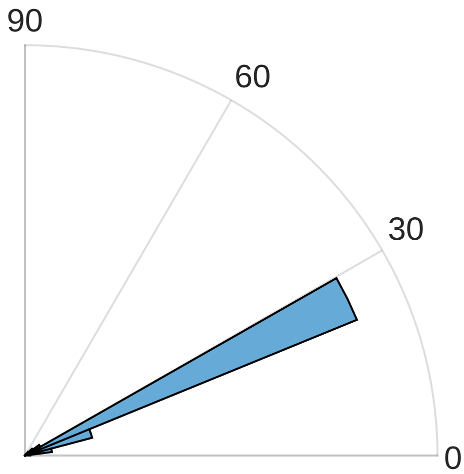

(f) Proposed method elevation.

Figure 2.9: A 3D printed pyramid with a 30 degree slope was produced and imaged to evaluate the proposed method on an object of known geometry. (a) shows the 3D printed pyramid and the RTI reference sphere for producing the standard H-RTI method RTI results (note this image is cropped, the centre of the image is the apex of the pyramid). (c) shows the surface normals of the pyramid faces calculated using the standard H-RTI method, while (d) shows the same for the proposed method. (e) shows the polar histogram of the elevation angle measured on all four visible faces of the pyramid (ground truth of 30 degrees) for the standard H-RTI method and (f) shows the same for the proposed method.

improvement in surface normal estimation, there is still a drop off in the corrected line (shown in solid blue in Figure 2.10a) as the distance to the centre of the image increases. This drop off is due to the marginal brightening factor, F (defined in (2.2) and used in (2.3)), which is given by the interquartile range (IQR) of the mean-corrected image, I_c. The interquartile range serves as an effective marginal brightening factor for improving the accuracy of surface normals for various surfaces. However, we took into account the potential of overcompensation for non-uniform lighting and found that the IQR served as the an optimal marginal brightening factor for the range of surfaces in this chapter.

Figure 2.11a shows a cylindrical chimney of 2.2m diameter for which surface normals were calculated using the standard H-RTI method, shown in Figure 2.11b, and our proposed method, shown in Figure 2.11c. Since the chimney is cylindrical, and constructed from vertical “planks” of concrete, we expect the pixels vertically down the centre of each plank to have the same surface normals, and we can calculate the expected surface normal for each plank. The plots in Figure 2.12 summarise the results from this exercise, with the left column of plots showing results for the x, y and z components of the surface normals respectively from the standard H-RTI process, and the right column showing the same for the proposed method. In each plot, the extent of each box marks the 25th to 75th percentiles of the values from the vertical line of pixels from one plank; the line within the box marks the median value. The dashed lines extending vertically from each box mark the full extent of the values. The single, smooth, solid line in each plot marks the calculated truth. These plots show that the surface normals calculated using the proposed method are significantly more accurate than those from the standard H-RTI method, with smaller spreads of values that are closer to the ground truth. This is especially obvious for the y and z components. In Figure 2.12d the measured y component of the corrected normals is biased to the negative axis likely due to the camera orientation not being exactly perpendicular to the cylinder surface.

Figure 2.13 shows how the proposed corrections from section 2.2 additionally benefit the virtual relighting obtained from RTI. Figure 2.13a shows a flat surface under RTI virtual relighting in which the standard H-RTI method has yielded a surface which appears, erroneously, to bulge due to non-uniform lighting. Figure 2.13b shows the same object, relit from the same virtual lighting direction, but processed using the proposed method. The surface appears much flatter, and is, therefore, much more uniformly lit, which increases the legibility of the inscriptions.

The proposed method was also retrofitted to noisy and imperfect pre-existing multi-light imaging collections in order to test its robustness. The results of this retrofitting are shown in Figure 2.14. The retrofitting of the proposed method to the gravestone shown previously in Figure 2.3 is shown in Figure 2.14e and the standard H-RTI method results are also shown in Figure 2.14c. Here it is shown that the traditional RTI method with the reference sphere generated such poor surface normal data of this generally flat gravestone facing the camera (z direction) that large portions of this surface appear green (y direction i.e. upwards). Despite the grave surface in Figure 2.14a consisting of different textures (stone and various mosses) the surface normals image should appear almost uniform in colour (blue/purple) because the gravestone is flat and facing directly at the camera (and so are the various mosses by and large). These inaccuracies apparent in surface normal data caused by non-uniform illumination are visible from the variation in colour of the surface normal image in Figure 2.14c. Retrofitting was also carried out on a pre-existing multi-light imaging collection of a (also mostly flat) wall memorial shown in 2.14b, 2.14d and 2.14f. It is shown in Figure 2.14f that the proposed method surface normals appear more uniform and camera-facing for the same multi-light imaging collection using the lighting uniformity corrections and automated light direction detection. It is clear here that the surface normals represent a more realistic, flat and uniform surface. These multi-light imaging collections are typical of H-RTI performed on medium to large objects, where for the most-part the lighting has been uniform but occasionally there over-lit regions and completely under-lit images. Despite this, it was found that the method is robust and improves the accuracy of the surface normal data.

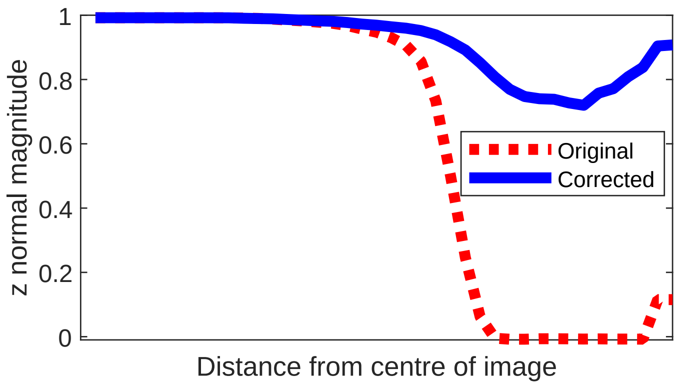

(a) z direction surface normal magnitude from centre outwards to the right with data (b) and (c) represented by the red dotted line and the blue solid line respectively.

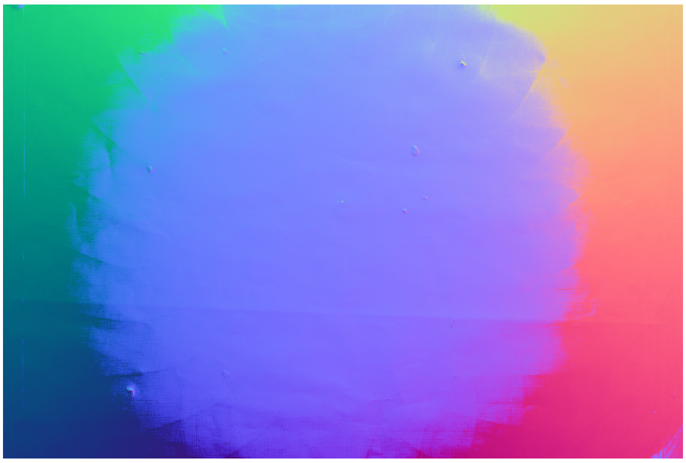

(b) Standard H-RTI method surface normals of flat surface.

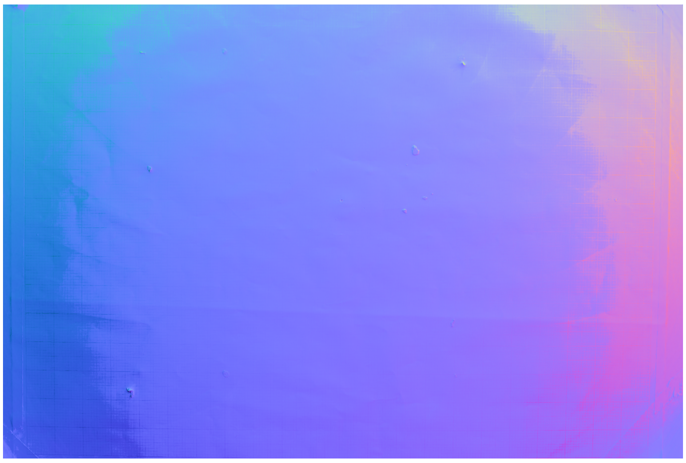

(c) Proposed method surface normals of flat surface.

Figure 2.10: Different surface normal data generated from H-RTI and the proposed method. (a) The z surface normal magnitude of the flat surface measured from the centre of image (camera position) outwards to periphery of image. Since the surface is flat and camera-facing the z normal should measure as a straight line of $z = 1$ (b) Surface normals generated using traditional RTI. (c) Surface normals generated using non-uniform illumination corrected data and automatic light direction detection. Note the colour range representing the surface normals in (b) and (c) are the same.

(a) Cylindrical chimney of 2.2m diameter.

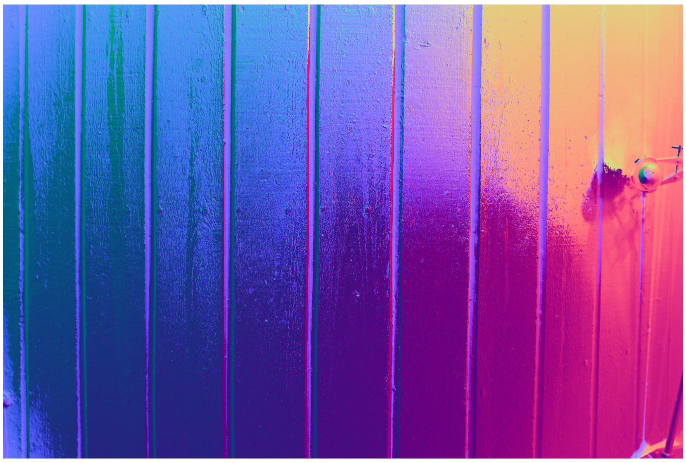

(b) Standard H-RTI method surface normals.

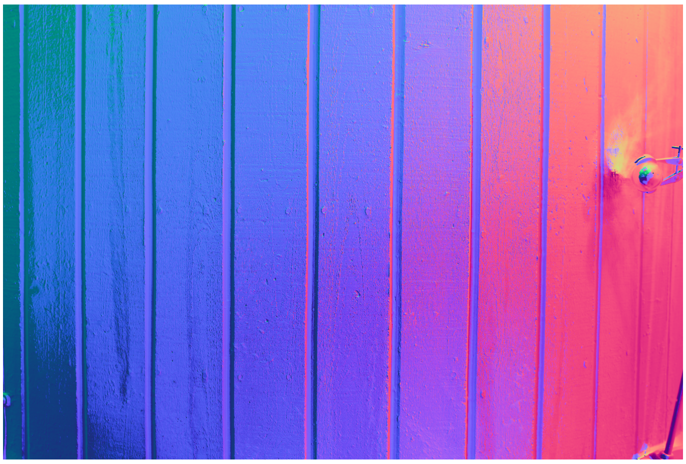

(c) Proposed method surface normals.

Figure 2.11: A cylindrical chimney of 2.2m diameter imaged to demonstrate the proposed method on a curved surface. (a) shows the chimney within its background context (this is not one of the RTI images). (b) shows the surface normals of the semi-cylindrical surface calculated using the standard H-RTI method, while (c) shows the same for the proposed method.

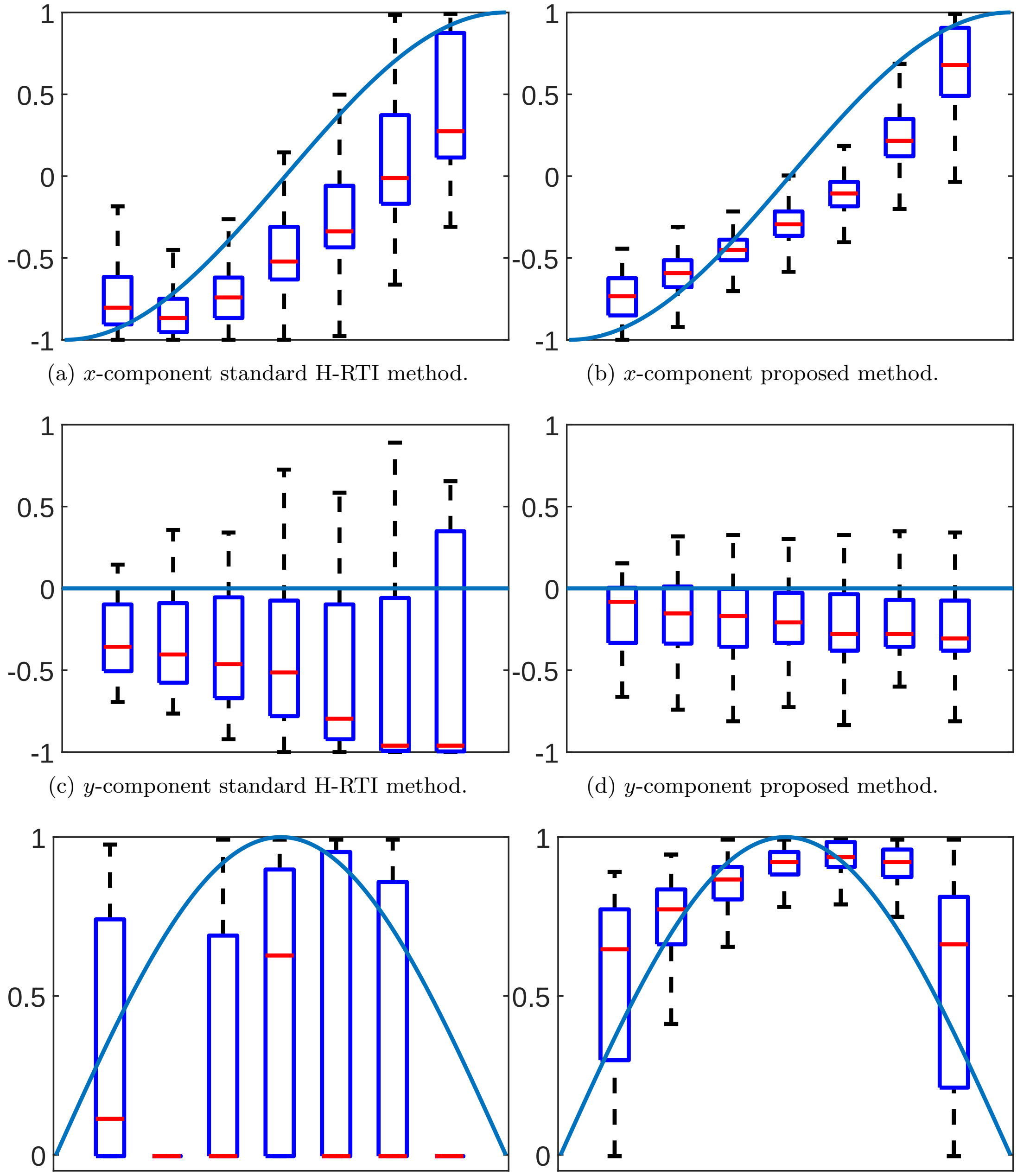

(a) x-component standard H-RTI method. (b) x-component proposed method.

(c) y-component standard H-RTI method. (d) y-component proposed method.

(e) z-component standard H-RTI method. (f) z-component proposed method.

Figure 2.12: For each of the seven central "planks" of concrete shown in Figs. 2.11b and 2.11c, the surface normals for a column of pixels have been used to produce the boxplots shown here. The three rows of plots show the x, y and z components of the surface normals respectively, where the smooth, continuous line in each plot marks the ground truth. The left column shows results using the standard H-RTI process, while those in the right column are from the proposed method. Each box represent the interquartile range and the centre line inside the box represents the median value; the dashed lines at the top and bottom of each box mark the full range of values.

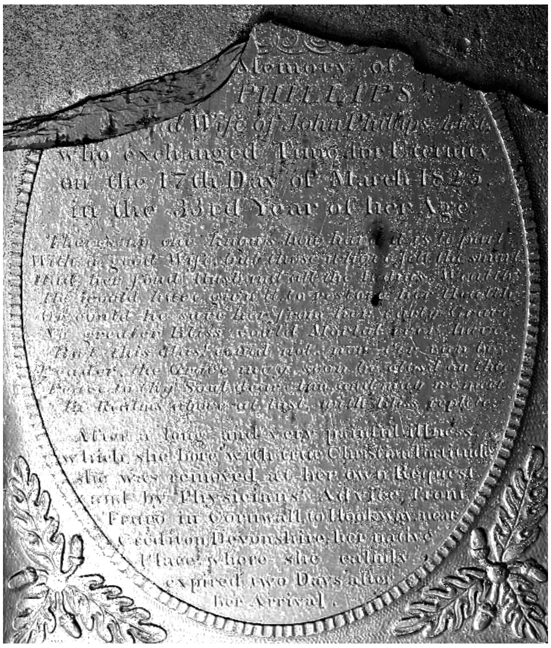

(a) Standard H-RTI specular enhancement.

(b) Proposed method specular enhancement lit from from same direction as (a).

Figure 2.13: The proposed technique not only results in more accurate surface normal data, but also results in improved readability and uniform lighting in virtual relighting which is visible here for a flat surface which falsely appeared to be curved due to non-uniform lighting. Note these images are lit from the same lighting direction. (a) Specular enhancement for uncorrected multi-light imaging collection showing non-uniform lighting. (b) Virtual relighting specular enhancement for corrected multi-light imaging collection showing uniform lighting using the proposed method. This also increases readability.

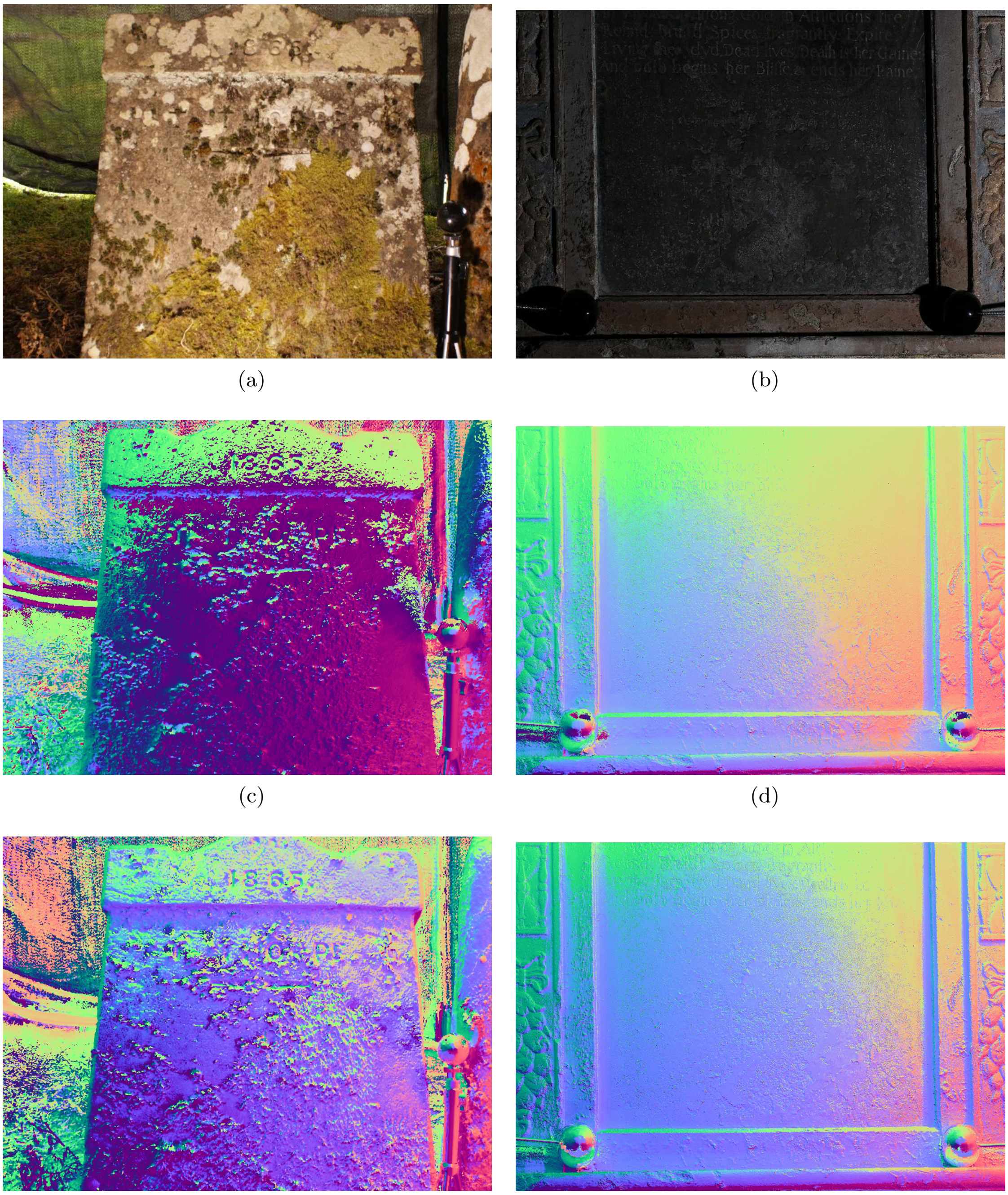

(a) (b) (c) (d) (e) (f)

Figure 2.14: Here we have retrofitted the proposed method to existing multi-light imaging collections. (a) shows a colour image of the gravestone featuring in Fig. 2.3. In (c) we see the surface normals measured for the same gravestone using the standard H-RTI method and (e) shows the surface normals measured using the proposed method. (b) shows a colour image of a flat wall memorial. (d) shows the surface normals calculated for the same wall memorial using the standard H-RTI method and (f) shows the surface normals calculated using the proposed method.

2.4 Conclusions

In this chapter we present a novel, fully automated technique for correcting common lighting errors in RTI and markedly improve the accuracy of surface normal estimation, leading to an increase in legibility of low relief surface variations. Like other authors we show that the uniform light assumption is false and propose a novel method to correct for it. However, we estimate the lighting directions automatically, unlike other proposed correction techniques.

The results discussed in section 2.3 show marked improvements in surface normal estimation for H-RTI using the proposed new method which, as is shown in Figure 2.14, can also be retrofitted to existing highlight multi-light imaging collections. RTI for larger objects suffers the most from non-uniformity in lighting, since for small items, such as coins, the lighting can be considered approximately parallel as the deviation in incident light angle across the image plane is much smaller. The proposed method more accurately estimates the light directions (see section 2.2.4) and does not require the addition of reference spheres or 3D printed calibration devices into the scene as other authors do [28] (note the 3D printed pyramid we use is for evaluation purposes). We keep the RTI process simple and inexpensive for non imaging science/photography professionals whilst markedly improving the results for surface normal generation compared with H-RTI when performed on larger objects and objects of known geometry such as in Figure 2.9.

The significant improvement in uniform lighting evident in Figure 2.13 during virtual relighting shows that the method is also relevant to conservationists who are more interested in readability of inscriptions than quantitative RTI.

These more quantitatively accurate surface normals mean that RTI could become more ubiquitous in cases where laser scanning would usually be used. This technique is not invulnerable to very messy multi-light imaging collections, where the light source has largely missed the centre of the object for a significant proportion of the images, but is more robust than traditional RTI.

3 Remote Extraction of Latent Fingerprints (RELF)

The following item has been published using material from this chapter:

McGuigan, M., and Christmas, J. (2020). Remote Extraction of Latent Fingerprints (RELF). In 2020 International Joint Conference on Neural Networks (IJCNN). 2020 International Joint Conference on Neural Networks (IJCNN). IEEE.
https://doi.org/10.1109/ijcnn48605.2020.9207376

Latent fingerprints are the kind left on objects after direct contact with a person's finger, often unwittingly at crime scenes. Most current techniques for extracting these types of fingerprint are invasive and involve contaminating the fingerprint with chemicals which often renders the fingerprint unusable for further forensic testing. We propose a multi-light imaging based method for extracting latent fingerprints from surfaces without the addition of contaminants or chemicals to the evidence. We show our technique works on notoriously difficult to image surfaces, using off-the-shelf cameras. In particular, we extract images of latent fingerprints from surfaces which are transparent, curved and specular such as glass light-bulbs and jars, which are challenging forensically due to their curvature and shininess. Our method produces results comparable to more invasive methods and leaves the fingerprint sample unaffected for further forensic analysis.

3.1 Introduction

Latent fingerprints are nearly invisible, formed by a dielectric residue left behind from the fingerprint ridges containing water with various salts and organic compounds [66]. Extracting latent prints is complicated since they are often found on complex curved surfaces. Existing methods are invasive and vulnerable to improper collection techniques which may cause a loss of information [62]. These invasive methods often physically enhance latent prints by adding a material to the print such as 'dusting' involves adding a powder that will become fixed to the residue left behind, and hence increase visibility for any further imaging [9]. This type of chemical processing may degrade or contaminate the evidence, preventing additional forensic testing [54]. Our method is simple, fast and requires only an off-the-shelf camera. Fingerprints are comprised of ridges which may terminate or form bifurcations as well as a variety of other distinctive features known as minutiae which usually appear in the fingerprint in unique combinations. Latent fingerprint minutiae are more difficult to match than those of patent fingerprints, and are more susceptible to scrutiny in courtroom arguments [97]. This is due to the non-ideal surfaces (often curved

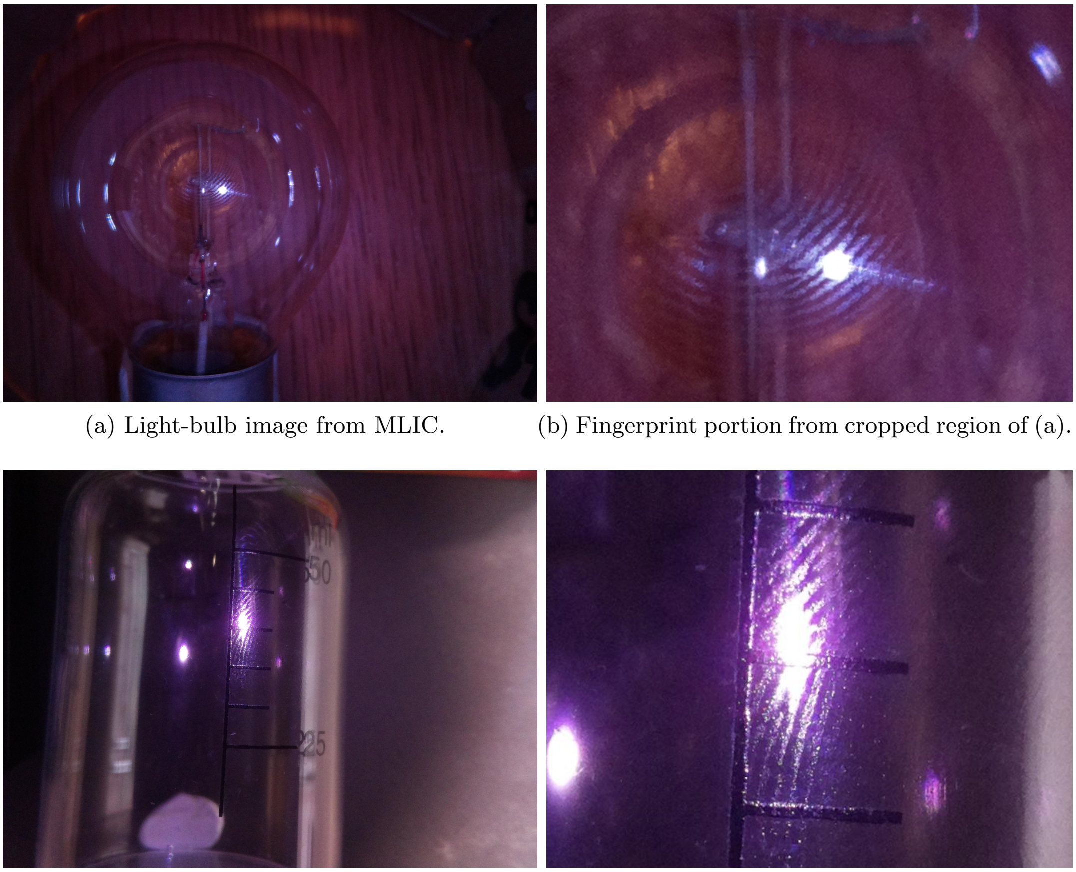

(a) Light-bulb image from MLIC. (b) Fingerprint portion from cropped region of (a).

(c) Beaker image from MLIC. (d) Fingerprint portion from cropped region of (c).

Figure 3.1: Here we see two MLICs of objects each containing a fingerprint. (a) shows an example MLIC image of a glass light-bulb. (b) shows cropped region of (a) containing a fingerprint. (c) shows an example MLIC image of a glass beaker. (d) shows cropped region of (c) containing a fingerprint. This observation provided the motivation behind the proposed MLIC method for contactless fingerprint extraction.

and specular) where latent prints are often found. Specular surfaces complicate imaging forensically because their reflectance is highly direction dependent, meaning the lighting direction has to be just right in order to reveal the fingerprint.

3.2 Latent fingerprints and surface curvature

Our proposed multi-light imaging collection (MLIC) method aims to assist in developing a simple and standard non-invasive technique to extract fingerprints in these circumstances so they may become a less vulnerable form of forensic evidence. Given the scale of fingerprint ridges and the fact that the quality of images impact the effectiveness of fingerprint feature point extraction [89], we work with high resolution input images in order to preserve the finer details.

Figures 3.1a and 3.1c show select images from MLICs of a light-bulb and glass beaker respectively, both of which contain a partially visible fingerprint shown in figures 3.1b and 3.1d. This exemplifies how fingerprint imaging on curved specular surfaces is dependent on lighting direction, with Figure 3.1b and Figure 3.1d showing clear fingerprint ridges

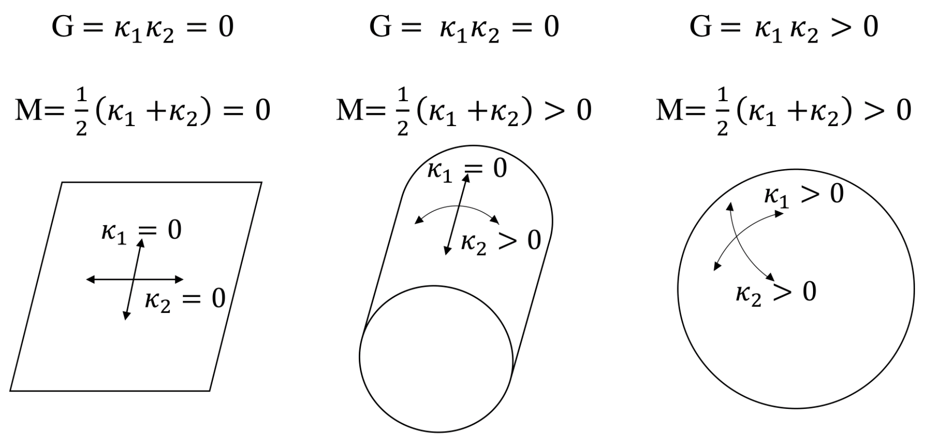

Figure 3.2: An outline of the different surface curvatures that the RELF algorithm is equipped to process.

but only for a portion of the fingerprint. This observation provided the motivation behind the proposed MLIC method for contactless fingerprint extraction.

The local shape of a point on a surface is determined by the two principal curvatures (eigenvalues of the shape operator at this point), κ_1 and κ_2 [43]. One principal curvature defines the rate of maximum bending and its corresponding tangent direction on the surface, while the other defines the rate and corresponding tangent direction of minimum bending. We will not focus too much on the mathematics of these principal curvatures, but it is important to acknowledge their significance and effects on imaging different surfaces. Two useful quantities we consider are Gaussian and mean curvatures, G and M. As one would expect, the curvature (Gaussian and mean) of a planar surface is zero. However, the mean curvature of a cylindrical surface is greater than zero, while the Gaussian curvature is still zero. This is because the Gaussian curvature of a surface is multiplicative (as shown in (3.1) and mean curvature is additive (as shown in equation (3.2) and visualised in Figure 3.2).

$$G = \kappa_1\kappa_2 \tag{3.1}$$

$$M = \frac{1}{2}(\kappa_1 + \kappa_2) \tag{3.2}$$

This means that if any of the principal curvatures, κ_1 and κ_2, are equal to zero then so will the overall Gaussian curvature G be. For this reason the mean curvature is more significant for the purposes of extracting fingerprints. We examine the effects of different principal curvatures and the proposed method's performance, and note how imaging becomes more difficult as mean curvature increases. In section 3.9 we show RELF is able to extract prints from specular planar surfaces including a mobile phone screen, with both principal curvatures $\kappa_1 = \kappa_2 = 0$, and hence a mean curvature of zero. Imaging a flat specular surface where both principal curvatures are zero is comparatively easier than when one or both are non-zero. We also extract fingerprints from specular cylindrical surfaces such as the glass beaker shown in Fig. 3.1c with $\kappa_1 = 0$ and $\kappa_2 > 0$, which results in positive mean curvature. Imaging cylindrical surfaces where one principal curvature is non-zero proves more difficult than a flat surface, but is possible to extract fingerprints using the RELF method as shown in Fig .3.24c. Our method also proves robust enough to work on specular spherical surfaces such as the spherical bulb shown in Fig. 3.1a with both principal curvatures κ_1 and κ_2 being positive. Despite the surface being much more difficult to image since both principal curvatures are non-zero, the RELF method is still able to extract fingerprints as shown in Fig 3.25c and Fig. 3.27c. A lower mean curvature of a surface is indicative of the ease at which we may extract fingerprints. The surfaces in these examples are also specular, which poses different issues as outlined in section 1.1.

3.2.1 Concepts behind proposed method

It has been noted by forensic investigators for decades that by varying the angle of a torch incident on a surface potentially containing latent fingerprints, it is possible to locate partial or full fingerprints [79]. Our method utilises this basic principle: we illuminate the object suspected to contain a latent fingerprint using multi-light imaging, a technique in which the object is held stationary and a light source illuminates the item from a different direction for each image. Reflectance Transformation Imaging (RTI) utilises multi-light imaging (using a lighting dome to avoid the process of manually moving a flash around) to compute surface normals and obtain topographical information about the object being imaged [56]. RTI is chiefly used in cultural heritage imaging since it is inexpensive and produces high resolution surface topography using off-the-shelf cameras. We borrow our imaging approach from RTI, but the similarities end here. We apply machine learning to reveal the hidden latent fingerprints found on objects.

3.3 Methods

The clarity of fingerprint ridges (despite only revealing a portion of the fingerprint in any given image) visible through multi-light imaging as shown in Figure 3.1 provided the motivation behind the proposed RELF method for contactless fingerprint extraction. The steps for our method are outlined in Fig. 3.3. We use multi-light imaging with an off-the-shelf digital camera to gather images as outlined in 3.3.1.

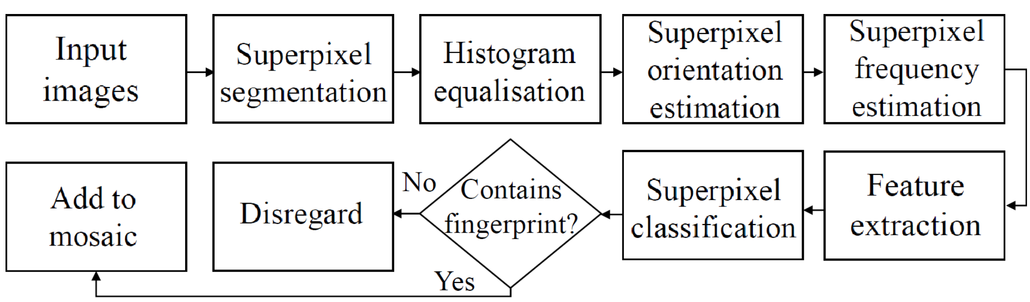

Figure 3.3: A flowchart of the RELF algorithm, which extracts features from superpixels for classification then uses these classifications to build a fingerprint image.

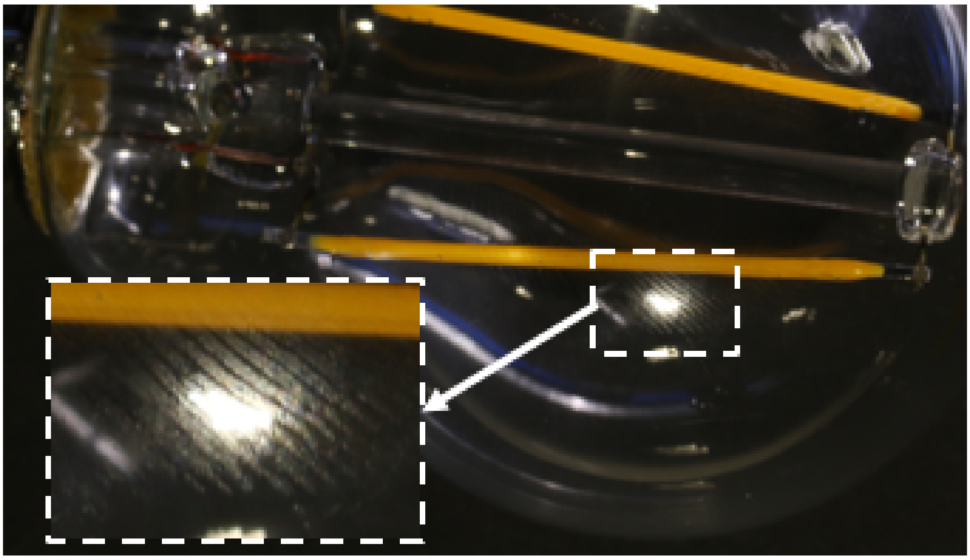

Figure 3.4: A spherical light-bulb exhibiting a specular reflection which is saturated but reveals a neighbouring portions of visible fingerprint.

3.3.1 Data acquisition using multi-light imaging

Latent fingerprints viewed under illumination on curved surfaces are only partially visible from any one lighting angle. They also vary in brightness relative to their proximity to the specular reflection on the curved surface. This means we only see small regions of the fingerprint at best in each image. This can be seen in Fig. 3.4 where the specular reflection of the light source is saturated, but the surrounding region contains a visible portion of the fingerprint. Using the multi-light image collection technique we illuminate the curved glass object to build up, piece by piece, the overall fingerprint image by combining each portion of the fingerprint. For each image stack we obtain around 90 images, with the location of the specular reflection being different on the surface because the light changes direction on the LED dome. At the apex of the multi-light imaging dome an off-the-shelf DSLR camera captures an image for each unique lighting direction.

3.3.2 Superpixel segmentation of fingerprint images

Having obtained the image data, we break down each image into sets of segments called superpixels [85] that collectively cover the entire image as shown in Figure 3.5a, where superpixels containing fingerprint have more ‘frilly’ and meandering edges than non-fingerprint superpixels which have much straighter edges, helping us discriminate between the two. Each individual superpixel is formed through grouping pixels with similar features such as colour, texture and brightness [85]. Superpixels can be generated by two main categories of algorithms: graph based and gradient ascent [2]. We opt to use a gradient ascent based method known as simple linear iterative clustering (SLIC), which efficiently generates superpixels using k-means clustering [1]. Often specular reflection pixels are grouped together by the SLIC superpixels algorithm due to their similar intensity, we use this to determine whether or not the superpixel requires further processing in the RELF framework. In these instances the entire superpixel is *whited* out, and yields little to no information. SLIC is straightforward and memory efficient, allows control over the number

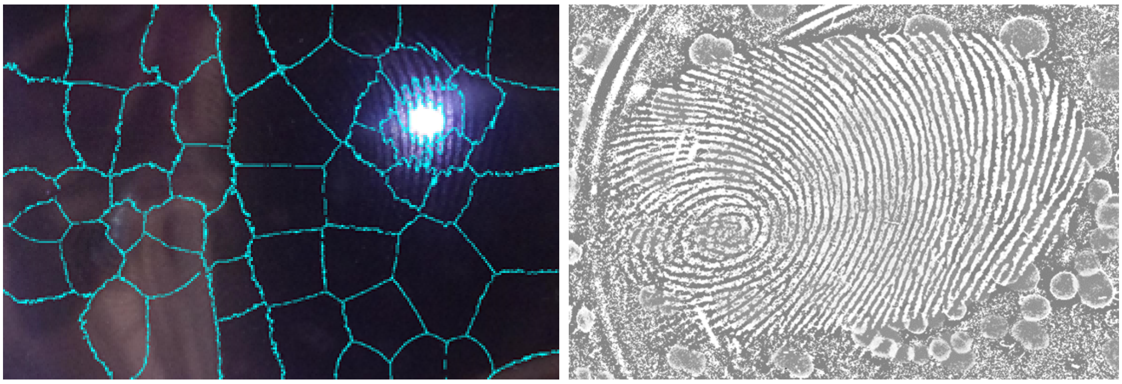

(a) MLIC image segmented using superpixels. (b) Fingerprint extracted from same MLIC as (a) using RELF.

Figure 3.5: We use superpixel segmentation to extract fingerprints from MLICs. (a) shows an MLIC image after superpixel segmentation, where superpixels containing fingerprint have more 'frilly' and meandering edges than non-fingerprint superpixels which have much straighter edges, helping us discriminate between the two. (b) shows the resulting fingerprint extracted from same MLIC as (a) using RELF.

of superpixels and adheres well to boundaries [2]. By varying the number of superpixels used, it was found that 200 superpixels segmented the fingerprint region best. We set the SLIC compactness to 10 because this allowed the superpixel boundaries to adhere to the fingerprint edges and better segment the fingerprint.

3.4 Feature extraction

We construct one feature vector per superpixel, which is comprised of numeric features of an object in our case a small region of the image, a superpixel. We obtain fourteen numerical features from the superpixel to build a one dimensional feature vector. These fourteen features were empirically chosen after observing the difference between superpixels which contained fingerprint and those which did not. For example, superpixels containing fingerprint were observed to have a meandering perimeter where the superpixel boundary adheres to the fingerprint ridges. This observation led to the perimeter over area ratio (feature 5) and convex hull over perimeter ratio (feature 6) being chosen as one of the fourteen features. We may use this 14x1 feature vector to represent the entire superpixel, meaning we only use 14 elements to learn from instead of the $40,000$ elements (pixels) a typical superpixel may consist of. We use these feature vectors to train a classifier so that it may learn information from these metrics and which combination of these metrics represent a fingerprint superpixel and which combinations do not, as summarised in Fig. 3.6

On a curved and specular surface the intensity of the fingerprint varies drastically with distance to the specular highlight. We use histogram equalisation across each superpixel before feature extraction to even out these disparities. This method is particularly effective for areas with lower local contrast (and further away from the specular reflection) to gain a higher contrast. This increases the clarity of any potential fingerprint ridges and allows

Feature Number	Superpixel feature
1	Number of potential fingerprint ridges
2	Cross correlation with filter
3	Ratio of light to dark pixels
4	Aspect ratio of superpixel
5	Perimeter over area ratio
6	Convex hull over perimeter ratio
7	Variance in intensity
8	Median value of intensity
9	Mode value of intensity
10	Entropy of the superpixel
11	Contrast (from GLCM)
12	Correlation (from GLCM)
13	Energy (from GLCM)
14	Homogeneity (from GLCM)

Figure 3.6: Example of feature vector extracted from superpixel.

us to determine whether any useful portions of the fingerprint are present. Examples of superpixels containing fingerprint data can be seen in Fig. 3.7. The unprocessed superpixels are shown in (a) - (g) and the corresponding superpixels having undergone histogram equalisation are shown in (b) - (h), where the ridges of the fingerprint portions are much clearer. Now we have increased the clarity of potential fingerprint containing superpixels, we will look at methods for frequency estimation.

3.4.1 Orientation and frequency estimation

We obtain our first two numerical features, cross-correlation of the superpixel with a filter generated using the underlying predominant spatial frequency of the superpixel and the number of potential fingerprint ridges by performing a two-dimensional Fast Fourier Transform (FFT), enabling us to estimate the dominant spatial frequency in the superpixel. We perform Fourier analysis separately on each superpixel, extracting these two features independently for each one (fingerprint ridge frequency is not assumed as constant due to curved surface). We are then able to measure the orientation of this dominant frequency relative to the horizontal, and calculate the cross-correlation of the superpixel with a filter generated using the underlying predominant spatial frequency of the superpixel. This cross-correlation is our first numerical $feature$ to be input into our machine learning algorithm as outlined in 3.4. If a given superpixel indeed contains fingerprint ridges, it will exhibit a high cross correlation with a sinusoid filter of the same frequency as shown in Fig. 3.8.

We take into consideration that the cross-correlation of a sinusoidal filter with a fingerprint portion may encounter issues due to the fact that the curvature of fingerprint ridges increase towards the centre of the fingerprint [81]. In these central fingerprint sections with high ridge curvature, the assumption of a dominant ridge direction and parallel ridges is not valid since the curvature is too great. This means, in central fingerprint regions, the correlation could indicate a low similarity with the sinusoidal filter. However, the effects

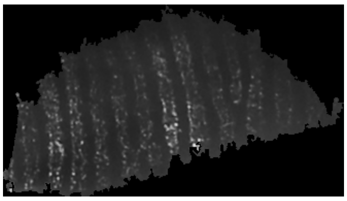

(a) Before HE.

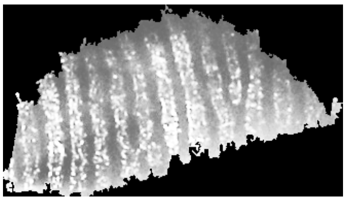

(b) After HE.

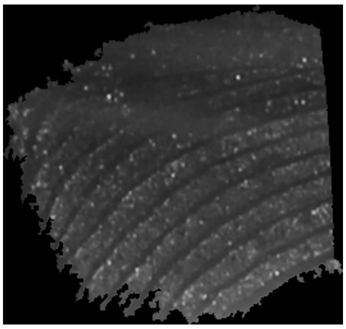

(c) Before HE.

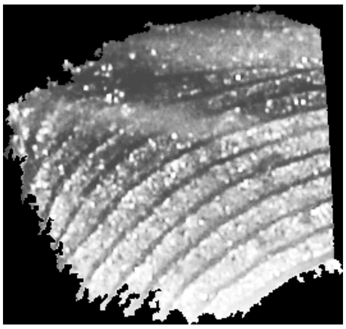

(d) After HE.

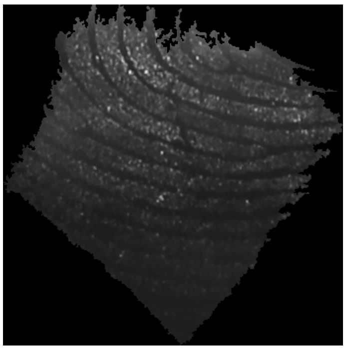

(e) Before HE.

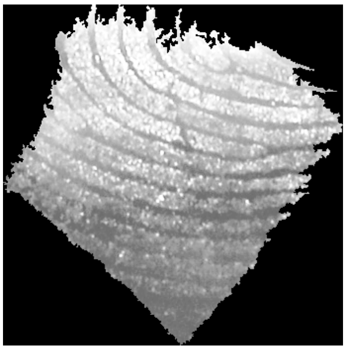

(f) After HE.

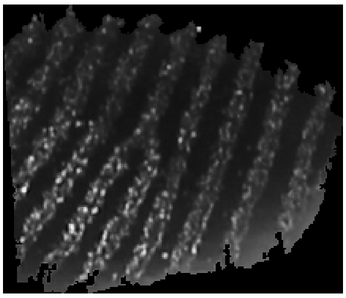

(g) Before HE.

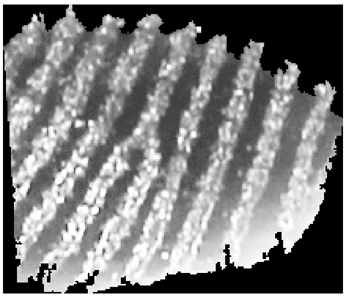

(h) After HE.

Figure 3.7: Various input superpixels before and after histogram equalisation (HE) to enhance contrast. The left column shows the input superpixels containing fingerprint. The right column shows the same superpixels after undergoing histogram equalisation.

of this issue were found to be minimal if the number superpixels used is sufficiently high. This is because if we increase the number of superpixels (and hence decrease their size) the central regions appear to be approximately less curved.

Indeed, most of the superpixels containing fingerprint ridges (see Fig. 3.8a) were found to be sufficiently parallel that they closely match the sinusoidal filter (see Fig. 3.8c). These similarities are also visible in the in the corresponding frequency spectra of the fingerprint (see Fig. 3.8b) and sinusoid (see Fig. 3.8d). As well as the spatial frequency of a fingerprint varying naturally, the spatial frequency of latent prints present an additional issue as they may vary due to the curvature of the surface they are present on (since the surface's distance from the camera varies). Thus, we adaptively analyse local regions of the fingerprint using superpixel segmentation, estimating the local frequency separately in each superpixel. We estimate the number of fingerprint ridges present by aligning the ridges with the vertical using the orientation information computed from the Fourier transform, then we compute the mean of all rows in the image and calculate the number of peaks in this mean row.

3.4.2 Gray-level co-occurrence matrix (GLCM)

We compute the gray-level co-occurrence matrix (GLCM) for each superpixel, which is a histogram of co-occurring grayscale values at a given offset across an image [34]. We compute the GLCM for each superpixel to quantitatively analyse their texture, allowing us to extract numeric GLCM features such as contrast, which measures the intensity contrast between a pixel and its neighbour over the superpixel, correlation, which measures how correlated a pixel is to its neighbour over the whole superpixel, energy, which yields the sum of squared elements in the GLCM, and homogeneity, which is a measure of the closeness of elements in the GLCM to the GLCM diagonal (a texture is considered coarse if most entries in the GLCM are situated down the main diagonal).

We will now discuss processing the superpixel to obtain more features and build *feature vector* for input into a classifier.

Number of potential fingerprint ridges present in superpixel

As described in 3.4.1, we estimate the number of fingerprint ridges present in a given superpixel by aligning the ridges so they are vertical using the orientation information computed from the Fourier transform, then we compute the mean of all rows in the image and calculate the number of peaks in this mean row.

Cross correlation of superpixel with filter

As described in 3.4.1, we obtain the cross correlation of the superpixel against a 2D sinusoidal filter.

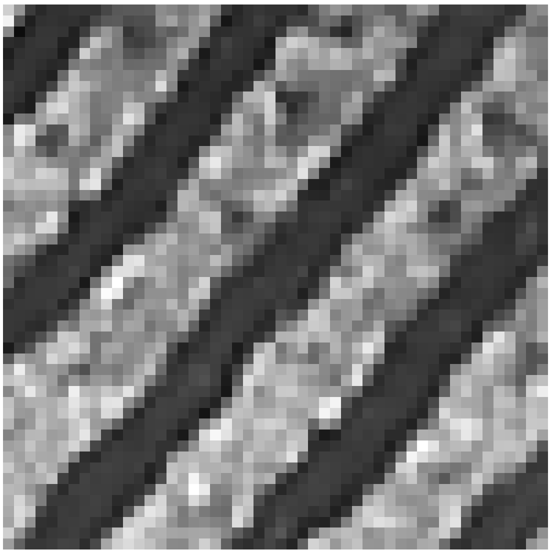

(a) Portion of fingerprint.

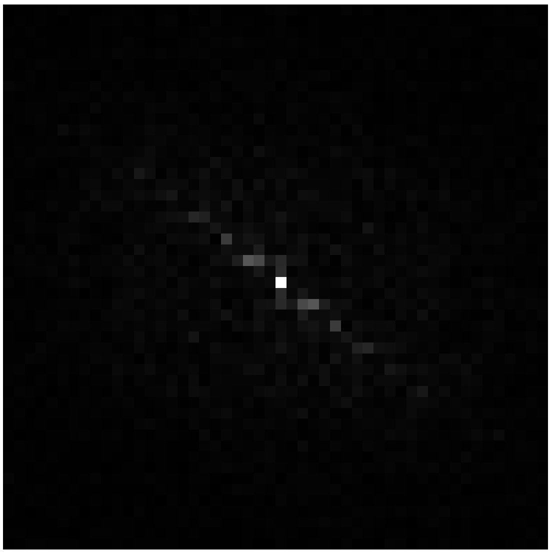

(b) Fingerprint in frequency domain.

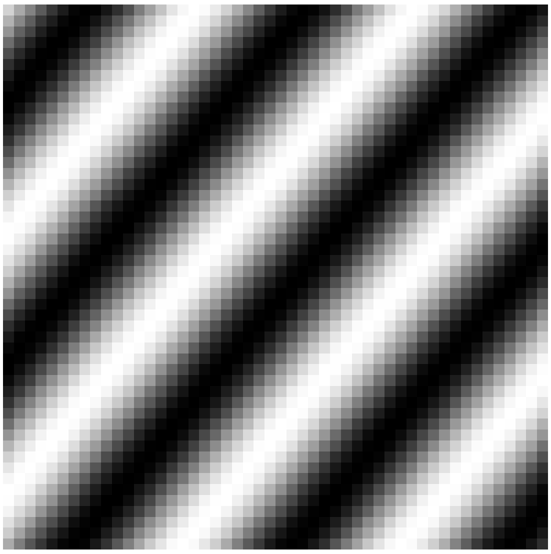

(c) Synthetic 2D sinusoidal pattern.

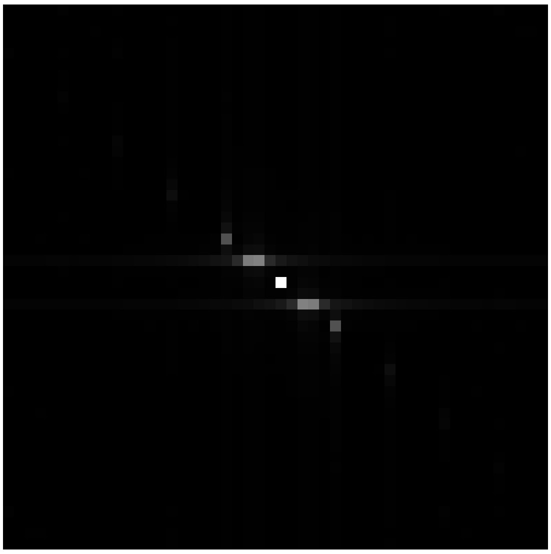

(d) 2D sinusoidal in frequency domain.

Figure 3.8: (a) Sample of exemplar fingerprint portion. (b) The resulting frequency domain image computed from the Fourier transform of the fingerprint portion. (c) A 2D sinusoidal filter. (d) The resulting frequency domain image after a Fourier transform on the sinusoidal filter.

Ratio of non-zero to zero value pixels in superpixel

We compute the ratio of non-zero value to zero value pixels (i.e. the ratio of light to dark pixels). This feature indicates how saturated the superpixel is and hence indicates the likelihood that fingerprint is present. The SLIC superpixels algorithm groups together specular reflection pixels due to their similar (saturated) intensities. In these instances often the entire superpixel is *whited* out, yeilding a ratio of non-zero to zero value pixels of near 1, we can safely assume that the superpixel contains little to no information. Conversely if this ratio is near 0 we may assume that the superpixel is in fact too dark to obtain information from.

Aspect ratio of superpixel dimensions

The aspect ratio of the superpixels dimensions is computed as this can serve as a useful indicator about the contents of the superpixel. This is because the shape of specular reflections on curved surfaces are often elongated and their dimensions are highly dissimilar. We simply calculate the superpixel height and width then take the smallest of these two dimensions and divide it by the largest, meaning that the aspect ratio is rotation invariant.

Ratio of perimeter over area of superpixel

The ratio of superpixel perimeter to area is also a helpful numerical feature since it indicates how the superpixel has adhered to object boundaries in the image, with largely empty superpixels having smaller (more square) perimeters and superpixels containing fingerprint portions have a larger (more meandering) perimeter as shown in Fig. 3.9b.

Ratio of convex hull over perimeter of superpixel

The convex hull of a set of points on a plane is the smallest possible convex polygon which contains all of the points in the set. The convex hull may occasionally be equal to the perimeter of the superpixel when there is less texture in the superpixel. However, the perimeter is usually larger than the convex hull in instances where the superpixel contains fingerprint as is shown in Fig. 3.9b.

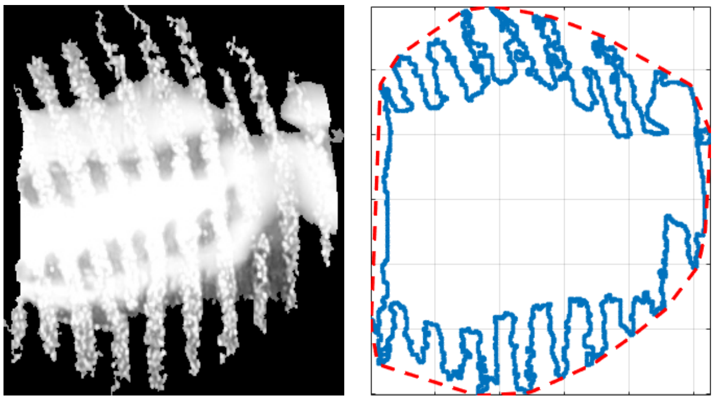

(a) Example of superpixel with meandering perimeter due to fingerprint.

(b) Perimeter and convex hull shown by solid blue and dashed red lines respectively.

Figure 3.9: Fingerprint ridges present in a superpixel result in a meandering superpixel perimeter, which is larger than the superpixel convex hull. (a) Shows an example of a superpixel with fingerprint ridges (b) Shows the perimeter is larger than the convex hull due to the fingerprint ridges.

Variance in intensity across superpixel

We compute the variance to measure how far the set of intensity values in the superpixel deviate from their average value.

Median intensity value of superpixel

We compute the median since outliers do not affect this feature as much as they affect the mean, which is useful when comparing superpixels that may contain a few bright specular pixels but are overall darker.

Mode intensity value of superpixel

We compute the modal value of the superpixel since it is also not as affected by outliers as the mean, which is useful when a small number of bright specular pixels occur in an overall dark superpixel.

Entropy of the superpixel

The entropy value tells us the randomness of intensity the distribution in the superpixel. It also provides us measure of information content, estimating the amount of information present in a superpixel [30].

Contrast (from GLCM)

As described in 3.4.2, we obtain a contrast value from the gray-level co-occurrence matrix (GLCM) which is a statistical method for examining texture.

Correlation (from GLCM)

The GLCM correlation measures how correlated a pixel is to its neighbour over the whole superpixel (see 3.4.2).

Energy (from GLCM)

The energy value of the GLCM yields the sum of squared elements in the GLCM (see 3.4.2).

Homogeneity (from GLCM)

Homogeneity is a measure of the closeness of elements in the gray-level co-occurrence matrix (GLCM) to its diagonal (a texture is considered coarse if most entries in the GLCM are situated down the main diagonal). For more detail see 3.4.2. We can now use this 14x1 feature vector to represent the entire superpixel as is shown in Fig. 3.6.

3.4.3 Processing the feature vectors

Now we have defined our feature vector to represent each superpixel, we extract these features from MLICs where each superpixel has been labelled as fingerprint or non-fingerprint so that we may train a classifier to learn from these features and correctly identify fingerprint features.

3.5 Fingerprint matching algorithm

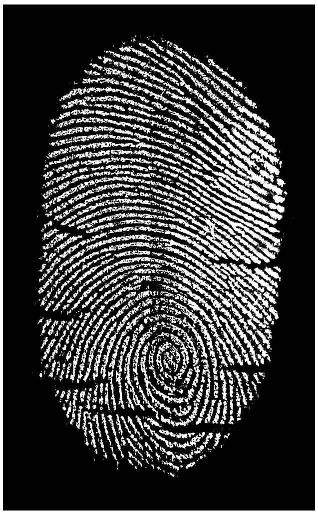

Figure 3.10: The flat reference fingerprint image we extract minutiae from to obtain a match score from minutiae extracted from latent print images.

In order to evaluate the quality of any extracted prints, we use a fingerprint matching system for matching one fingerprint to another. One such system, developed in the United States by National Institute of Standards and Technology (NIST) is the NIST biometric image software (NBIS) [15]. This software is was developed with the Federal Bureau of Investigation (FBI) and the Department of Homeland Security. NBIS includes the minutiae extractor MINDTCT, which extracts the location of each minutiae point in the image, as well as its orientation and type.

NBIS is used to obtain a match score by extracting minutiae from a flat reference fingerprint image (shown in Figure 3.10), and then pair the minutiae from this image to a latent print imaged using our method. The match score is computed with the construction of a list of these minutiae pairs, with each pair being described by the distance between the two minutiae in the pair and the two angles of orientation of both minutiae in the pair relative to the line connecting them. One pair of minutiae from a given fingerprint image may then be compared to the extracted minutiae from another using the NBIS BOZORTH3 algorithm.

NBIS produces an integer value for the match score, where a match score of greater than 40 usually indicates a true match [46]. A match score of 40 is usually only obtainable with patent fingerprints (often made purposefully by inking a finger for example) where the print is clear to see. For latent fingerprints, achieving a score of 40 using NBIS is difficult (but we show in chapter 5 this is possible).

3.6 Generating a fingerprint image

In order to generate a complete fingerprint image from a MLIC, we take an MLIC image as shown in Figure 3.11a then use superpixel segmentation as shown in Figure 3.11b. We then assign each superpixel the value of its predicted fingerprint probability as shown in Figure 3.11c, where superpixels with a higher predicted fingerprint probability appear brighter and lower probability superpixels appear dark. We compute this for each image in the MLIC, then find the highest predicted fingerprint probability on a per-pixel basis and add the pixel from the corresponding image which generated this highest probability and add this the the fingerprint image as shown in Figure 3.11d. The fingerprint images in the following sections and chapters in this thesis are generated using the method shown in Figure 3.11.

(a) MLIC image.

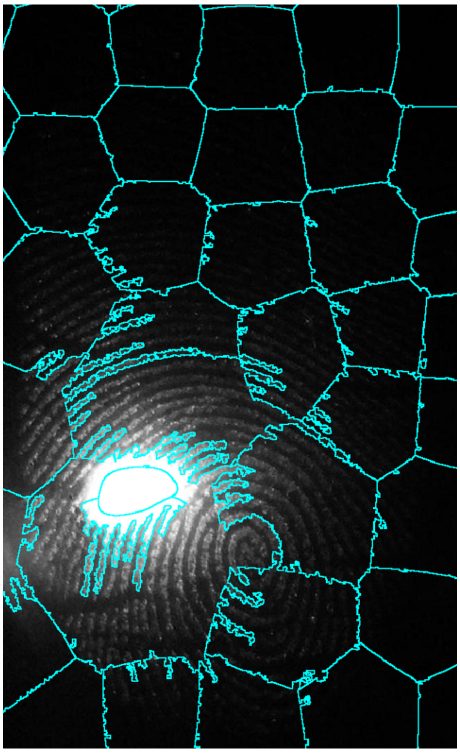

(b) Same MLIC image as (a) after superpixel segmentation.

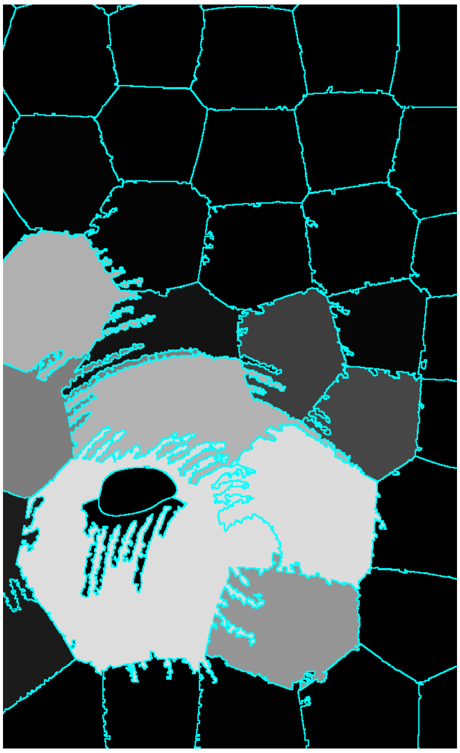

(c) Each superpixel from (b) is assigned the value of its predicted fingerprint probability.

(d) The resulting fingerprint image generated from RELF.

Figure 3.11: Generating a fingerprint image after superpixel segmentation using the RELF. (a) shows an MLIC image of a flat specular surface. In (b) we see the same MLIC image as (a) after superpixel segmentation. (c) shows an image of the superpixels from (a) where each superpixel is assigned the value of its predicted fingerprint probability. (d) shows the resulting fingerprint image generated from RELF.

3.7 Testing and training regimes for imbalanced data

We acquire fingerprint image stacks of various surfaces, each of which are then segmented into superpixels, then we generate a feature vector for each superpixel. We select different images stacks of varying surface specularity and colour for the purposes of training and then testing the performance of a model to recognise fingerprint superpixels. Multiple real-life binary classification problems such as locating diseased tissue in medical scans or identifying fraudulent transactions in financial data require learning from imbalanced data [31]. Binary classification is one of the most researched aspects of learning from imbalanced data [83], where the majority class is much more abundant than the minority class.

Given the nature of latent fingerprint imaging, the majority of the image (and hence superpixels) will not contain fingerprint, making negative (no fingerprint present) superpixels the majority class and positive (fingerprint present) superpixels the minority class. We choose 8 different training regimes so as to vary the ratio of minority to majority class, using different over-sampling and under-sampling methods to determine the effect on classifier performance and select the training regime which produces the best performance for fingerprint recognition.

3.7.1 Training

For training we acquire 14 fingerprint image stacks of various surfaces, each of which contain 92 images giving us a total of 14x92 = 1288 training images. Each of these are then segmented into 200 superpixels, giving us 1288x200 = $257,600$ training superpixels. In practice the SLIC superpixels algorithm [2] will generate slightly fewer superpixels than the input number, so the actual number of training superpixels generated was $207,712$. We then extract a 14x1 feature vector from each of these superpixels, yielding $207,712$ training feature vectors with 14 features. The surface types and example images used in the training set are shown in Figure 3.12. The various training regimes and their proportions of fingerprint (minority class) to non-fingerprint (majority class) after using over-sampling and under-sampling techniques are shown in Figure 3.14 and Figure 3.13.

Training regime 1

For training regime 1 we use the original feature vectors from the training image stacks with no over-sampling or under-sampling. As shown in table 3.16 this means the minority class (fingerprint) is severely imbalanced, with a ratio of fingerprint to non-fingerprint feature vectors of 1:277 with a total number of feature vectors of $N_{Total} = 207\,712$.

Training regime 2

For training regime 2 we randomly under-sample the majority class (non-fingerprint) from the training image stacks reducing it by 96.8%, resulting in minority class percentage of 10% and a majority class percentage of 90%. As shown in table 3.16, this results in a ratio

Surface type	Image of object
Black Sphere	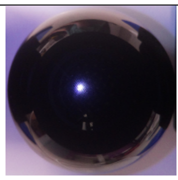
Glass Sphere	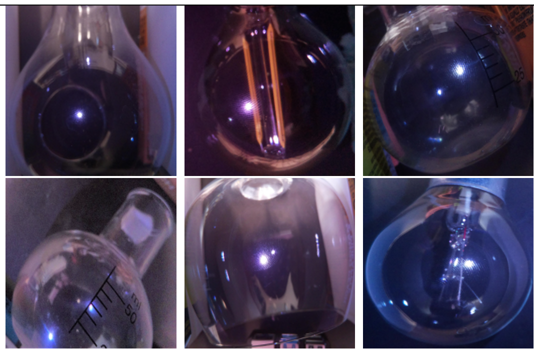
Glass Cylinder	
Chrome Cylinder	

Figure 3.12: The surface types and example images used in the training set are shown here.

of fingerprint to non-fingerprint feature vectors of 1:9, meaning training regime 2 is less imbalanced than training regime 1 with a total number of feature vectors of $N_{Total} = 7\,468$.

Training regime 3

For training regime 3 we randomly under-sample the majority class (non-fingerprint) and over-sample the minority class (fingerprint) from the training image stacks. We over-sample the 746 fingerprint feature vectors by a factor of 3 via image augmentation to generate three new over-sampled feature vectors from each original feature vector using three different image augmentations (as shown in Figure 3.15). We use these augmentations to generate a new feature vector from the original superpixel because they are fast to compute. Firstly we augment the original superpixel shown in Figure 3.15a through a pincushion distortion of random amplitude as shown in Figure 3.15b to generate our first new feature vector. Secondly we augment the original superpixel through skewing of random magnitude as shown in Figure 3.15c to generate a second new feature vector.

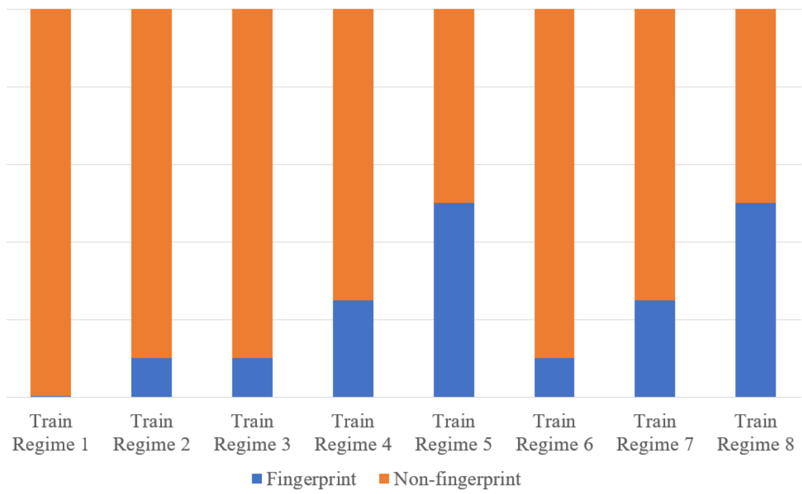

Figure 3.13: The 8 training regimes and their varying proportions of fingerprint (minority class) to non-fingerprint (majority class) after using over-sampling and under-sampling techniques described in Figure 3.14.

Training Regime	N_{Total}	% OS Rate	% US Rate	OS Method	US Method	% Minority Class	% Majority Class
1	207 712	0	0	None	None	0.4%	99.6%
2	7 468	0	96.8	None	Random	10%	90%
3	29 808	300	87	Augment	Random	10%	90%
4	11 922	300	95.7	Augment	Random	25%	75%
5	5 960	300	98.6	Augment	Random	50%	50%
6	29 839	300	87	SMOTE	Random	10%	90%
7	11 935	300	95.7	SMOTE	Random	25%	75%
8	5 967	300	98.6	SMOTE	Random	50%	50%

Figure 3.14: Training regimes used for fingerprint recognition. Here the N_{Total} column represents the total number of training feature vectors, % OS Rate refers to the percentage by which the minority class has been over-sampled, % US Rate refers to the percentage by which the majority class has been under-sampled, OS Method refers to the over-sampling method, US Method refers to the under-sampling method, % Minority Class shows the minority class as a percentage of the overall feature vectors used in a given training regime N_{Total} and % Majority Class shows the majority class as a percentage of the overall feature vectors used in a given training regime.

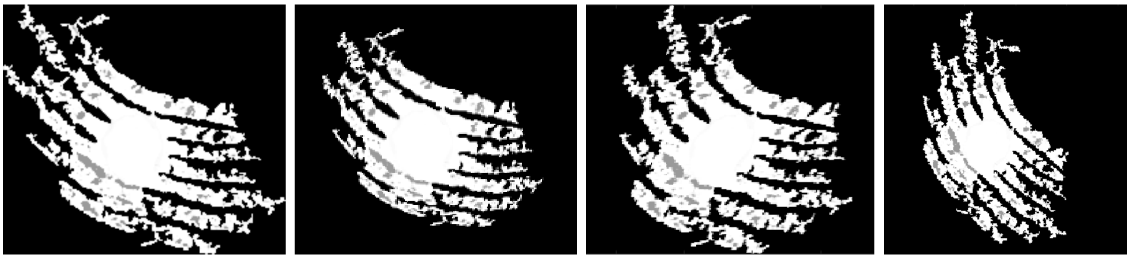

(a) Original. (b) Pincushion distortion. (c) Skewed. (d) Rotated.

Figure 3.15: Image augmentation for over-sampling minority class (fingerprint) in training regime 3. (a) Sample of exemplar fingerprint superpixel (b) The same superpixel after pincushion distortion of a random amplitude. (c) The same superpixel after skewing of a random magnitude. (d) The same superpixel after rotation by a random angle.

Thirdly we perform rotation by a random angle as shown in Figure 3.15d to generate a third new feature vector. We do this for each of the original N_{FP} =746 feature vectors labelled as fingerprint resulting in N_{FP} =2 980 feature vectors labelled as fingerprint after augmentation. As shown in table 3.14, we randomly under-sample the majority class (non-fingerprint) reducing it by 87%, resulting in minority class percentage of 10% and a majority class percentage of 90%, which is the same ratio as training regime 2, but results in a larger total number of feature vectors ($N_{Total} = 29\,808$).

Training regime 4

For training regime 4 we randomly under-sample the majority class (non-fingerprint) and over-sample the minority class (fingerprint) from the training image stacks. We over-sample the 746 fingerprint feature vectors by a factor of 3 via image augmentation, the same rate and method of over-sampling described in training regime 3. However, in training regime 4 we randomly under-sample the majority class (non-fingerprint) reducing it by 95.7%, resulting in minority class percentage of 25% and a majority class percentage of 75% and total number of feature vectors of $N_{Total} = 11\,922$.

Training regime 5

For training regime 5 we randomly under-sample the majority class (non-fingerprint) and over-sample the minority class (fingerprint) from the training image stacks. We over-sample the 746 fingerprint feature vectors by a factor of 3 via image augmentation, the same rate and method of over-sampling as we do for training regime 3 and 4. However, in training regime 5 we randomly under-sample the majority class (non-fingerprint) reducing it by 98.6%, resulting in minority class percentage of 50% and a majority class percentage of 50% and total number of feature vectors of $N_{Total} = 5\,960$. This means that for training regime 5, we have significantly reduced the total number of feature vectors, but have balanced the two classes.

Training regime 6

For training regime 6 we randomly under-sample the majority class (non-fingerprint) and over-sample the minority class (fingerprint) from the training image stacks. We over-sample the fingerprint feature vectors using synthetic minority over-sampling technique (SMOTE) [13]. Researchers have shown that classifier performance can be improved (in ROC space) by over-sampling the minority class using SMOTE and under-sampling the majority class rather than simply only under-sampling the majority class [13]. SMOTE works by choosing an sample at random from the minority class, then finds k of the nearest neighbours for that example in feature space (we use k=5). One of the k nearest neighbours, is then randomly chosen and a synthetic sample is generated at a randomly computed point along the line segment between the two minority class examples [35].

We use SMOTE to over-sample the original N_{FP} =746 fingerprint feature vectors by a factor of 3 to generate three new over-sampled feature vectors from each original feature vector, resulting in N_{FP} =2 980 feature vectors labelled as fingerprint after SMOTE. For training regime 6 we under-sample the majority class by 87%, resulting in minority class percentage of 10% and a majority class percentage of 90% which is the same ratio as training regime 2 and 3, but resulting in a larger total number of feature vectors (N_{Total} = 29 808) than training regime 2 but nearly the same as training regime 3.

Training regime 7

For training regime 7 we randomly under-sample the majority class (non-fingerprint) and over-sample the minority class (fingerprint) from the training image stacks. We over-sample the 746 fingerprint feature vectors by a factor of 3 using SMOTE, the same rate and method of over-sampling described in training regime 6. However, in training regime 7 we randomly under-sample the majority class (non-fingerprint) reducing it by 95.7%, resulting in minority class percentage of 25% and a majority class percentage of 75% and total number of feature vectors of N_{Total} = 11 922.

Training regime 8

For training regime 8 we randomly under-sample the majority class (non-fingerprint) and over-sample the minority class (fingerprint) from the training image stacks. We over-sample the 746 fingerprint feature vectors by a factor of 3 using SMOTE, the same rate and method of over-sampling as we do for training regime 6 and 7. However, in training regime 8 we randomly under-sample the majority class (non-fingerprint) reducing it by 98.6%, resulting in minority class percentage of 50% and a majority class percentage of 50% and total number of feature vectors of N_{Total} = 5 960. This means that for training regime 8, we have significantly reduced the total number of feature vectors, but have balanced the two classes.

Testing Regime Description	N_{Total}	% Minority Class	% Majority Class
Original data composition	71 872	0.26	99.7

Figure 3.16: The testing regime used for evaluating classifier performance. Here the N_{Total} column represents the total number of testing feature vectors % Minority Class shows the minority class as a percentage of the overall feature vectors used in the testing regime N_{Total} and % Majority Class shows the majority class as a percentage of the overall feature vectors used the testing regime.

3.7.2 Testing

For testing we acquire 6 fingerprint image stacks of various surfaces not included in training, each of which contain 92 images giving us a total of 6x92 = 552 testing images as shown in Figure 3.16. Each of these are then segmented into 200 superpixels, giving us 552x200 = 104 400 testing superpixels. In practice the number of testing superpixels was 71, 872 due to the SLIC superpixels algorithm generating slightly less superpixels than the number input. We then extract a 14x1 feature vector from each of these superpixels, yielding 71, 872 testing feature vectors with 14 features.

3.7.3 Classifiers

We train the following three models on the training regimes described in section 3.7.1.

Artificial neural network classifier

We train a two-layer feed-forward artificial neural network to learn from the superpixel feature vectors and use Bayesian regularisation [23; 55] to update the weights and biases according to Levenberg-Marquardt optimisation [64], minimising squared errors and weights resulting in a network with good generalisation (its ability to handle unseen data). We stop training when generalisation ceases to improve. The feed-forward network uses a hyperbolic tangent sigmoid transfer function [87] in its hidden layer (which consists of 10 hidden neurons) and a linear transfer function in its output layer.

Fine tree classifier

We train a fine tree classifier [78] to learn from the superpixel feature vectors. Our model has a maximum number of splits of 100 meaning it has high flexibility and has a large number of leaves to make many fine distinctions between classes. For our fine tree splitting criterion we use Gini's diversity index, which is calculated by subtracting the sum of squared probabilities of each class from 1, and a given feature with a lower Gini index is selected for a split [44].

Quadratic support vector machine classifier

We opt to train a support vector machine since they are effective in high dimensional feature spaces [72]. We train the support vector machine with a quadratic kernel function to learn from the superpixel feature vectors.

3.7.4 Performance of classifiers on testing data

In order to measure the performance of our classifiers we measure their precision, recall and F1 scores respectively. Precision is particularly important when the consequences of a false positive are significant. An example of this is detecting email spam, where a false positive could mean that a given email may be classified as spam when it in fact pertinent for the email user. Therefore if the spam detector is not of sufficiently high precision the user may lose valuable emails. Precision is calculated as shown in (3.3).

$$Precision = \frac{TruePositive}{TruePositive + FalsePositive} \tag{3.3}$$

Another performance metric of a classifier is recall, which is particularly important when the consequences of a false negative are significant. This is true for classifiers handling medical data, where a sick patient (true positive) may be classified as not sick (false negative), meaning the patient may not receive vital treatment. Clearly medical classifiers must have sufficiently high recall, which we calculate using (3.4).

$$Precision = \frac{TruePositive}{TruePositive + FalseNegative} \tag{3.4}$$

In machine learning the combination of precision and recall prove useful in measuring the performance of a classifier [47]. An alternative performance evaluation measure which combines precision and recall is the F1 score, which measures the harmonic mean of the two values, The measure was originally introduced in statistical ecology [49] and then applied to information theory [51] and then ultimately adopted the name F1 score [53]. The F1 Score may be optimised in order to find a balance between Precision and Recall, and is a useful metric if there is a large class imbalance. We compute the F1 score using (3.5).

$$F1 = 2 \times \frac{Precision \times Recall}{Precision + Recall} \tag{3.5}$$

Best performing model

We perform 10 fold cross-validation to compute the best performance (F1 Score) of the three models trained on the eight different training regimes as shown in Figure 3.17. It was found that the highest mean F1 Score across 10 folds was 0.961 obtained using a quadratic support vector machine (SVM) trained on training regime 8, which randomly

Training Regime	% Minority Class	% Majority Class	Neural Network F1 Score	Fine tree F1 Score	Quadratic SVM F1 Score
1	0.4%	99.6%	0.122	0.161	0.044
2	10%	90%	0.738	00.717	0.817
3	10%	90%	0.804	0.810	0.871
4	25%	75%	0.890	0.870	0.922
5	50%	50%	0.944	0.927	0.958
6	10%	90%	0.820	0.777	0.863
7	25%	75%	0.904	0.879	0.930
8	50%	50%	0.945	0.931	*0.960*

Figure 3.17: Performance (F1 Score) comparison of the three models trained on each of the eight training regimes with varying minority class and majority class percentages using the various over-sampling and under-sampling methods described in Figure 3.14 and tested on the testing data described in Figure 3.16. The results shown were computed using 10 fold cross-validation and the best trained model's F1 Score is italicised and underlined.

under-samples the majority class (non-fingerprint) and over-samples the minority class (fingerprint) using SMOTE. Training regime 8 has a minority class percentage of 50% and a majority class percentage of 50% meaning the two classes are balanced. Clearly when the classes are balanced the classifier performance improves, with the quadratic SVM trained on training regime 5 (which is also balanced but uses image augmentation to over-sample instead of SMOTE) coming in a close second with an F1 Score of 0.957. Despite training regimes 5 and 8 having a significantly reduced total number of feature vectors N_{Total}, the quadratic SVM yields the highest F1 score for these training regimes whilst the classes are balanced.

Despite the quadratic SVM trained on training regime 8 yielding the highest F1 score of 0.960, the neural network trained on training regime 8 was faster to train and test and yielded a comparatively high F1 score of 0.945. We decided to use this neural network as the classifier in RELF because of this increase in training and testing speeds, so we choose to perform the exhaustive feature search using a neural network.

In Figure 3.18 we show fingerprint images generated by a neural network trained on training regime 1 and training regime 8 respectively. Training regime 1 produced a very low F1 score of 0.122 and generated an NBIS match score of 20 for the image shown in Figure 3.18a. Training regime 8 produced a much higher F1 score of 0.960 and generated a greatly improved NBIS match score of 31 for the image shown in Figure 3.18b. The vastly improved F1 Score yielded by training regime 8 produces an improvement in NBIS match score of 11, which suggests that a higher F1 score does generate a higher quality fingerprint image.

(a) Training regime 1 NBIS match score: 20. (b) Training regime 8 NBIS match score: 31.

Figure 3.18: A neural network trained on training regime 1 produces the image shown in (a) which generates an NBIS match score of 20 and training regime 8 produces the image shown in (b) which generates a reduced NBIS match score of 31. These fingerprint images were extracted from a flat, black specular smart phone screen.

3.8 Exhaustive feature selection and cross-validation

In order to establish which of the fourteen features from section 3.4 contribute most to produce a correct fingerprint classification we perform exhaustive feature selection. As previously stated we use a neural network as the classifier in RELF because of its increase in training and testing speeds over the quadratic SVM. We train this neural network on Training Regime 8 (the best performing training regime) and compute an F1 score for each combination using the testing data described in section 3.7.2. Exhaustive feature selection is the most computationally expensive of all feature selection methods since it trains a model on all possible combinations of features and finds the optimal. Despite the computational expense, we perform an exhaustive search because it only needs to be performed once and increases the accuracy and speed of our machine learning model once the optimal combination of features is computed.

With the 14 features described in section 3.4 there are $16,384$ possible feature combinations (since $2^{14} = 16,384$). In our exhaustive search we evaluate the F1 Score of a a neural network classifier trained on each of these $16,384$ combinations using 10 fold cross-validation

3.8.1 Four most significant features

After performing an exhaustive feature search of all possible feature combinations, we compute the average F1 Score for every feature combination containing each of the features individually as shown in Figure 3.20. In this figure, column 1 represents the average F1 Score of every possible feature combination containing feature 1, and so on for the remaining columns. It is clear to see from Figure 3.20 that feature combinations containing the four Features 3, 7, 10 and 14 (Ratio of light to dark pixels, Variance in intensity, Entropy of the superpixel and Homogeneity (from GLCM)) yield the highest F1 Scores. These four features contribute most to producing a correct superpixel, and using these four features alone to train a neural network classifier produces an F1 Score of 0.920, which is only a reduction of 0.040 from using all features (which yields an F1 Score of 0.960 as shown in Figure 3.17), despite only using four features and dropping the remaining ten. A neural network classifier trained on these four features alone also produces the fingerprint shown in Figure 3.19a (extracted from the same fingerprint on a smart phone screen shown in Figure 3.18) which generates an NBIS match score of 25. This is an NBIS match score decrease of 6 from using all features with training regime 8 which yields the image shown in Figure 3.18b with a score of 31. This decrease may be expected since we are only using 4 of the 14 original features but shows that these 4 features are indeed fundamental for correct fingerprint classification since these four features alone can produce a comparatively high F1 score and NBIS match score. The circles and half circles which appear in these images are caused by reflections of the LEDs where the RELF algorithm has determined that these pixels are the most likely to contain fingerprint. This is likely due to some superpixels in the training set which have been labelled as containing fingerprint also containing a slight LED reflection.

3.8.2 Best feature combination overall

Finding the optimal feature combination is made more difficult by the fact that there is some amount of educated guesswork involved in choosing the original features. Feature selection allows us to evaluate the impact of each feature on the classifier performance. Features with high correlation have almost the same effect on classification, meaning when two features are correlated we can drop one of the two features. In Figure 3.20 features which have a similar average F1 score for every feature combination they are present in are likely somewhat correlated, which makes sense since for example features 8 and 9 (the median and modal superpixel intensity values) are very similar measures and have similar average F1 scores. Across all features the feature combination which produces the highest F1 Score for the neural network 0.951 was found through the exhaustive feature search and is shown in Figure 3.21. This feature combination produces an F1 Score of 0.951 using only Features 1, 2, 3, 4, 6, 7, 9, 10, 13 and 14, and does not use Features 5, 8, 11 and 12 (which are shown in Figure 3.22). Note that this optimal feature combination does not use feature 8 but does use feature 9 (the median and modal superpixel intensity values), likely because they are correlated so feature 8 is dropped. Since this feature combination uses Features 3, 7, 10 and 14, this supports the conclusions drawn in section 3.8.1 that these four features contribute most to producing a correct superpixel classification.

(a) Trained on Features 3, 7, 10 and 14 NBIS match score: 25.

(b) Trained on Features 1, 2, 3, 4, 6, 7, 9, 10, 13 and 14 NBIS match score: 30.

Figure 3.19: A neural network trained on the most significant four features described in section 3.8.1 produces the image shown in (a) which generates an NBIS match score of 25, while training on the best feature combination overall described in section 3.8.2 produces the image shown in (b) which generates an NBIS match score of 30. These images were extracted from the same fingerprint on a smart phone screen shown in Figure 3.18.

A neural network trained on these ten features alone also produces the fingerprint shown in Figure 3.19b (extracted from the same fingerprint on a smart phone screen shown in Figure 3.18) which generates an NBIS match score of 30. This is an improvement on using only the four most significant features (3, 7, 10 and 14) as described in section 3.8.1 which produces an NBIS match score of 25 as shown in Figure 3.19a. However, with an NBIS match score of 30, the fingerprint image in Figure 3.19b is just shy of the match score obtained from using all 14 features shown in Figure 3.18b which was 31. Therefore, despite these 10 features producing a higher F1 score than using all 14 (0.951 compared to 0.945), the fingerprint generated by this network appears to be of slightly less quality than when using all 14. This suggests that the F1 score is a good indicator overall of the networks ability to classify fingerprints, since generally speaking lower F1 scores produce lower NBIS match scores, however when the F1 scores are very similar then the match score may vary slightly.

Given that using all 14 features yields the highest NBIS match score despite having a marginally lower F1 score, we choose to use all of the 14 features when classifying fingerprints with RELF.

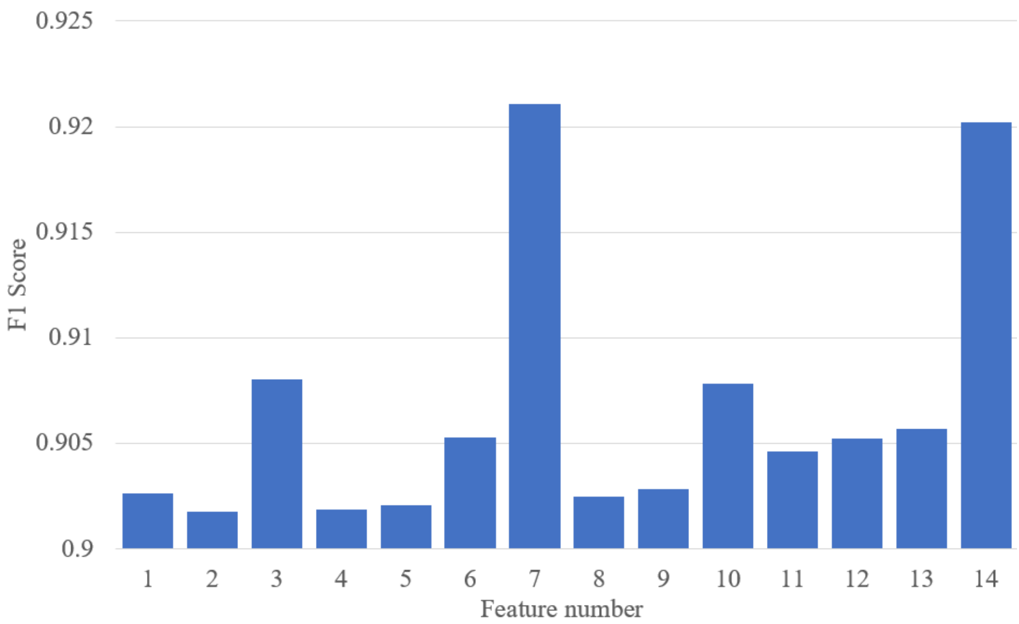

Figure 3.20: The average F1 Score of each feature combination containing each feature after an exhaustive feature search. In this figure, column 1 represents the average F1 Score of every possible feature combination containing feature 1, and so on for the remaining columns. Note that the y axis is between 0.9 and 0.925 to better visualise the difference.

Feature Number	Used features
1	Number of potential fingerprint ridges
2	Cross correlation with filter
3	Ratio of light to dark pixels
4	Aspect ratio of superpixel
6	Convex hull over perimeter ratio
7	Variance in intensity
9	Mode value of intensity
10	Entropy of the superpixel
13	Energy (from GLCM)
14	Homogeneity (from GLCM)

Figure 3.21: Features used in the overall best feature combination after the exhaustive search, producing an F1 Score of 0.961.

Feature Number	Dropped features
5	Perimeter over area ratio
8	Median value of intensity
11	Contrast (from GLCM)
12	Correlation (from GLCM)

Figure 3.22: Features dropped from best feature combination after the exhaustive search.

3.9 Results

We demonstrate our RELF method on prints from five objects of varying surface characteristics, showing that it is capable of extracting fingerprints from planar, curved and spherical specular surfaces. As noted in 3.2, when the principal curvatures κ_1 and κ_2 increase from zero on a planar surface, to one becoming non-zero on a cylindrical surface until both are non-zero on a spherical surface, the mean curvature also increases. The mean curvature (the average of κ_1 and κ_2) of a surface is indicative of the ease at which we may extract fingerprints. We see this is true for the phone screen in Fig. 3.23(a)-(c), where the quality and completeness of the latent fingerprint is high. We further evaluate RELF on a specular cylindrical glass jar in Fig. 3.24(a)-(c). It is clear that the fingerprint is missing some portions, yet overall we yield a high quality, mostly complete latent print. This shows the robustness of RELF to work on different surface curvatures. We then evaluate RELF's performance on a clear (dome-lit) specular spherical light-bulb, as can be seen in Fig. 3.25(a)-(c). Since both principal curvatures are now non-zero for this surface, each input image contains only small portions of the fingerprint at best. This makes it much more difficult for RELF to extract latent prints, but the technique produces a mostly complete fingerprint nonetheless. This surface is additionally difficult to extract fingerprints as the curved and transparent light-bulb contains filament elements which are visible and disruptive to the extraction process. Despite this, RELF proves to be robust in outputting fingerprints in these most undesirable of circumstances.

We also extract fingerprints from a mug which has a particularly challenging combination of properties: it is black in colour, specular and curved. The fingerprint outputted from RELF is shown in 3.26c, which shows the stark contrast between the region of the unprocessed image in 3.26b. We show our novel technique is also capable of extracting fingerprints from further problematic surfaces such as the (dome-lit) white spherical specular bulb in Fig. 3.27c.

(a) Context image of (specular) flat phone screen.

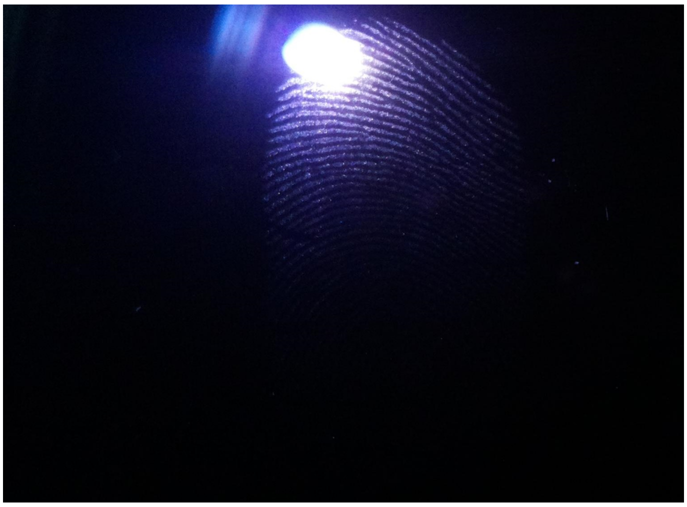

(b) Cropped MLIC image of phone screen shown in (a).

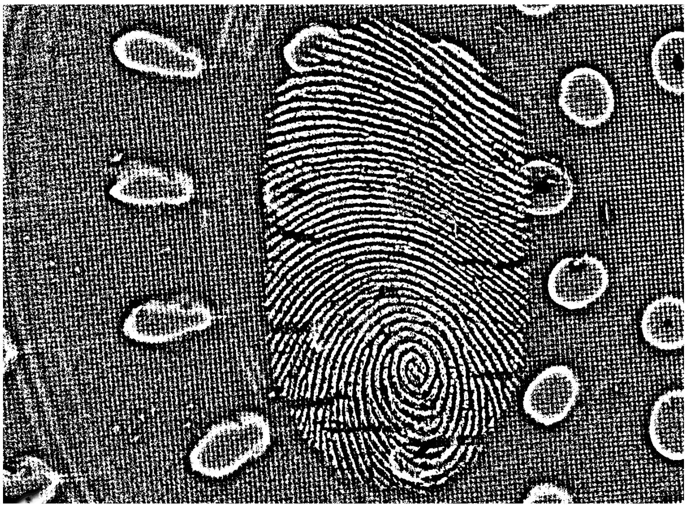

(c) RELF fingerprint extracted from same MLIC as (a).

Figure 3.23: Fingerprints extracted using the RELF method on a planar specular surface. In (a) we see the flat surface of a phone screen. (b) shows a cropped region of a MLIC image of the phone screen shown in of (a) for comparison. (c) shows the same cropped region as (b) with the extracted RELF fingerprint.

3.10 Conclusions

In this chapter we present a multi-light imaging based method for extracting latent fingerprints from surfaces without the addition of contaminants or chemicals to the evidence. We show our technique works on notoriously difficult to image surfaces, using off-the-shelf cameras. In particular, we extract images of latent fingerprints from surfaces which are transparent, curved and specular such as glass light-bulbs and jars, which are challenging forensically due to their curvature and shininess. Our method produces results comparable to more invasive methods and leaves the fingerprint sample unaffected for further forensic analysis.

We perform an exhaustive feature search in section 3.8 and concluded which features contribute most to correct fingerprint classification, but choose to use all of the 14 features when classifying fingerprints with RELF given that using all 14 features yields the highest NBIS match score despite having a marginally lower F1 score. The results of this exhaustive search will help in future optimisation of the model.

In real-life when a fingerprint is used as evidence, a forensic expert is relied upon to determine the quality of the print [84]. If a person sat down and inspected all RELF input images they could identify the fingerprint portion - RELF simply performs this automatically, and efficiently adds all fingerprint portions into one image uncovering the true latent fingerprint.

As stated in section 1.3.3, RTI is stated to run into difficulty when imaging specular surfaces. We show that multi-light imaging is capable of extracting fingerprints from planar, curved and spherical specular surfaces. Moreover, we show the method is capable of extracting fingerprints from these difficult specular surfaces when they are transparent (see Fig. 3.23c), black (see Fig. 3.26c) and white (see Fig. 3.27c).

Our technique performed well on real world surfaces and objects with no preparation such as the mobile phone screen shown in Fig. 3.23c, opening up the technique to potentially be used in crime scenes. There is no exact number of lighting directions required by RELF, we use around 90 which seems to be sufficient. The method is dependant on the light illuminating the region containing fingerprint which could appear anywhere in the image, so the more lights we use should mean more likelihood of capturing the fingerprint. It is likely that the number of light directions used is related to the degree of curvature of the surface.

These results are highly promising, but we realise that the latent fingerprint image is distorted due to the curvature of the surface on which it sits, so in chapter 5 we introduce an automatic method for correcting surface curvature.

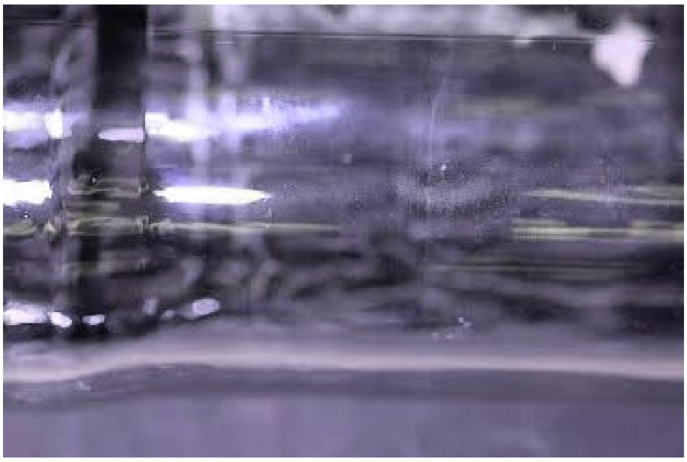

(a) Input image of (specular) clyindrical surface.

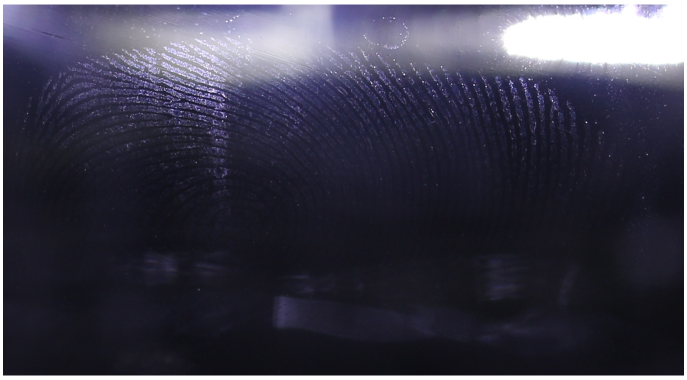

(b) Cropped region of (a).

(c) RELF data overlayed on cropped region of (a).

Figure 3.24: Fingerprints extracted using the RELF algorithm on a cylindrical specular surface. It can be seen that there are portions of the fingerprint missing, due to the mis-classification of a small number of superpixels for which lighting may not have been adequate or the SLIC superpixels algorithm may have segmented a small number of unusually shaped superpixels. In (a) we see the cylindrical surface of a glass jar. (b) shows a cropped region of (a) for comparison. (c) shows the same cropped region as (b) with the extracted RELF fingerprint.

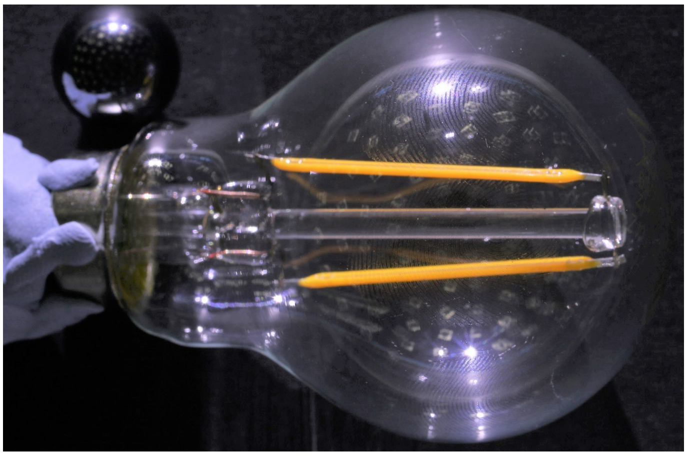

(a) Input image of (specular) spherical surface.

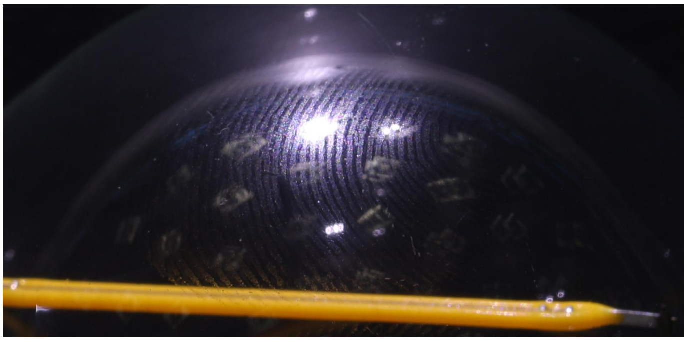

(b) Cropped region of (a).

(c) RELF data overlayed on cropped region of (a).

Figure 3.25: Fingerprints extracted using the RELF method on spherical specular surfaces. It can be seen that there are portions of the fingerprint missing, due to the mis-classification of a small number of superpixels for which lighting may not have been adequate or the SLIC superpixels algorithm may have segmented a small number of unusually shaped superpixels. In (a) we see the spherical surface of a glass light-bulb. (b) shows a cropped region of (a) for comparison. (c) shows the same cropped region as (b) with the extracted RELF fingerprint.

(a) Input image: black, specular, curved.

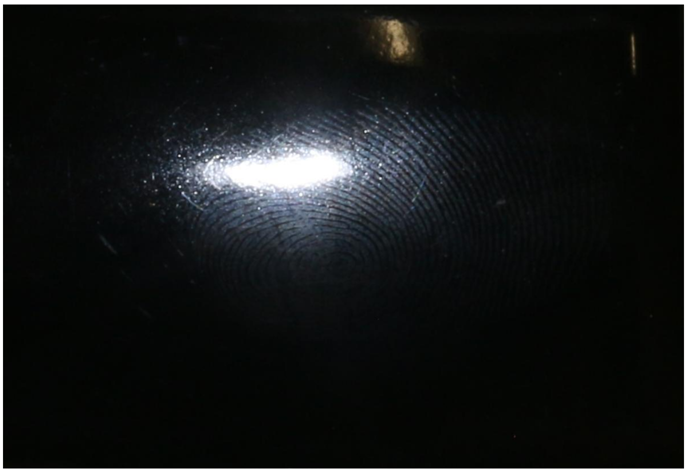

(b) Cropped region of (a).

(c) RELF data overlayed on cropped region of (a).

Figure 3.26: Fingerprints extracted using the RELF method on a black curved specular surface (a mug). In (a) we see the specular curved black surface of a mug. (b) shows a cropped region of (a) for comparison. (c) shows the same cropped region as (b) with the extracted RELF fingerprint.

(a) Input image: white, specular, spherical

(b) Cropped region of (a).

(c) RELF data overlayed on cropped region of (a).

Figure 3.27: Fingerprints extracted using the RELF method on a white specular spherical bulb. In (a) we see the white spherical surface of a glass light-bulb. (b) shows a cropped region of (a) for comparison. (c) shows the same cropped region as (b) with the extracted RELF fingerprint.

4 Prototype RELF hardware

Following the publication of our results (see [58] and chapter 3), the UK Metropolitan Police Service expressed interest in developing a RELF prototype. This project aimed to produce a handheld prototype device which is capable of capturing multi-light imaging collections of surfaces containing fingerprints to then be processed using the RELF algorithm. The device was then tested to find fingerprints on a variety of surfaces, including difficult curved and specular surfaces such as light-bulbs as well as vehicle bodywork. In this chapter we will describe the standardised prototype which is fundamental to the method presented in chapter 5, which extends RELF with automated curvature distortion correction.

4.1 Prototype device for Metropolitan Police Service

Recent advances in single board computers allow us to present a portable device for RELF which fully automates the lighting, image capturing and image processing to identify and mosaic certain portions of fingerprint visible only using certain light directions. We use a Raspberry Pi 4B (an off-the-shelf small single-board computer) with 4GB of RAM to control the lighting and simultaneously capture one image per light direction. The LED lights as well as the camera module are housed in a small hemisphere (in our case 125mm x 125mm x 65mm). For imaging we use the Raspberry Pi's 8 megapixel camera module which gives enough resolution to preserve the fine detail of fingerprint ridges, given that image quality impacts the effectiveness of fingerprint feature point extraction [89]. A full component list is shown in Figure 4.3.

As we illuminate each LED the latent print is only partially visible depending on the lighting direction, meaning we see different small regions of the fingerprint. This can be seen in Figure 3.4 where the specular reflection is saturated, but the surrounding region contains an eligible portion of the fingerprint. After testing different prototype designs, it was found that 92 LEDs inside a 3D printed hemisphere (shown in Figure 4.1) are more than enough to provide sufficient directional lighting coverage of the surface. Using the multi-light image technique we light each of the 92 LEDs and obtain an image for each light direction. The camera is positioned at the apex of the dome and captures an image for each unique lighting direction.

This standardised prototype device is fundamental to the method presented in chapter 5, which extends RELF with automated curvature distortion correction. The MLIC images captured by the device are processed through the RELF algorithm [58] to extract the

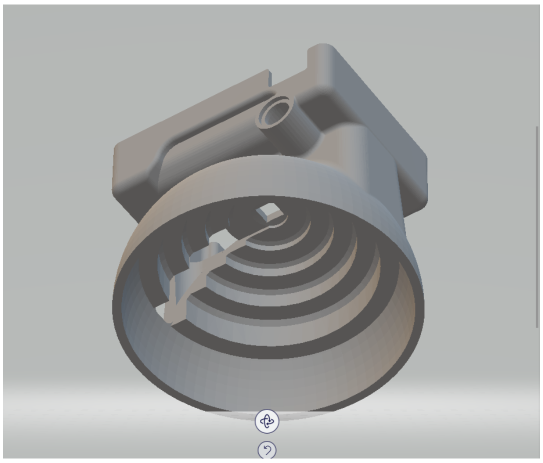

(a) 3D prototype model from below.

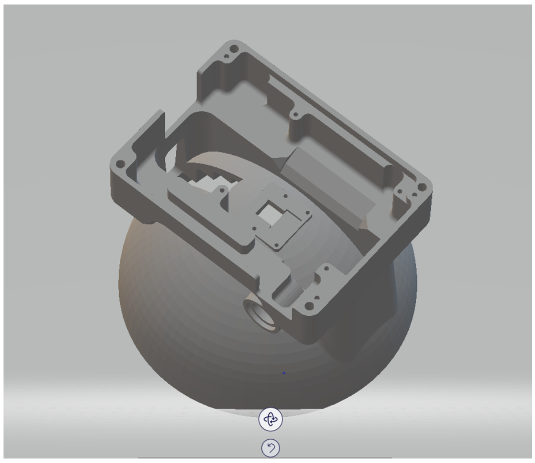

(b) 3D prototype model from above.

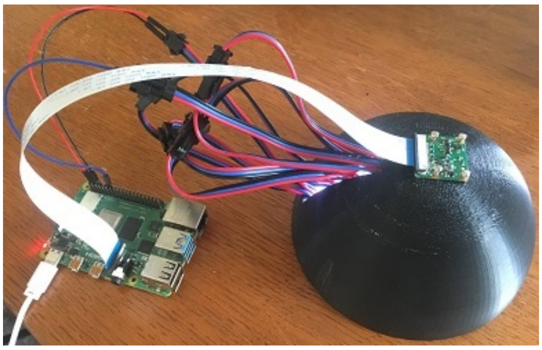

(c) Raspberry Pi and hemishphere housing LED lights and camera.

(d) Hemisphere from beneath with lights on and camera at apex.

Figure 4.1: The 3D prototype model of the multi-light imaging device for capturing latent prints. (a) shows the 3D model from below, where the concentric ring pattern inside the dome is designed to house the LED rings. (b) shows the 3D model from above, where the compartment on top of the dome is designed to house the Raspberry Pi. The RELF hemispherical lighting dome is shown in (c) with the camera at the apex connected to the Raspberry Pi (left). The image in (d) shows the LED lights (note all the lights are turned on here for illustrative purposes, in operation of the device only one LED is lit at a time).

fingerprints as outlined in section 5.1.2, then the surface curvature is automatically estimated as described in section 5.2.2, allowing us to correct surface curvature distortions as described in section 5.2.3.

4.2 Setting device LED intensity

The brightness of the LEDs used to illuminate the latent fingerprint surface from the prototype device shown in Figure 4.1 has a significant impact on the extracted fingerprint. The LEDs we use are individually addressable and have an adjustable intensity, so we are able to change LED intensity as required. The fingerprint image in Figure 4.2d shows the effect of using a low light level, whereas the image in Figure 4.2f was generated using a higher light level. In Figure 4.2d the image is more noisy and LED blob shaped reflections are visible due to there being less high quality fingerprint regions available for our RELF [58] method to mosaic together. In Figure 4.2d the fingerprint is adequately lit so that there are enough high quality fingerprint regions available for our RELF [58] method to mosaic together. For the surfaces used in this thesis it was found that an LED illumination of 20% of maximum intensity achieves the highest matching score, since other illumination levels introduce LED reflection artefacts from the latent print either not being illuminated enough for our RELF method to detect or being saturated when the LEDs are too bright.

The 20% maximum intensity value was found to be the optimal intensity for achieving the highest match score after imaging different objects under the same viewing conditions whilst varying the intensity. This optimal intensity was found to illuminate the fingerprint the right amount so as to make the fingerprint visible and avoid saturation.

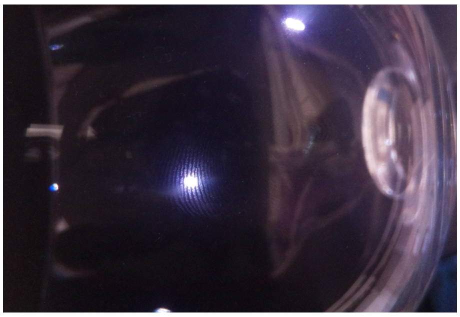

(a) Source image of gin glass containing fingerprint.

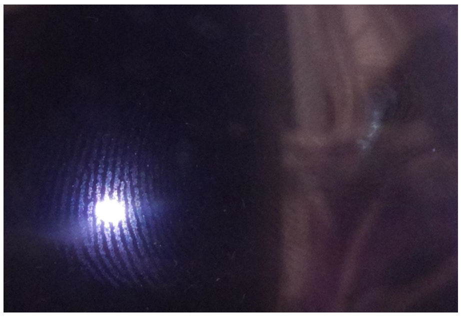

(b) Source image of gin glass containing fingerprint.

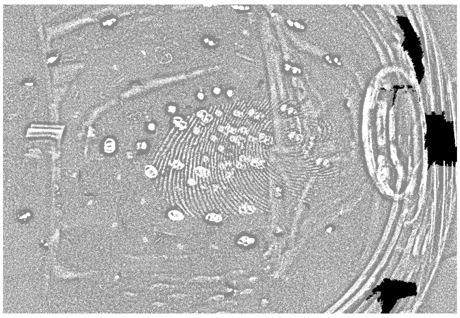

(c) RELF with LED intensity at lowest setting.

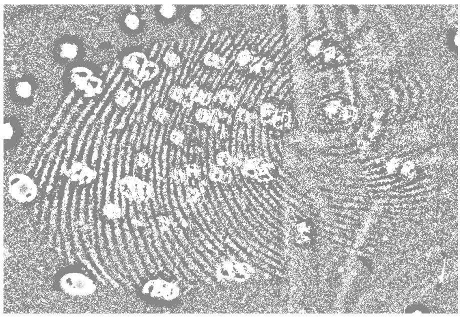

(d) RELF with LED intensity at lowest setting.

(e) RELF with LED intensity 50x higher than lowest setting.

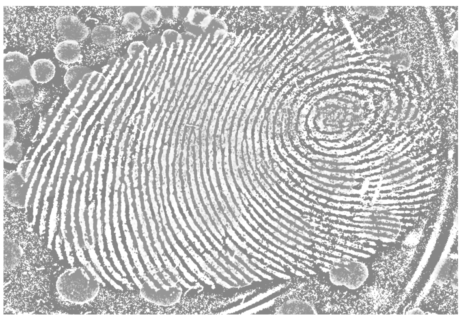

(f) RELF with LED intensity 50x higher than lowest setting.

Figure 4.2: The 3D prototype model of the multi-light imaging device for capturing latent prints. (a) shows the 3D model from below, where the concentric ring pattern inside the dome is designed to house the LED rings. (b) shows the 3D model from above, where the compartment on top of the dome is designed to house the Raspberry Pi.

Component	Description
Raspberry Pi 4 (4GB)	Operates the camera and lights.
Raspberry Pi Camera Module 2 (8MP)	8 megapixel camera to capture images.
8 LED 32mm Ring - WS2812B 5050 RGB LEDs	Smallest LED ring fitted nearest camera.
12 LED 52mm Ring - WS2812B 5050 RGB LEDs	LED ring fitted around the 8 LED ring.
16 LED 72mm Ring - WS2812B 5050 RGB LEDs	LED ring fitted around the 12 LED ring.
24 LED 92mm Ring - WS2812B 5050 RGB LEDs	LED ring fitted around the 16 LED ring.
32 LED 112mm Ring - WS2812B 5050 RGB LEDs	LED ring fitted around the 24 LED ring.
125mm x 125mm x 65mm 3D printed hemisphere	Lighting dome to house the LED rings and camera.

Figure 4.3: Components required to construct the prototype RELF device.

5 Extending RELF with contactless fingerprint extraction method with automated curvature distortion correction

The following article has been published using material from this chapter:

McGuigan, M., and Christmas, J. (2022). Contactless automated lifting of latent fingerprints from difficult curved surfaces. In Signal Processing: Image Communication (Vol. 109, p. 116858). Elsevier BV.
https://doi.org/10.1016/j.image.2022.116858

Furthering our work from chapter 3, we present a novel method which is able to automatically correct for surface curvature distortion and improve fingerprint matching scores using the LED pattern from the prototype device described in chapter 4 which also captures the multi-light imaging collection. This novel method extends RELF and is rapid, automatic, zero-contact and chemical-free, and able to obtain high quality fingerprint images from (forensically) difficult curved surfaces that are specular and/or transparent. We demonstrate that automatic surface curvature distortion correction improves fingerprint matching scores, often significantly, across a range of objects commonly found at a crime scene.

5.1 Introduction

In chapter 3 we introduce a rapid, chemical-free and non-contact photographic method for the Remote Extraction of Latent Fingerprints (RELF). In this chapter we extend RELF using exactly the same imaging prototype device to present a novel technique which is capable of *automatically* detecting surface curvature and corrects for surface curvature distortions, *improving* the fingerprint match score. As noted by the UK Government Home Office's Fingerprint Source Book [9] (and a private correspondence with the Covert Policing branch of the Metropolitan Police [60]), curved and shiny surfaces (both opaque and transparent) pose significant challenges for forensic investigators in extracting latent fingerprints.

Surface curvature is critical to fingerprint matching since algorithms use the relative distance between minutiae to obtain a match score [15] and curved surfaces distort these distances between minutiae [5]. Previous researchers have developed *reduced* contact latent print extraction methods [5] and noted that curved surfaces are additionally difficult because they introduce distortion to the fingerprint. Their technique is faster than more traditional methods and corrects for surface curvature distortions on cylindrical surfaces, but it is still invasive since it involves adding a material (glue vapour), and the surface curvature is measured manually. In section 5.1.1 we provide some essential background about latent fingerprints and more detail of the method introduced in [5]. In section 5.1.2 we summarise the key characteristics of RELF, as first described in [58], and in section 5.1.3 discuss surface curvature. The new method is described in section 5.2, and the experimental results are described in section 5.3 which demonstrate the new method across a range of different surfaces and show some very significant increases in fingerprint matching scores. Conclusions are drawn in section 5.4.

5.1.1 Related work

Historically, it has been noted by forensic investigators that through varying the angle of torch light incident on a surface containing latent fingerprints, it is possible to locate partial or full fingerprints [79].

More recently, this method of shining a torch on an object by hand to reveal latent prints has been employed [5], where it was also possible to correct for surface curvature distortions by measuring objects manually.

It is important to note here that before shining a hand-held torch on the object the authors deposit vaporised glue to develop the print and improve clarity for photography. This is different from our method, which uses *no* chemicals and is completely contact free, entirely preserving the print.

The authors measure the dimensions of a surface manually with a ruler and take a separate photograph of the side of the object to measure distances by inspecting the photograph. The authors yield impressive results in improving the matching scores after the distortion correction is applied, but they render the print compromised for DNA analysis.

Despite their results, the method proposed in [5] involves manually illuminating the object by hand (which takes some time to get the lighting just right), manually measuring the dimensions of the surface and then manually applying superglue vapour to develop the print. Although the method offers an increase in speed from more traditional methods, all of the manual steps mean the fingerprint extraction process is still considerable and the invasiveness renders the fingerprint sample unusable for further forensic testing.

Moreover, the authors in [5] state they would like to expand their method to work on surfaces curved in two dimensions since their method only works for cylinders (which have one curved dimension). Correspondingly, the method proposed in this chapter is fully capable of extracting latent prints from surfaces curved in two dimensions (such as spheres).

5.1.2 Remote extraction of latent fingerprints (RELF)

In this chapter we utilise the same technology as RELF, but perform surface curvature estimation (in section 5.2.2) and correct for the corresponding distortions caused (in section 5.2.3). It is shown in section 5.3 that our technique significantly improves the fingerprint matching score after correcting for surface curvature. We will now discuss the zero contact automated lifting of latent prints from curved surfaces, describing the automated surface curvature estimation and distortion correction in detail.

5.1.3 Types of surface curvature

Generally, fingerprint imaging becomes more difficult as the mean curvature (M) increases. As a result, we extract prints from curved surfaces with large M (see section 5.3) in order to show our method's ability to extract prints from challenging surfaces. The mean curvature of a cylinder ($M_{cylinder}$) is only dependent on the principal curvature κ_1 (since $\kappa_2 = 0$), so the mean curvature of a cylinder may be expressed as follows.

$$M_{cylinder} = \frac{\kappa_1}{2} = \frac{1}{2R_{curvature}} \tag{5.1}$$

In (5.1) the radius of curvature is represented by $R_{curvature}$. Spheres have larger M than cylinders since both principal curvatures are positive and *equal* (i.e. $\kappa_1 = \kappa_2$). We also extract prints from spheres to demonstrate our method's effectiveness. The mean curvature of a sphere is computed as follows.

$$M_{sphere} = \kappa_1 = \kappa_2 = \frac{1}{R_{curvature}} \tag{5.2}$$

Our method successfully extracts fingerprints from these challenging surfaces (such as the chrome cylindrical surface in Figure 5.10f and the transparent spherical bulb in Figure 5.11i) and corrects for surface curvature distortions which improves the fingerprint match score. Our method's ability to correct for surface curvature distortions and improve the fingerprint match score for cylindrical surfaces is shown in Figure 5.10 as well as spherical surfaces in Figure 5.11.

5.2 Methods

Our method utilises the standardised off-the-shelf and inexpensive hardware described in section 4, so that the lighting directions are the same in every MLIC. This enables us to use the expected light reflection from each lighting direction to estimate surface curvature. In section 5.2.1 we describe how the fingerprint images are captured with *zero* contact or chemicals required, before they are then processed using our RELF algorithm [58] which identifies portions of fingerprint and mosaics them (as described in section 5.1.2). In section 5.2.2 we then measure the change in locations of the LED reflections to estimate surface orientation and curvature *automatically*, then compensate for any distortions this curvature may cause in the fingerprint image in section 5.2.3. Each of these steps make up our pipeline for zero contact automated lifting of latent prints from curved surfaces, as is shown in Figure 5.1.

The surfaces investigated here are considered to be forensically interesting as they are commonly found at crime scenes such as light bulbs, drinking glasses and jars. In future work we may consider to estimate curvature different non cylindrical or spherical surfaces and compensate for their surface curvature distortion. Transparent, curved and specular such as glass light-bulbs and jars, which are challenging forensically due to their curvature and shininess.

5.2.1 Image acquisition

For imaging we use use the standardised RELF MLIC dome prototype as described in chapter 4. Each LED used to illuminate the latent print is only partially visible depending on the lighting direction, meaning different small regions of the fingerprint are shown in

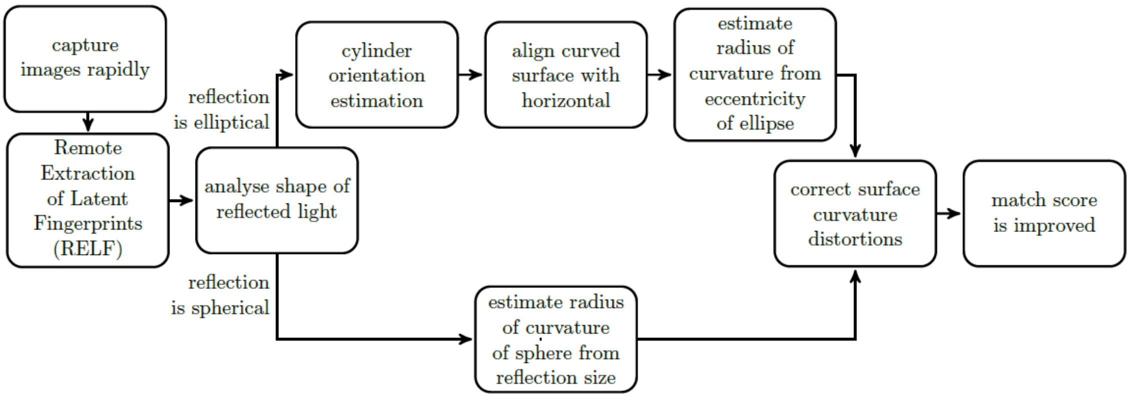

Figure 5.1: Pipeline for the zero contact automated lifting of latent fingerprints from curved surfaces

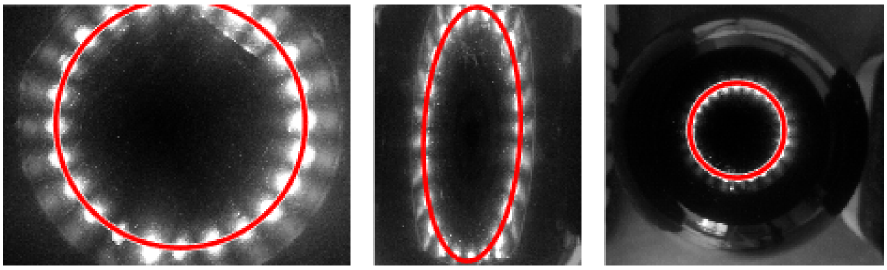

(a) LED reflection from a flat surface. (b) LED reflection from a cylindrical surface. (c) LED reflection from a spherical surface.

Figure 5.2: The LED reflection from the lighting hemisphere for a flat surface is shown in (a), and as expected the reflected pattern simply shows the ring formation of the LEDs. The figure in (b) shows the LED reflection from a curved surface, where the reflected pattern is elliptical instead of circular due to distortions from the curved surface. In figure (c) shows the LED ring reflected on a spherical surface, resulting in the reflection maintaining its circularity but appearing much smaller than the circular reflection from the flat surface in (a). The shape of these reflections is analysed to determine the surface curvature. Here the ellipse fitting is shown by the red line.

one given image. This can be seen in Figure 3.4 where the specular reflection is saturated, but the surrounding region contains an eligible portion of the fingerprint.

The images are then processed through the RELF algorithm [58] to extract the fingerprints as outlined in section 5.1.2, then in section 5.2.2 surface curvature is automatically estimated allowing us to correct surface curvature distortions in section 5.2.3.

5.2.2 Automatic surface curvature estimation

Using the hand-held, 12.5cm diameter dome described in chapter 4, we use the the LED reflection locations to estimate surface curvature and orientation. In Figure 5.2 the reflection pattern caused by the LED lights from the light dome reflecting on different surface types is shown, where the ellipse fitting is shown by the red line. The LED ring reflection for a flat surface is shown in Figure 5.2a, and as expected the reflected pattern simply mirrors the ring formation of the LEDs. The figure in Figure 5.2b shows the LED ring reflection for a cylindrical curved surface, where the reflected pattern is elliptical (instead of circular) due to curvature. In Figure 5.2c the LED ring reflection for a spherical surface is shown, where the LED ring maintains its circularity in the reflection but is much smaller than the reflection from the flat surface in Figure 5.2a.

This means that if the LED ring reflection is elliptical we may infer the distortion is cylindrical, and if the reflection is circular and smaller we may infer the distortion is spherical.

The LED reflection location within the image is computed in section 5.2.2 and fit an ellipse to these points. In section 5.2.2 our automatic cylinder curvature estimation through fitting an ellipse to the reflected LED pattern is described, and in section 5.2.2 the orientation of the cylinder is computed. In section 5.2.2 our automatic spherical curvature estimation method is described. Once our method estimates the surface curvature type from these reflections, it then automatically undoes any geometric distortion of the fingerprint caused by the curvature of the surface (as outlined in section 5.2.3 for cylinders and section 5.2.3 for spheres).

Automated LED reflection location estimation

In (5.3) the pixel coordinates of the reflection caused by a given LED in the image are automatically calculated.

$$(\mathbf{x}, \mathbf{y})_{LED} = mode\left((x_1, ..., x_n, y_1, ..., y_n)_{max}\right) \tag{5.3}$$

The location of the reflection caused by a given LED, $(\mathbf{x}, \mathbf{y})_{LED}$, is automatically estimated by finding the pixel coordinates of all n pixels with an intensity equal to the brightest pixel in the image, $(x_1, ..., x_n, y_1, ..., y_n)_{max}$ then compute their modal pixel coordinates.

Once the location of the LED reflection is obtained, $(\mathbf{x}, \mathbf{y})_{LED}$, for every LED in the LED ring, the surface curvature may then be estimated. As shown in Figure 5.2, the surface is *cylindrical* if the LED ring reflection is *elliptical*, and the surface is *spherical* if the reflection is *circular and smaller*.

Automated ellipse fitting for cylinder estimation

For cylindrical surfaces the surface curvature is computed by fitting an ellipse to the LED ring reflection as shown in Figure 5.3a. This allows us to compute the mean curvature and hence determine the correct distortion correction to apply. In Figure 5.4 it is shown that as the cylinder radius increases, the eccentricity of the LED ring reflection decreases and hence the reflection becomes less distorted. This makes sense because reflections on small cylindrical objects appear more distorted and warped than reflections on larger cylinders. Similarly a latent print on an increasingly large cylinder will begin to appear approximately flat and exhibit less distortion.

An ellipse is fitted to the ring's LED reflection coordinates (as computed in section 5.2.2) using the general equation of an ellipse which is given below in (5.4) for ellipse fitting (as shown in 5.3a).

$$a\mathbf{x}^2 + b\mathbf{x}\mathbf{y} + c\mathbf{y}^2 + d\mathbf{x} + e\mathbf{y} + f = 0 \tag{5.4}$$

Here a, b, c, d, e, f are the ellipse parameters and $\mathbf{x}$ and $\mathbf{y}$ are the coordinates of the modal value of x and y values from all $(\mathbf{x}, \mathbf{y})_{LED}$ as defined in (5.3). We then define γ as equal to the term in (5.5) for convenience.

$$\gamma = \sqrt{(a-c)^2 + b^2} \tag{5.5}$$

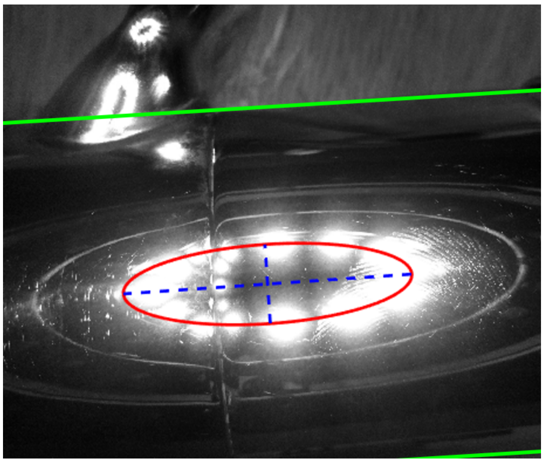

(a) LED reflection from a cylindrical surface.

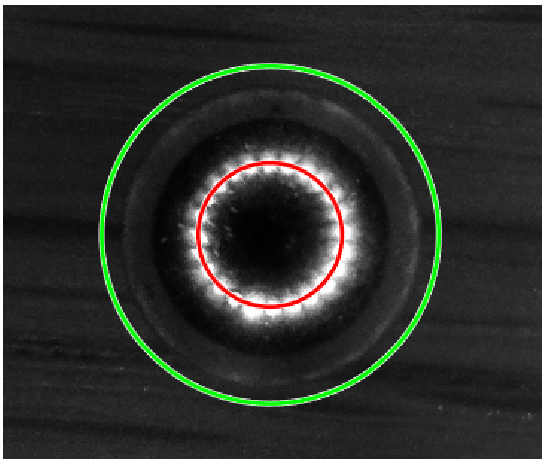

(b) LED reflection from a spherical surface.

Figure 5.3: In (a) shows the ellipse fitting for a reflection of an LED ring as outlined in section 5.2.2. The red line shows the fitted ellipse with the dashed blue line showing the ellipses semi major and semi minor axes, and the green line shows the estimated perimeter of the cylindrical surface. In (b) we see the circle fitting for a reflection of an LED ring as outlined in section 5.2.2. The red line shows the fitted circle and the green line shows the estimated perimeter of the spherical surface.

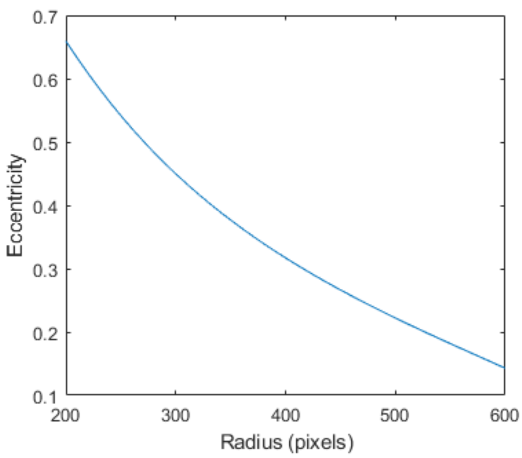

Figure 5.4: For cylindrical curved surfaces curved we use the eccentricity of the reflected LED ring to determine the radius of curvature of the surface using this geometrically calculated curve.

The semi-major and semi-minor axes (A and B) are now computed using γ and the ellipse parameters as shown in (5.6) and (5.7), allowing us to calculate the eccentricity of the ellipse.

$$A = \frac{-\sqrt{2(ae^2 + cd^2 - bde + (b^2 - 4ac)f)((a + c) - \gamma)}}{b^2 - 4ac} \tag{5.6}$$

$$B = \frac{-\sqrt{2(ae^2 + cd^2 - bde + (b^2 - 4ac)f)((a + c) + \gamma)}}{b^2 - 4ac} \tag{5.7}$$

The axes A and B are shown as dashed lines in the ellipse fitted to the reflected LED ring in Figure 5.3a. Finally we have enough information to compute the eccentricity of the ellipse (E_0) as shown in (5.8) below.

$$E_0 = \sqrt{1 - \frac{B^2}{A^2}} \tag{5.8}$$

From (5.8) it is shown that eccentricity is equal to zero when the semi-major and semi-minor axes (A and B) are equal, as is the case for a circle since by definition is the radius is constant from any straight line drawn between the circle centre to the perimeter.

As stated previously, eccentricity of the LED ring reflection is used to infer that the surface is curved and cylindrical. The radius of curvature ($R_{curvature}$) may now be estimated from the eccentricity (E_0) using the plot shown in Figure 5.4.

The cylinder orientation is then estimated using the ellipse parameters to align it with the horizontal, and then correct for the cylindrical distortions in section 5.2.3.

Automated cylinder orientation estimation

Using the ellipse fitted to the LED ring reflection in section 5.2.2, the automated orientation estimation, θ, of the cylindrical surface containing the fingerprint is computed. Before applying the distortion correction the image is rotated by θ to align the cylinder with the horizontal, making our method rotation invariant.

To yield the orientation, the parameters of the general ellipse given by (5.4) in section 5.2.2 are used and rearranged.

$$\theta = \tan^{-1}\left(\frac{c - a - \sqrt{(a - c)^2 + b^2}}{b}\right) \tag{5.9}$$

It is important to note when estimating the orientation of an ellipse using (5.9) that when $b = 0$ and $a < c$, then $\theta = 0°$. Similarly, we have $\theta = 90°$ for the case that $b = 0$ and $a > c$. It is for all other cases where the parameter $b \neq 0$ we compute θ using (5.9).

After computing the orientation, θ, this allows us to align the cylinder with the horizontal before applying distortion correction. The fingerprint image is simply rotated by θ, aligning the curved surface with the horizontal as shown in Figure 5.5, where the bounding box also shows the estimation of the surfaces dimensions derived from the ellipse fitting. The circles and half circles which appear in these images are caused by reflections of the LEDs where the RELF algorithm has determined that these pixels are the most likely to contain fingerprint. This is likely due to some superpixels in the training set which have been labelled as containing fingerprint also containing a slight LED reflection.

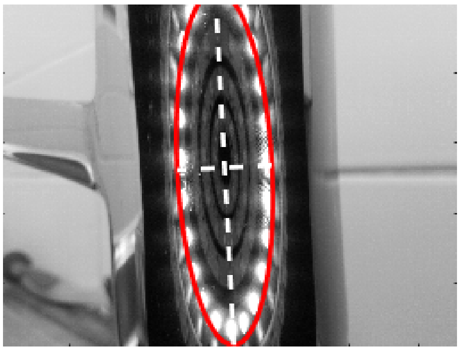

(a) Ellipse fitting.

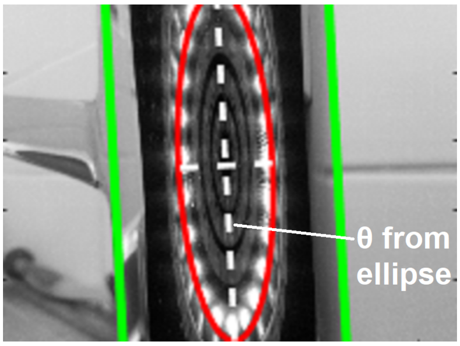

(b) Orientation (θ) and boundary estimation.

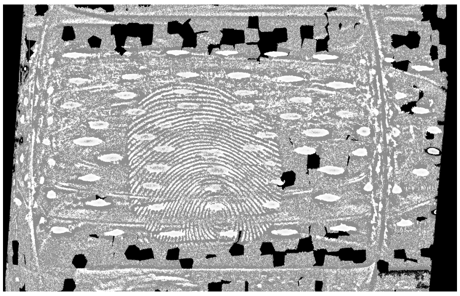

(c) Auto-cropped RELF image rotated by θ.

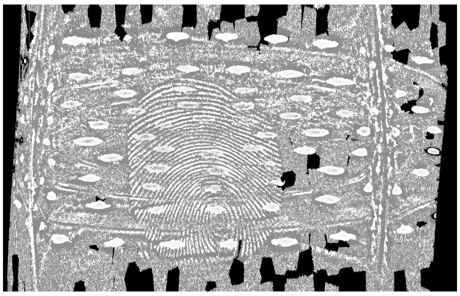

(d) Curvature correction.

(e) Extracted print.

Figure 5.5: Fully automated print extraction and cylindrical curvature correction. (a) shows the ellipse fitting as outlined in section 5.2.2, (b) shows the cylinder orientation and boundary estimation of the surface, (c) shows the extracted latent print which has been automatically rotated and cropped, (d) shows the distortion corrected latent print.

Automated spherical curvature estimation

Our zero contact automated method also estimates the radius of curvature, $R_{curvature}$, for spherical surfaces containing fingerprints.

As described in section 5.2.2 and Figure 5.2,if the LED ring reflection is *elliptical* then the distortion is *cylindrical*, and if the reflection is *circular and smaller* the distortion is *spherical*. For spheres, the *size* of this circular LED ring reflection is used to compute the radius of curvature ($R_{curvature}$) and hence diameter of the spherical surface itself.

Unlike cylindrical surfaces, it is not necessary to estimate the orientation of the sphere since both principal curvatures κ_1 and κ_2 (as defined in section 5.1.3) are equal, therefore rotating a sphere does not affect its curvature.

The location of the sphere's centre is known from the circle fitted to the LED ring reflection as shown in Figure 5.3b.

Using the circle fitted to the reflected LED ring (shown as the inner red circle in Figure 5.3b), it is then possible to determine $R_{curvature}$ and hence the perimeter of the sphere (shown as the green circle in Figure 5.3b).

5.2.3 Automated curvature distortion correction

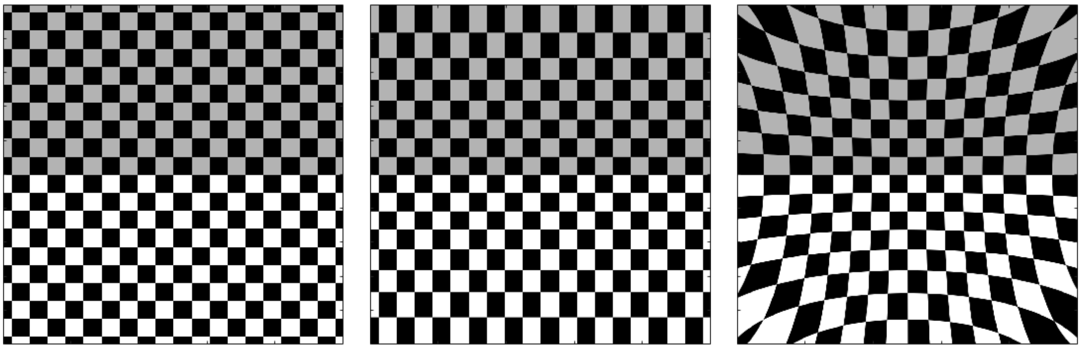

(a) Flat reference surface. (b) Cylindrical distortion correction applied to (a). (c) Spherical distortion correction applied to (a).

Figure 5.6: A representation of the distortion correction applied to a flat reference surface for both cylindrical and spherical distortions. In (a) shows the flat reference surface. In (b) shows the cylindrical distortion correction applied to (a). In (c) shows the spherical (or pincushion) distortion correction applied to (a)

Once the surface's boundaries and curvature are estimated, and we have corrected for lens distortion it is then possible to correct for the geometric distortions caused by this curvature on the fingerprint image. In Figure 5.6 we see a representation of the distortion corrections applied to a flat reference surface for both cylindrical and spherical distortions. In Figure 5.6b we see the cylindrical distortion correction applied to Figure 5.6a and in Figure 5.6c we see the spherical (or pincushion) distortion correction applied to Figure 5.6a.

Automated cylinder distortion correction

For cylindrically curved surfaces, the LED ring reflection's eccentricity computed using (5.8) is used to estimate the radius of curvature ($R_{curvature}$), allowing us to correct any distortions on the fingerprint caused by surface curvature. In Figure 5.7 we see that for the point $P_{distorted}$ the angle β is then obtained using the following:

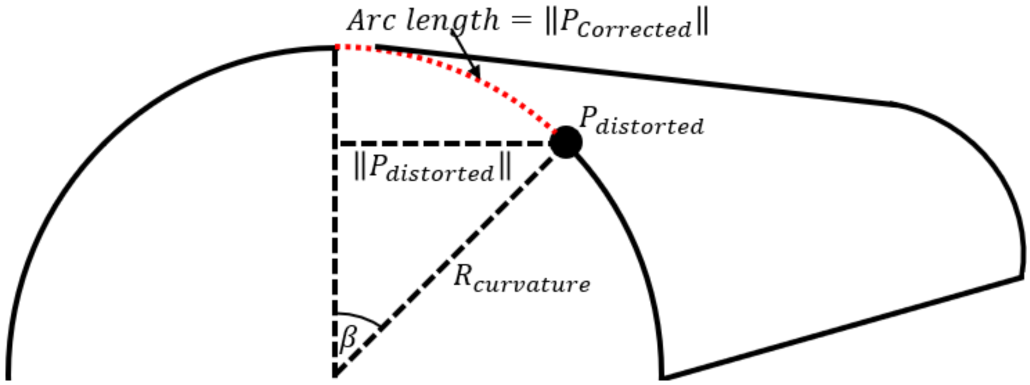

Figure 5.7: The cross section of a cylindrical surface being imaged for latent prints, with the symbols for various parameters defined in section 5.2.3.

$$\beta = \sin^{-1}\left(\frac{\|P_{distorted}\|}{R_{curvature}}\right) \tag{5.10}$$

The length of the arc from the central axis of the cylinder to the point $P_{distorted}$ in Figure 5.7 is then computed using the arc length formula. As shown in Figure 5.7, this arc length is equal to the magnitude of the corrected point $P_{corrected}$, as outlined below.

$$Arclength = \|P_{corrected}\| = R_{curvature}\beta \tag{5.11}$$

Then (5.10) is utilised to substitute for β, yielding the final equation for the transformed point $P_{corrected}$. The point $P_{distorted}$ is transformed from the input image to $P_{corrected}$ as outlined in (5.12) below.

$$\|P_{corrected}\| = R_{curvature}\sin^{-1}\left(\frac{P_{distorted}}{R_{curvature}}\right) \tag{5.12}$$

This transformation defined by (5.12) is visualised in Figure 5.6b. This distortion correction increases fingerprint matching accuracy since matching compares the relative distances between minutiae. The method's increase is shown in match score accuracy in section 5.3.

Automated spherical distortion correction

When a fingerprint is left on a spherical surface, the sphere's curvature has the effect of performing a barrel distortion on the print where the magnification of the image decreases with distance from the optical axis. Barrel distortions are evident in wide-angle lenses used in digital cameras because they are also spherical, and can introduce significant lensing effects in the image [6]. The barrel distortion is then reversed by applying its inverse transformation known as the pincushion distortion, given by (5.13).

$$P_{corrected} = P_{distorted}\left(1 + kP^2_{distorted}\right) \tag{5.13}$$

Here $P_{distorted}$ is the distance to the centre of distortion in the uncorrected image, which is located at the centre of the spherical object as computed in section 5.2.2. $P_{corrected}$ is the distance to the centre of distortion in the corrected image and k is the distortion parameter which is inversely proportional to the radius of the sphere. The pincushion distortion (as shown in Figure 5.6c) is defined so that image magnification is increased as the distance from the optical axis increases [70], meaning lines which don't pass through the centre of the image become curved inwards towards the centre. This spherical distortion correction is shown in Figure 5.8, where the bounding circle also shows the estimation of the sphere dimensions derived from the circle fitting.

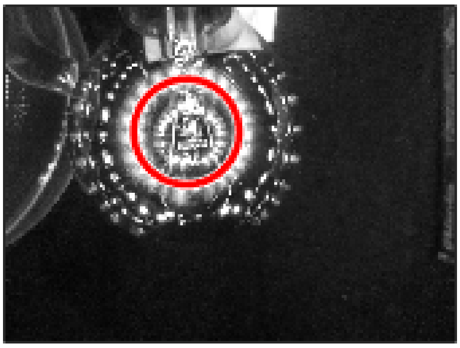

(a) Circle fitting.

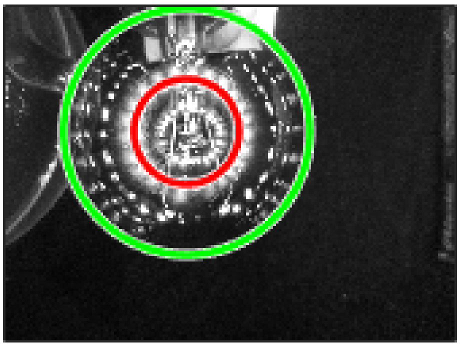

(b) Object boundary estimation.

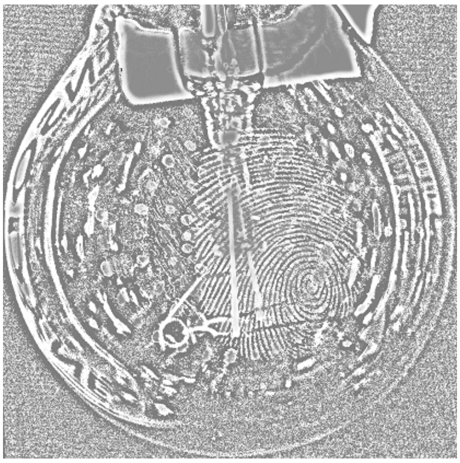

(c) Auto-cropped RELF image.

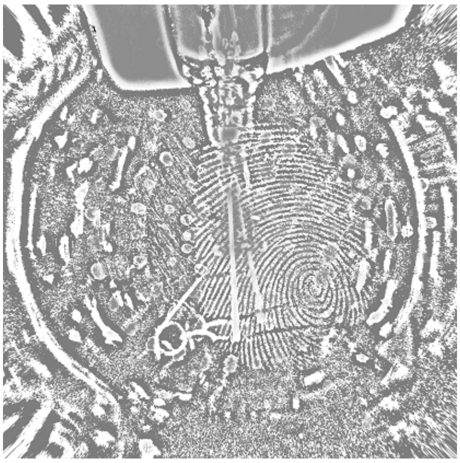

(d) Curvature correction.

(e) Extracted print

Figure 5.8: Fully automated print extraction and spherical curvature correction. (a) shows the circle fitting as outlined in section 5.2.2, (b) shows the boundary estimation of the surface, (c) shows the extracted latent print which has been automatically cropped, (d) shows the distortion corrected latent print.

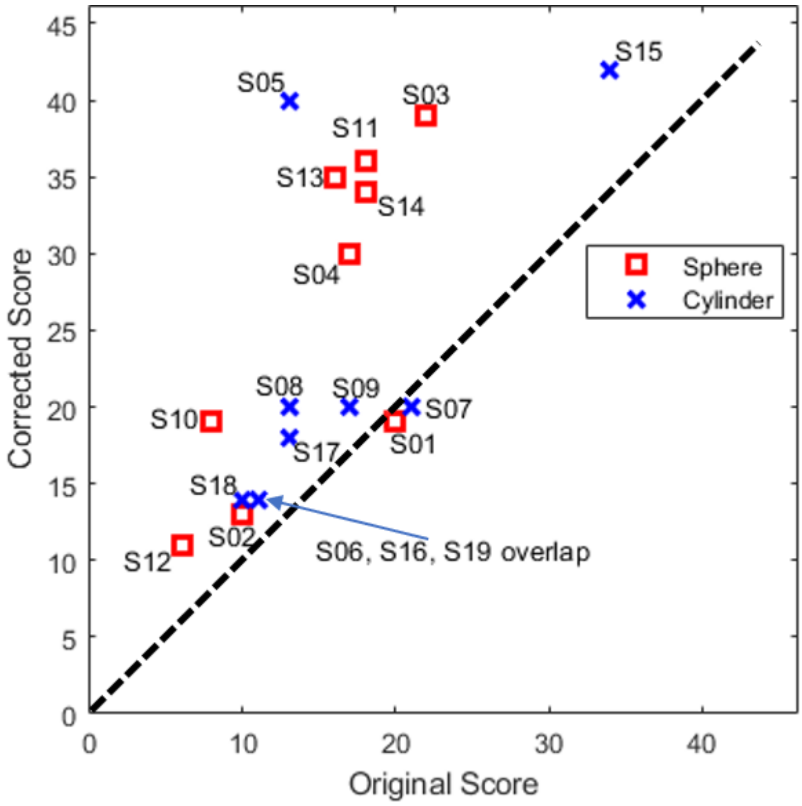

Figure 5.9: Match scores for fingerprints extracted from various spherical and cylindrical surfaces using the proposed method. The horizontal axis shows the score before distortion correction is applied and the vertical axis shows the score after distortion correction is applied. Here the labels refer to arbitrary surface numbers (i.e. surface 1 is referred to as S01)

5.3 Results

In Figure 5.9 the improved match scores for fingerprints extracted from various spherical and cylindrical surfaces using our zero contact automated method are shown, where the labels refer to arbitrary surface numbers (i.e. surface 1 is referred to as S01). The horizontal axis shows the score before distortion correction is applied and the vertical axis shows the score after distortion correction is applied. The diagonal line is plotted to show where the two scores are equal, so the scores plotted above the line have improved after the distortion correction.

In Figure 5.10 latent prints extracted from cylindrical surfaces before and after distortion correction are shown. In Figure 5.10j the latent print with a match score of 34 is shown which has been extracted from surface S15 (cylindrical glass container shown in Figure 5.10l), and which exhibits distortions due to cylindrical curvature. In Figure 5.10k the same latent print is shown from Figure 5.10j after the distortion corrections outlined in section 5.2.3 are applied, resulting in an improved match score of 42. Note that this match score is greater than 40 which generally indicates a true match [46], and is usually only obtainable with patent fingerprints (often made purposefully by inking a finger for example) where the print is clear to see.

In Figure 5.11 latent prints extracted from spherical surfaces before and after distortion correction are shown. In Figure 5.11d the latent print with a match score of 22 is shown which has been extracted from surface S03 (spherical drinking glass shown in Figure 5.11f), which exhibits distortions due to spherical curvature. In Figure 5.11e the same latent print from Figure 5.11d is shown after the distortion corrections outlined in section 5.2.3 are applied, resulting in an improved match score of 39.

These results show the proposed method considerably improves the match score for the vast majority of samples (17 out of 19) and only marginally decreased the score of two samples by 1.

5.4 Conclusions

Continuing our work from chapter 3, we propose a novel method which is able to correct automatically for curvature distortion and improve fingerprint matching scores using the LED pattern from the prototype device described in chapter 4 which also captures the multi-light imaging collection. We show that using our method that it is possible to obtain a match score of greater than 40 (shown in Figure 5.10k) which is significant because this generally indicates a true match [46] and is usually only obtainable with patent fingerprints.

Our rapid method allows for lengthy and contamination-prone traditional forensic analysis of latent prints to be avoided. We estimate the curvature of the surface automatically, extract the latent prints without touching the sample, and finally correct for the distortions caused by the surface curvature. Not only does our method improve the matching score, but it does so in a potentially revolutionary manner since the fingerprint sample remains entirely untouched throughout the process.

The occasional minor reduction in match score by a value of one (for 2 of 19 sample surfaces) is negligible since the reduction is so low in magnitude and we always submit both the distorted (original) and distortion-corrected images for matching. The slight reduction in match score is likely due to the NBIS minutiae extractor MINDTCT being sensitive to image DPI [80], requiring the input image resolution to correspond to an average distance between fingerprint ridges of “around 8 or 9 pixels” [80]. In order to achieve this average fingerprint ridge distance we reduce the resolution of our fingerprint images, which possibly results in loss of information. By varying the image resolution even slightly we see variations in the NBIS match score, possibly due to quantisation error introduced by reducing image resolution. We still opt to use NBIS as it is widely used in research and well recognised in forensics.

We aim to develop a set of experiments which will be carried out to ascertain what factors decrease the NIST match score after the distortion corrections are applied, including investigating the sensitivity of NBIS to image resolution.

(a) S06 with no distortion correction: score of 11.

(b) S06 with distortion correction: score of 14.

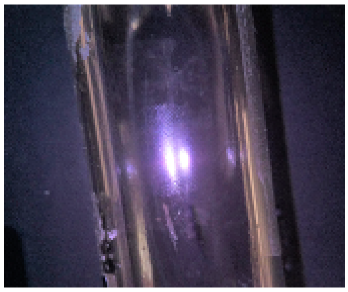

(c) S06: cylindrical glass jar.

(d) S08 with no distortion correction: score of 13.

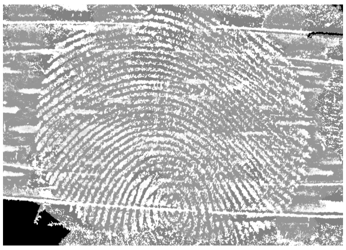

(e) S08 with distortion correction: score of 20.

(f) S08: cylindrical chrome towel rack.

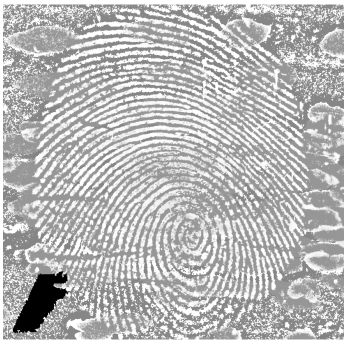

(g) S09 with no distortion correction: score of 17.

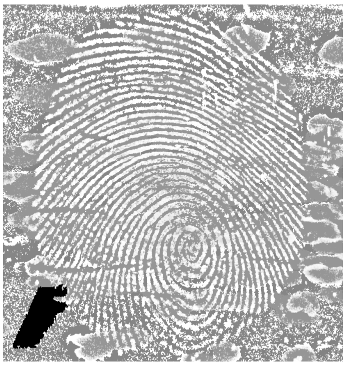

(h) S09 with distortion correction: score of 20.

(i) S09: cylindrical milk bottle.

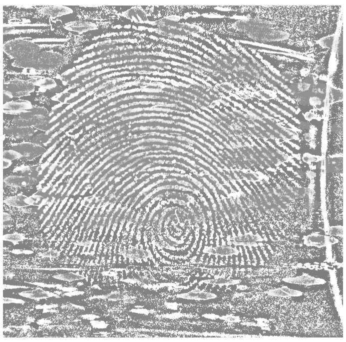

(j) S15 with no distortion correction: score of 34.

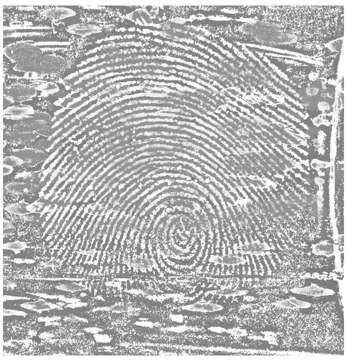

(k) S15 with distortion correction: score of 42.

(l) S15: cylindrical glass container.

Figure 5.10: Latent prints contactlessly extracted from cylindrical surfaces using off-the-shelf and inexpensive hardware described in section 4.1, and processed using the RELF algorithm as detailed in section 5.1.2 with curvature distortions corrected as described in section 5.2.3. Figures (a), (d), (g), (j) show the latent print extracted before distortion corrections and Figures (b), (e),(h),(k) show the prints after distortion correction with improved match scores and Figures (c), (f),(i),(l) show the objects for context.

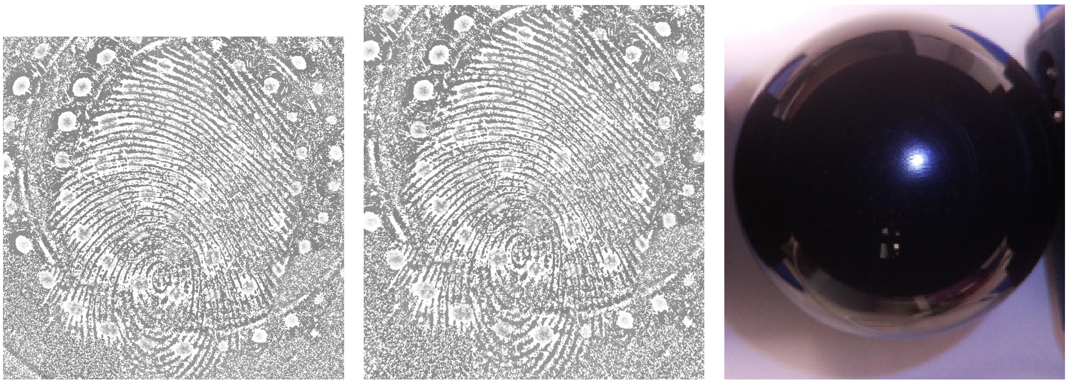

(a) S01 with no distortion correction: score of 20.

(b) S01 with distortion correction: score of 19.

(c) S01: black sphere.

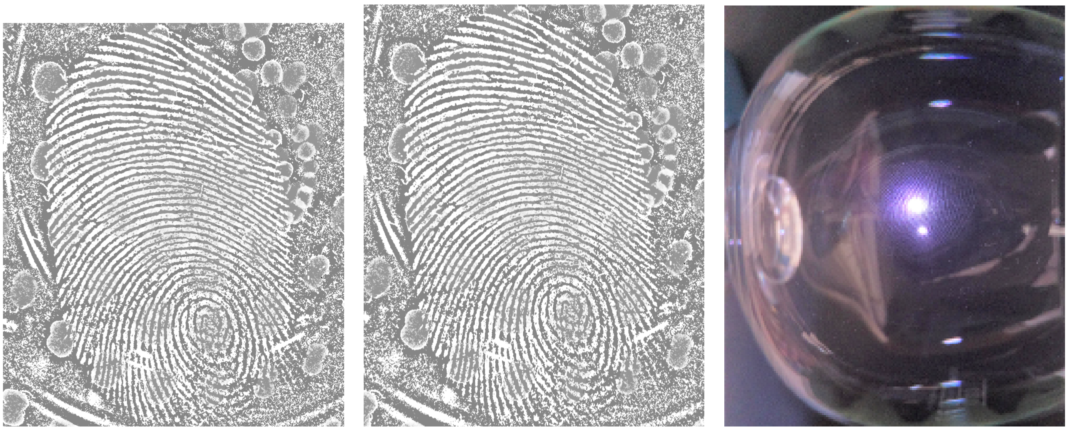

(d) S03 with no distortion correction: score of 22.

(e) S03 with distortion correction: score of 39.

(f) S03: spherical drinking glass.

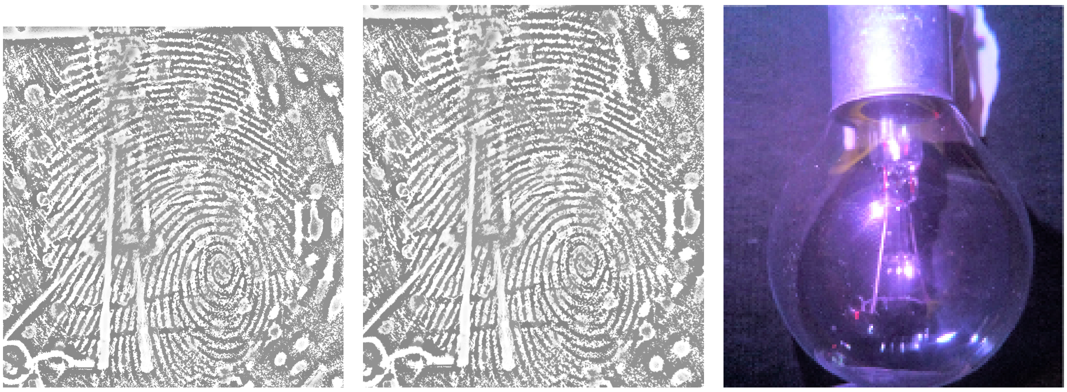

(g) S04 with no distortion correction: score of 17.

(h) S04 with distortion correction: score of 30.

(i) S04: spherical glass bulb.

Figure 5.11: Latent prints contactlessly extracted from spherical surfaces using off-the-shelf and inexpensive hardware described in section 4.1, and processed using the RELF algorithm as detailed in section 5.1.2 with curvature distortions corrected as described in section 5.2.3. Figures (a), (d), (g) show the latent print extracted before distortion corrections and Figures (b), (e), (h) show the prints after distortion correction with improved match scores and Figures (c), (f), (i) show the objects for context. The lightbulb filament visible in S04 adds difficulty to fingerprinting bulbs, but despite this we are still able to extract quality prints and obtain a match.

6 Conclusions

In this thesis, we present our findings and contributions for processing multi-light imaging collections for surface analysis and fingerprint recognition. Multi-light imaging collections are stacks of images captured from a fixed viewpoint under various lighting directions. We review the literature on multi-light imaging, RTI and fingerprint capturing which allowed us to identify gaps in the current knowledge and propose novel methods to address these gaps. Multi-light imaging is contactless and helps to extract information from surfaces at different scales, giving the user valuable tools for visualisation and analysis. In our research we automate and improve the existing multi-light imaging technique known as Reflectance Transformation imaging, as well as developing two novel and automated imaging multi-light imaging techniques firstly for the Remote Extraction of Latent Fingerprints (RELF) and and secondly for the contactless extraction of prints from difficult surfaces with curvature distortion correction.

In chapter 2 we present a novel, fully automated technique for correcting common lighting errors in RTI and markedly improve the accuracy of surface normal estimation, as well as increasing the legibility of low relief surface variations. This moves RTI from the qualitative domain (e.g. enabling the reading of weathered inscriptions) into the quantitative domain of computer vision. Our method also requires no calibration equipment, increasing the simplicity of the standard highlight RTI method by automatically detecting lighting directions and maintain its appeal to non-imaging professionals. The increased quantitative accuracy of surface normals in RTI using our method could potentially make it a more commonly used alternative to laser scanning. While it is not completely immune to very messy multi-light imaging collections, where the light source has largely missed the centre of the object for a significant proportion of the images, our approach is more robust than traditional RTI.

In chapter 3 we propose a novel and robust method for the Remote Extraction of Latent Fingerprints (RELF), without the addition of any contaminants or chemicals to the evidence. We show our technique works on notoriously difficult to image surfaces, using off-the-shelf cameras and a neural network classifier. Our method produces results comparable to more invasive methods and leaves the fingerprint sample unaffected for further forensic analysis (as confirmed through private correspondence with the Covert Policing branch of the Metropolitan Police [60]). Our technique uses machine learning to identify partial fingerprints between successive images and mosaics them. We conduct an extensive feature search to determine which features have the most significant impact on accurate fingerprint classification. We found that all 14 features contribute to the highest NBIS match score when used in RELF, despite a slightly lower F1 score. These findings will aid in optimizing the model in the future.

In chapter 4 we present our RELF prototype developed in collaboration with the UK Metropolitan Police Service following the publication of our results (see [58] and chapter 3). The University of Exeter has filed a priority patent (application number *GB2110863.4*) for this handheld prorotype which is capable of capturing multi-light imaging collections of surfaces containing fingerprints to then be processed using the RELF algorithm. This prototype is fundamental to the method presented in chapter 5, which extends RELF with automated curvature distortion correction.

In chapter 5 we develop our work from chapter 3, with a new method that is able to automatically correct for curvature distortion improving fingerprint matching scores using the reflected LED pattern from the prototype device described in chapter 4 which also captures the multi-light imaging collection. The method is rapid, zero-contact and chemical-free, and is able to obtain high quality fingerprint images from (forensically) difficult curved surfaces. By using our rapid method, the traditional forensic analysis of latent prints that is both lengthy and prone to contamination can be avoided. Our method is able to automatically estimate the surface curvature, extract the latent prints in a contactless manner, and correct for any distortions caused by the surface curvature. This not only improves the matching score, but it also has the potential to significantly speed up the fingerprint collection process, whilst the fingerprint sample remains untouched throughout.

6.1 Future work

Throughout the course of this research, a myriad of intriguing and promising ideas have surfaced, each presenting themselves as a potential avenue for further exploration. As such, the following is a summary of the various research areas that have been identified as having potential for future investigation and study.

6.1.1 Combining RTI and RELF

Despite the potential benefits of RELF and RTI in forensic analysis, there are still some obstacles that need to be addressed before these imaging techniques can be widely used in court. One such hurdle is the need for a reliable method of combining MLICs that have been generated through RELF. The submission of individual images as evidence can be challenging, particularly since each image only reveals a portion of the fingerprint. To overcome this obstacle, we are currently exploring novel methods that combine RTI and RELF techniques, which would enable both methods to be applied to the same MLIC, resulting in a unified and more robust approach to fingerprint analysis. The proposed fusion of these techniques could provide a useful application for processing MLICs since both RTI and RELF use the same image acquisition process, allowing surface normals to be obtained for the fingerprint image. This could potentially yield more information for fingerprint matching, thus potentially enhancing the overall accuracy of the analysis while providing valuable insights for visualisation purposes.

6.1.2 Dynamic move-able RELF system

We are also currently engaged in a project aimed at further enhancing the capabilities of the RELF system. Specifically, we are developing a dynamic system that can be moved around a surface to obtain clear fingerprint images. While our previous collaboration with the Metropolitan Police resulted in a low-cost, completely contactless RELF system that works well for imaging latent fingerprints on difficult surfaces, such as transparent, shiny, and curved ones like light bulbs, the new move-able system we aim to produce will expand the scope of the technique. The existing device is hand-held but must be static, working very well if we know where the prints are. This new system is intended for use in covert/intelligence-gathering operations and aims to significantly increase the number of surfaces from which latent prints can be obtained. It is also intended to reduce the technical and forensic expertise required and speed up the process of identifying individuals of risk.

To achieve this, we are developing a set of experiments aimed making the RELF process as computationally fast as possible and determining what factors in our method may cause a decrease in match score after the distortion corrections described in chapter 5. One aspect of our investigation will be to determine the sensitivity of the National Institute of Standards and Technology Biometric Image Software (NBIS) to image resolution. By understanding the limitations of the current technology, we hope to improve the accuracy and effectiveness of our move-able RELF system, thereby enabling better outcomes for law enforcement agencies and other organisations.

6.1.3 RELF with no superpixels using a Mask R-CNN as classifier

In addition to the developments with the RELF system, we have been working on a new approach for fingerprint classification using mask Region-based Convolutional Neural Networks (R-CNN). The primary motivation for this approach is to eliminate the need for computationally expensive superpixel segmentation in the RELF system. The R-CNN classifier has the potential to provide fast and accurate fingerprint classification, as our preliminary experimental results have shown.

Moreover, we plan to evaluate the R-CNN method by comparing its performance against the current superpixel method used in RELF. This comparison will be done using a wider range of surface types and with the addition of new training and testing surfaces. These tests will provide us with a better understanding of the performance of the R-CNN method in different conditions and its potential for real-world applications.

Our preliminary results indicate that the R-CNN classifier can eliminate the problem of LED reflections that are present in some fingerprint images processed by the superpixel method (which are present in some images as circles and half circles as is visible in Figure 5.5). These LED reflections are present due to some superpixels in the training set which have been labelled as containing fingerprint also containing a slight LED reflection. However, with a mask R-CNN the training masks discard the LED reflections, resulting in the R-CNN classifier not identifying any LED reflections as potential fingerprint, as is the case with the superpixel method.

References

[1] R. Achanta, A. Shaji, K. Smith, A. Lucchi, P. Fua, and S. Süsstrunk. SLIC superpixels. Technical report, École Polytechnique édrale de Lausanne (EPFL), 2010.

[2] R. Achanta, A. Shaji, K. Smith, A. Lucchi, P. Fua, and S. Süsstrunk. SLIC superpixels compared to state-of-the-art superpixel methods. *IEEE transactions on pattern analysis and machine intelligence*, 34(11):2274–2282, 2012.

[3] A. Agrawal, R. Raskar, and R. Chellappa. What is the range of surface reconstructions from a gradient field? In *European Conference on Computer Vision*, pages 578–591. Springer, 2006.

[4] Y. A. Anan'ev. *Laser resonators and the beam divergence problem.* CRC Press, 1992.

[5] M. M. Askarin, K. Wong, and R. C.-W. Phan. Reduced contact lifting of latent fingerprints from curved surfaces. *Journal of Information Security and Applications*, 53:102520, 2020.

[6] D. G. Bailey. A new approach to lens distortion correction. In *Proceedings Image and Vision Computing New Zealand*, volume 2002, pages 59–64, 2002.

[7] J. Baqersad, P. Poozesh, C. Niezrecki, and P. Avitabile. Photogrammetry and optical methods in structural dynamics–a review. *Mechanical Systems and Signal Processing*, 86:17–34, 2017.

[8] F. O. Bartell, E. L. Dereniak, and W. L. Wolfe. The theory and measurement of bidirectional reflectance distribution function (brdf) and bidirectional transmittance distribution function (btdf). In *Radiation scattering in optical systems*, volume 257, pages 154–160. SPIE, 1981.

[9] S. Bleay, V. Sears, R. Downham, H. Bandey, A. Gibson, V. Bowman, L. Fitzgerald, T. Ciuksza, J. Ramadani, and C. Selway. Fingerprint source book v2. 0. *UK Government Home Office*, 665, 2017.

[10] R. Boute, M. Hupkes, N. Kollaard, S. Wouda, K. Seymour, and L. ten Wolde. Revisiting reflectance transformation imaging (RTI): A tool for monitoring and evaluating conservation treatments. *IOP Conference Series: Materials Science and Engineering*, 364:012060, jun 2018.

[11] Y. Castro, G. Pitard, G. Le Goïc, V. Brost, A. Mansouri, A. Pamart, J.-M. Vallet, and L. De Luca. A new method for calibration of the spatial distribution of light positions in free-form rti acquisitions. In *Optics for Arts, Architecture, and Archaeology VII*, volume 11058, pages 127–141. SPIE, 2019.

[12] S. Chang, Y. Cheng, K. V. Larin, Y. Mao, S. Sherif, and C. Flueraru. Optical coherence tomography used for security and fingerprint-sensing applications. *IET Image Processing*, 2(1):48–58, 2008.

[13] N. V. Chawla, K. W. Bowyer, L. O. Hall, and W. P. Kegelmeyer. Smote: synthetic

minority over-sampling technique. *Journal of artificial intelligence research*, 16:321–357, 2002.

[14] H. Coules, P. Orrock, and C. E. Seow. Reflectance transformation imaging as a tool for engineering failure analysis. *Engineering Failure Analysis*, 105:1006–1017, 2019.

[15] Cultural Heritage Imaging. *NIST Biometric Image Software (NBIS), (accessed April 21, 2020)*, 2016.

[16] Cultural Heritage Imaging. *Reflectance Transformation Imaging (RTI), (accessed September 6, 2018)*, 2016.

[17] B.-I. L. Dalenbäck. Room acoustic prediction based on a unified treatment of diffuse and specular reflection. *The journal of the Acoustical Society of America*, 100(2):899–909, 1996.

[18] K. J. Dana, B. Van Ginneken, S. K. Nayar, and J. J. Koenderink. Reflectance and texture of real-world surfaces. *ACM Transactions On Graphics (TOG)*, 18(1):1–34, 1999.

[19] R. J. de Figueiredo and H. D. Tagare. Curves and surfaces in computer vision. In *Curves and Surfaces in Computer Vision and Graphics*, volume 1251, pages 10–16. SPIE, 1990.

[20] S. K. Dubey, T. Anna, C. Shakher, and D. S. Mehta. Fingerprint detection using full-field swept-source optical coherence tomography. *Applied Physics Letters*, 91(18):181106, 2007.

[21] F. Edwin. *Geometrical considerations and nomenclature for reflectance*, volume 160. US Department of Commerce, National Bureau of Standards, 1977.

[22] X. Feng. Comparison of methods for generation of absolute reflectance factor measurements for brdf studies. 1990.

[23] F. D. Foresee and M. T. Hagan. Gauss-newton approximation to Bayesian learning. In *Proceedings of International Conference on Neural Networks (ICNN'97)*, volume 3, pages 1930–1935. IEEE, 1997.

[24] R. Forgeot. *Étude médico-légale des empreintes peu visibles ou invisibles révélées par des procédés spéciaux*. A Storck, 1891.

[25] P. Gautron, J. Krivanek, S. N. Pattanaik, and K. Bouatouch. A novel hemispherical basis for accurate and efficient rendering. *Rendering Techniques*, 2004:321–330, 2004.

[26] A. Ghosh, S. Achutha, W. Heidrich, and M. O'Toole. Brdf acquisition with basis illumination. In *2007 IEEE 11th International Conference on Computer Vision*, pages 1–8. IEEE, 2007.

[27] A. Giachetti, I. M. Ciortan, C. Daffara, G. Marchioro, R. Pintus, and E. Gobbetti. A novel framework for highlight reflectance transformation imaging. *Computer Vision and Image Understanding*, 168:118–131, 2018.

[28] A. Giachetti, C. Daffara, C. Reghelin, E. Gobbetti, and R. Pintus. Light calibration and quality assessment methods for reflectance transformation imaging applied to artworks' analysis. In *Optics for Arts, Architecture, and Archaeology V*, volume 9527, page 95270B. International Society for Optics and Photonics, 2015.

[29] K. Gill, J. Ren, S. Marshall, S. Karthick, and J. Gilchrist. Quality-assured fingerprint image enhancement and extraction using hyperspectral imaging. 2011.

[30] R. C. Gonzalez. *Digital image processing*. Pearson education india, 2009.

[31] G. Haixiang, L. Yijing, J. Shang, G. Mingyun, H. Yuanyue, and G. Bing. Learning from class-imbalanced data: Review of methods and applications. *Expert systems with applications*, 73:220–239, 2017.

[32] Ø. Hammer, S. Bengtson, T. Malzbender, and D. Gelb. Imaging fossils using reflectance transformation and interactive manipulation of virtual light sources. *Palaeontologia Electronica*, 5(1):1–9, 2002.

[33] Y. Han, X.-C. Feng, and G. Baciu. Variational and PCA based natural image segmentation. *Pattern Recognition*, 46(7):1971–1984, 2013.

[34] R. M. Haralick, K. Shanmugam, and I. Dinstein. Textural features for image classification. *IEEE Transactions on Systems, Man, and Cybernetics*, SMC-3(6):610–621, 1973.

[35] H. He and Y. Ma. *Imbalanced learning: foundations, algorithms, and applications*. Wiley-IEEE Press, 2013.

[36] K. He, G. Gkioxari, P. Dollár, and R. Girshick. Mask r-cnn. In *Proceedings of the IEEE international conference on computer vision*, pages 2961–2969, 2017.

[37] Hewlett-Packard. *PTM fitter, (accessed September 6, 2018)*, 2001.

[38] E. H. Holder, L. O. Robinson, and J. H. Laub. *The fingerprint sourcebook*. US Department. of Justice, Office of Justice Programs, National Institute of . . . , 2011.

[39] B. K. Horn. Shape from shading: A method for obtaining the shape of a smooth opaque object from one view. 1970.

[40] B. K. Horn. Height and gradient from shading. *International journal of computer vision*, 5(1):37–75, 1990.

[41] X. Huang, M. Walton, G. Bearman, and O. Cossairt. Near light correction for image relighting and 3D shape recovery. In *Digital Heritage, 2015*, volume 1, pages 215–222. IEEE, 2015.

[42] X. Jiang and W.-Y. Yau. Fingerprint minutiae matching based on the local and global structures. In *Proceedings 15th international conference on pattern recognition. ICPR-2000*, volume 2, pages 1038–1041. IEEE, 2000.

[43] M. R. Jimenez, C. Müller, and H. Pottmann. Discretizations of surfaces with constant ratio of principal curvatures. *Discrete & Computational Geometry*, 63(3):670–704, 2020.

[44] L. Jost. Entropy and diversity. *Oikos*, 113(2):363–375, 2006.

[45] S. Kiltz, M. Hildebrandt, J. Dittmann, and C. Vielhauer. Challenges in contact-less latent fingerprint processing in crime scenes: Review of sensors and image processing investigations. In *2012 Proceedings of the 20th European Signal Processing Conference (EUSIPCO)*, pages 1504–1508. IEEE, 2012.

[46] K. Ko et al. Users guide to export controlled distribution of nist biometric image software (nbis-ec). 2007.

[47] V. Krátkỳ, P. Petráček, V. Spurnỳ, and M. Saska. Autonomous reflectance transformation imaging by a team of unmanned aerial vehicles. *IEEE Robotics and Automation Letters*, 5(2):2302–2309, 2020.

[48] K. Kuivalainen, K.-E. Peiponen, and K. Myller. Application of a diffractive element-based sensor for detection of latent fingerprints from a curved smooth surface. *Measurement Science and Technology*, 20(7):077002, 2009.

[49] M. Kurt and D. Edwards. A survey of brdf models for computer graphics. *ACM SIGGRAPH Computer Graphics*, 43(2):1–7, 2009.

[50] J.-H. Lambert. *JH Lambert,... Photometria, sive de Mensura et gradibus luminis, colorum et umbrae.* sumptibus viduae E. Klett, 1760.

[51] H. C. Lee and R. Gaensslen. Methods of latent fingerprint development. *Advances in fingerprint technology*, 2(105-176):10, 2001.

[52] C. Lennard. Fingermark detection and identification: current research efforts. *Australian Journal of Forensic Sciences*, 52(2):125–145, 2020.

[53] S. Lin and H.-Y. Shum. Separation of diffuse and specular reflection in color images. In *Proceedings of the 2001 IEEE Computer Society Conference on Computer Vision and Pattern Recognition. CVPR 2001*, volume 1, pages I–I. IEEE, 2001.

[54] S.-S. Lin, K. M. Yemelyanov, E. N. Pugh Jr, and N. Engheta. Polarization-based and specular-reflection-based noncontact latent fingerprint imaging and lifting. *JOSA A*, 23(9):2137–2153, 2006.

[55] D. J. MacKay. Bayesian interpolation. *Neural computation*, 4(3):415–447, 1992.

[56] T. Malzbender, D. Gelb, and H. Wolters. Polynomial texture maps. In *Proceedings of the 28th annual conference on Computer graphics and interactive techniques*, pages 519–528, 2001.

[57] J. Martin, P. ten Hagen, W. Strasser, R. Guedj, D. Duce, C. Osland, G. Enderle, W. Hewitt, R. Hubbold, A. Arnold, et al. Computer graphics software workshop report. In *Comput. Graph. Forum*, volume 1, pages 10–13, 1982.

[58] M. McGuigan and J. Christmas. Remote extraction of latent fingerprints (RELF). In *2020 International Joint Conference on Neural Networks (IJCNN)*. IEEE, jul 2020.

[59] E. R. Menzel. *Fingerprint detection with lasers.* M. Dekker New York, 1999.

[60] Metropolitan Police Covert Policing. Private correspondence, 2021.

[61] J. Min, S. Jeong, K. Park, Y. Choi, D. Lee, J. Ahn, D. Har, and S. Ahn. Reflectance transformation imaging for documenting changes through treatment of joseon dynasty coins. *Heritage Science*, 9(1):1–12, 2021.

[62] J. Mnookin, P. J. Kellman, I. Dror, G. Erlikhman, P. Garrigan, T. Ghose, E. Metler, and D. Charlton. Error rates for latent fingerprinting as a function of visual complexity and cognitive difficulty. *Report. NIJ Award*, 2009.

[63] J. L. Mnookin. Fingerprint evidence in an age of dna profiling. *Brook. L. Rev.*, 67:13, 2001.

[64] J. J. Moré. The levenberg-marquardt algorithm: implementation and theory. In *Numerical analysis*, pages 105–116. Springer, 1978.

[65] M. Mudge, T. Malzbender, C. Schroer, and M. Lum. New reflection transformation imaging methods for rock art and multiple-viewpoint display. In *The 7th International Symposium on Virtual Reality, Archaeology and Cultural Heritage (VAST)*, volume 6, pages 195–202, 2006.

[66] M. U. Munir and M. Y. Javed. Fingerprint matching using ridge patterns. In *2005 International Conference on Information and Communication Technologies*, pages 116–120. IEEE, 2005.

[67] H. Mytum and J. Peterson. The application of reflectance transformation imaging (rti) in historical archaeology. *Historical Archaeology*, 52(2):489–503, 2018.

[68] S. E. Newman. Applications of reflectance transformation imaging (rti) to the study of bone surface modifications. *Journal of Archaeological Science*, 53:536–549, 2015.

[69] L. O'Gorman. An overview of fingerprint verification technologies. *Information Security Technical Report*, 3(1):21–32, 1998.

[70] H. Ojanen. Automatic correction of lens distortion by using digital image processing. *Rutgers University, Dept. of Mathematics technical report*, 1999.

[71] B. T. Phong. Illumination for computer generated pictures. *Communications of the ACM*, 18(6):311–317, 1975.

[72] D. A. Pisner and D. M. Schnyer. Support vector machine. In *Machine learning*, pages 101–121. Elsevier, 2020.

[73] G. Pitard, G. Le Goïc, H. Favrelière, S. Samper, S.-F. Desage, and M. Pillet. Discrete modal decomposition for surface appearance modelling and rendering. In *Optical Measurement Systems for Industrial Inspection IX*, volume 9525, pages 952523:1–10. International Society for Optics and Photonics, 2015.

[74] Y. Quéau, R. Mecca, J.-D. Durou, and X. Descombes. Photometric stereo with only two images: A theoretical study and numerical resolution. *Image and Vision Computing*, 57:175–191, 2017.

[75] C. Ricci, K. A. Chan, and S. G. Kazarian. Combining the tape-lift method and fourier transform infrared spectroscopic imaging for forensic applications. *Applied Spectroscopy*, 60(9):1013–1021, 2006.

[76] S. R. Richter and S. Roth. Discriminative shape from shading in uncalibrated illumination. In *Proceedings of the IEEE Conference on Computer Vision and Pattern Recognition*, pages 1128–1136, 2015.

[77] J. K. Ross and A. Marshak. Calculation of canopy bidirectional reflectance using the monte carlo method. *Remote Sensing of Environment*, 24(2):213–225, 1988.

[78] S. R. Safavian and D. Landgrebe. A survey of decision tree classifier methodology. *IEEE transactions on systems, man, and cybernetics*, 21(3):660–674, 1991.

[79] W. R. Scott. *Fingerprint mechanics, a handbook: fingerprints from crime scene to courtroom*. Thomas, 1951.

[80] L. Scuderi, T. Nagle-McNaughton, and J. Williams. Trace evidence from mars' past: Fingerprinting transverse aeolian ridges. *Remote Sensing*, 11(9), 2019.

[81] B. G. Sherlock, D. Monro, and K. Millard. Fingerprint enhancement by directional

fourier filtering. *IEE Proceedings-Vision, Image and Signal Processing*, 141(2):87–94, 1994.

[82] G. S. Sodhi and J. Kaur. Powder method for detecting latent fingerprints: a review. *Forensic science international*, 120(3):172–176, 2001.

[83] Y. Sun, A. K. Wong, and M. S. Kamel. Classification of imbalanced data: A review. *International journal of pattern recognition and artificial intelligence*, 23(04):687–719, 2009.

[84] M. B. Thompson, J. M. Tangen, and D. J. McCarthy. Expertise in fingerprint identification. *Journal of forensic sciences*, 58(6):1519–1530, 2013.

[85] T. Tuytelaars, K. Mikolajczyk, et al. Local invariant feature detectors: a survey. *Foundations and trends® in computer graphics and vision*, 3(3):177–280, 2008.

[86] C. F. Van Loan and G. Golub. Matrix computations (johns hopkins studies in mathematical sciences). *Matrix Computations*, 1996.

[87] T. Vogl, J. Mangis, and A. Rigler. Kl, zink, wt and alkon, dl, 1988, accelerating the convergence of the back-propagation method. *Biological Cybernetics*, 59:263.

[88] O. Wang, P. Gunawardane, S. Scher, and J. Davis. Material classification using brdf slices. In *2009 IEEE Conference on Computer Vision and Pattern Recognition*, pages 2805–2811. IEEE, 2009.

[89] Z. Wang, S. Chen, C. Busch, and X. Niu. Performance evaluation of fingerprint enhancement algorithms. In *2008 Congress on Image and Signal Processing*, volume 3, pages 389–393. IEEE, 2008.

[90] V. L. Williams and R. T. Lockie. Optical contamination assessment by bidirectional reflectance-distribution function (brdf) measurement. *Optical Engineering*, 18(2):152–156, 1979.

[91] H. Winick and S. Doniach. *Synchrotron radiation research*. Springer Science & Business Media, 2012.

[92] H. Winnemöller, A. Mohan, J. Tumblin, and B. Gooch. Light waving: Estimating light positions from photographs alone. *Computer Graphics Forum*, 24(3):433–438, 2005.

[93] R. J. Woodham. Photometric method for determining surface orientation from multiple images. *Optical engineering*, 19(1):139–144, 1980.

[94] L. Yan and J. Chen. Non-intrusive fingerprints extraction from hyperspectral imagery. In *2018 26th European Signal Processing Conference (EUSIPCO)*, pages 1432–1436. IEEE, 2018.

[95] A. Yilmaz, O. Javed, and M. Shah. Object tracking: A survey. *Acm computing surveys (CSUR)*, 38(4):13–es, 2006.

[96] M. Zhang and M. S. Drew. Efficient robust image interpolation and surface properties using polynomial texture mapping. *EURASIP Journal on Image and Video Processing*, 2014(1):1–19, 2014.

[97] Q. Zheng, A. Kumar, and G. Pan. Contactless 3d fingerprint identification without 3d reconstruction. In *2018 International Workshop on Biometrics and Forensics (IWBF)*, pages 1–6. IEEE, 2018.